Effect of Ischemic Stroke on Neuronal and Glial Cell Structure in the Peri-Infarct Zone of Adult Mice

by Armin Bayati

A Thesis Submitted in Partial Fulfillment of the Requirements for the Degree of
BACHELOR'S OF SCIENCE
in the Honour's Biology and Psychology Combined Program

Supervisory Committee:

Dr. Patrick C. Nahirney, Co-supervisor,
Division of Medical Sciences

Dr. Brian R. Christie, Co-supervisor,
Division of Medical Sciences

Dr. Raad Nashmi, Honour's Advisor
Department of Biology

Dr. Craig Brown, External Examiner,
Division of Medical Sciences

Abstract

Cerebral ischemia, more commonly referred to as a stroke, results in widespread cognitive and behavioural dysfunction. Between the necrotic core and the unaffected intact brain, lies a small but distinct region known as the peri-infarct (PI) zone. This zone has been theorized to undergo dramatic remodelling and remapping in post-stroke recovery. To investigate how this zone changes at the cellular level, light and transmission electron microscopy were used to examine the PI and to compare its morphology to that of the unaffected contralateral brain tissue in a mouse model of cerebral ischemia. Five adult mice were subject to photothrombotic stroke (~3-5 mm^3 in size) in the forelimb region of the somatosensory cortex (SSC) of the parietal lobe and at 72 hours post-ischemia, mice were perfusion fixed with aldehydes and then sectioned with a vibratome, micro-dissected, post-fixed, dehydrated and embedded in Spurr's resin. Toluidine blue-stained sections were imaged with light microscopy for qualitative analysis. At 72 hours, the PI, measuring between 100-200 μm in width, appeared less dense and frothy but contained perfused capillaries. Electron micrographs (EMs) were obtained from layers 2-5 of the contralateral and PI SSC (6.58 x 4.39 μm test field) and analyzed for synaptic and vesicular density, areas occupied by presynaptic and postsynaptic terminals, postsynaptic densities, mitochondria and astrocytes. The qualitative analyses yielded noticeable differences between control, PI, and infarct tissue. Average synaptic density per test field was significantly reduced in the PI compared to the contralateral SSC (7.200 ± 1.304 vs 18.520 ± 1.119, $p<0.0001$), whereas no significant difference was found in vesicular density per synapse ($p=0.186$). Similarly, no changes were observed in total presynaptic area ($p=0.628$) or postsynaptic area ($p=0.541$). Postsynaptic density areas within terminals were reduced in the PI (0.090 ± 0.047 μm^2 vs 0.246 ± 0.130 μm^2, $p=0.014$) while total mitochondrial area showed a large increase (5.967 ± 5.064 μm^2 vs 1.557 ± 0.163 μm^2, $p<0.05$). This increase in area was largely due to swelling of the mitochondria. The most striking change in the parenchyma of the PI was a dramatic increase in astrocyte area (6.503 ± 0.966 μm^2 vs 2.809 ± 0.544 μm^2, $p=0.0004$). Astrocytes exhibited a spacious cytoplasm with scattered organelles and a dramatic increase in glycogen granules. These findings shed light on the underlying ultrastructural changes within the PI that represent the initial cellular responses at 72 hours and potential reconfiguration of neural connections. The progression of these morphological changes might ultimately account for the regression in stroke-induced symptoms following cerebral infarction.

Table of Contents

List of Figures

List of Tables

List of Abbreviations

AMPA: α-amino-3-hydroxy-5-methyl-4-isoxazolepropionic acid
BBB: Blood brain barrier
DNA: Deoxyribonucleic acid
EM: Electron micrograph
GABA: Gamma-Aminobutyric acid
mAChR: Muscarinic acetylcholine receptor
NMDA: *N*-methyl-D-aspartate receptor
PI: Peri-infarct
PID: Peri-infarct depolarization
PLC: Phospholipase C
RNA: Ribonucleic acidS1: Primary somatosensory cortex
S2: Secondary somatosensory cortex
SSC: Somatosensory cortex
V-ATPase: Vacuolar-type H^+-ATPase
VGLUT: Vesicular glutamate transporter

Dedication

I would like to thank Dr. Nahirney for opening up the world of electron microscopy for me and allowing me to learn the skills required to take staggeringly beautiful images of neurons. I will forever thank you for the opportunity and for your kindness in giving me a chance to be a part of your lab. Prior to meeting you, I thought my attention to detail far surpassed most individuals; however, I believe you redefine the meaning of the word ‘detail’. Thank you for the second chance.

I would also like to take this opportunity to thank Dr. Christie for his kindness throughout my work in the Christie and Nahirney lab. I would also like to thank Dr. Christie’s graduate student, Scott Sawchuk, for aiding me in getting started and gaining experience in the field of confocal imaging and spine analysis. The immunohistochemistry and stacked imaging experience provided me with a different view on the world of dendrites and dendritic branching.

To Taryn, thank you for being there, and thank you for being with me. You know as I know that I couldn’t have done this without you. I love you.

Thanks to Mom and Dad for your support in all my endeavours, even if sometimes they are contradictory to what you think is best. I hope that the contents of this thesis unveil to you my interests in neuroscience and the field of microscopy, in ways I could never describe myself.

Thanks to Irene for being the best sister in the world. You are my favourite sister!

Finally, I would like to thank Dr. Bruce Wright, head of the division of medical sciences for his unending support of my work and his help whenever things got out of hand (which was more times than I was comfortable with).

Introduction

Cerebral infarcts (otherwise referred to as cerebral stroke or ischemia) are among the most common underlying causes of cognitive dysfunction, and motor and sensory impairment in humans. By far, they are among the most difficult of cerebrovascular and neurological diseases to recover from, and their onset is perhaps the most unpredictable (Kalaria et al., 2016). Additionally, individuals who have previously endured cerebral ischemia are at a higher risk of having future cerebral strokes (Johnston et al., 2009). This property makes cerebral ischemia even more debilitating. Despite the medical knowledge regarding the symptoms and emergency procedures required at the time of the accident, the underlying causes of cognitive impairment following stroke are unknown. Although the basis of these cognitive impairments can be related to the hypoxic conditions that neuronal tissues are subjected to during ischemia (Nathaniel et al., 2015), the precise process and mechanism by which neuronal functioning and communication changes to give rise to the ensuing cognitive impairments are unknown. Simply put, other than cellular necrosis, very little is known about the cellular and molecular consequences of stroke.

At their most basic level, cerebrovascular accidents are a result of blockages in blood vessels that feed into brain tissues. The blockage of blood flow within capillaries throughout the brain causes an interruption in nutrient transport for the ensuing brain tissue as well as a disruption in the export of waste materials from these tissues into the circulatory system (Binienda et al., 1996). Similarly, bleeding within the brain would cause the absence of blood flow in other vital areas of the brain in addition to adverse consequences resulting from the buildup of intracranial pressure within the skull (Beard et al., 2016). In severe cases of ischemia, long periods of interruption in blood flow take place; therefore, the associated neurons affected by the blockage enter an anoxic state, where their oxygen stores are entirely depleted. Anoxic conditions often cause disintegration of neurons and neuronal scaffolding structures (carried out by glial cells), ultimately resulting in cerebral infarction (Yanagihara, 1974). Thus, many downstream effects may be responsible for cognitive and behavioural deficits in patients.

Recent research has found that cerebral ischemia exhibits neurodegenerative characteristics within subjects. Specifically, affected necrotic tissue has been known to invade healthier (perfused or intact) and more distal (to the focal core of stroke) tissues (Strong et al., 2007). This phenomena, referred to as PI depolarization (PID), for periods following cerebral infarction, at which time blood supply has been re-established within these regions (Hartings et al., 2003). As a result of PID and other potentially unknown mechanisms, neurons that are often

relatively far away from the necrotic core gain characteristics similar to the affected tissue. The specific mechanisms behind this invasion of perfused tissues are unknown (Zhang et al., 2012). Moreover, the existence of this phenomena is somewhat alarming since our current understanding of ischemia is one of acute onset. Evidently, this conventional understanding is lacking and incomplete.

This thesis attempts to explore the morphological (structural characteristics) changes that occur in the brain following the onset of cerebral infarcts. Using the mouse model, the effects of stroke on brain tissue were observed using advanced imaging techniques on tissues obtained 72 hours following the onset of stroke. Both light and transmission electron microscopy were used in an attempt to observe and quantify changes in morphology and structures of neurons and their synaptic connections.

1.1 Neuronal structures and substructures

With the advent of microscopy and advancements in optics, the microscopic world has become accessible to the researcher's macroscopic environment. In the field of biology, microscopy has allowed for different cell types to be identified in different organisms and this knowledge has allowed for an evolutionary organization of animals based on the observed cellular structures, morphology and characteristics (Masland, 2004). Within the body, there exists a plethora of different cell types. Despite the existence of a complete copy of the genetic code in almost all cells, each equipped with the same transcriptional and translational machinery, the underlying mechanisms that give rise to different cell types has been a debated topic. Through advancements in the field of genetics, it is now believed that epigenetics (e.g. chromatin remodelling and histone acetylation/deacetylation) is the primary contributor of this phenomenon (Carmichael et al., 2017; Nelson et al., 2006).

Due to the rise of different cell types within organisms, compartmentalization of function and processes were achieved that eventually gave rise to the nervous system. Segmentation, cephalization, the formation of ganglia, neuropils, neuronal circuits, allowed organisms to adopt different senses and motor capabilities throughout evolution (Shigeno et al., 2001, 2007; Swanson, 2013). The entailing sections outline the different levels of organizations within the nervous system and detail many fundamental discoveries. It should be noted that although an organized approach is taken in describing the various discoveries pertaining to the nervous system, much of these areas of inquiry were conducted simultaneously by various scientists in

different fields (i.e. psychologists, biologists, medical practitioners, zoologists). The convergence of these multiple avenues of discovery have only recently merged to create the field of neuroscience (Abbott, 2008).

1.2 Neuronal subtypes

Many different neurons exist within the central nervous system. While the spinal cord primarily consists of interneurons and segmented nuclei and the communication of afferent and efferent tracts, the brain consists of much more complex neuronal organization (Peljto and Wichterle, 2011). Arguably, the complexity of nervous system must, therefore, rely heavily on the existence of different cell types, and respectively unique capabilities (Adrian, 1948). Within the brain, complexity arises from three factors: layering, lateralization, and localization (Crochet and Petersen, 2009; Willshaw, 2006). Early research within the field of neuroscience postulated the existence of laterality, meaning that the right and left hemispheres of the brain perform different functions. Following laterality, multiple levels of localization were then explored by neuroscientists. Initially misguided attempts at localization were carried out by phrenologists, in which particular behaviours were attributed, in an arbitrary manner, to different parts of the brain (Simpson, 2005). Scientific research soon ensued that disqualified the findings of these individuals which, unfortunately, also resulted in a push against functional localization within the brain (Brett et al., 2002). However, further research into neurological, behavioural, and structural disorders as a result of brain trauma, provided neuroscientists with unique opportunities to glimpse at the correlation between structure and function (Kerr et al., 2005). Eventually, lateralization was followed by localization of function, with each different cerebral lobe serving fundamental functions in cognitive and behavioural processing. Correlative observations in abnormal subjects with symptomatic behaviours were one of such opportunities to explore the functions of neural tissue. Broca was the first to adopt such methodology, with his findings based mostly on the symptoms and the injury of his patient Tan (Selnes and Hillis, 2000).

Behavioural studies led to curiosity regarding the biological components of the nervous system and factors underlying human consciousness. Tissue staining and the advances in light microscopy allowed for such understanding to occur in the brain and other organs. Research carried out by Golgi and Cajal is the most well-known example of such endeavours (De Carlos and Borrell, 2007).

Tissue staining aided the discovery of different cellular layers within the neocortex, along with layering of cells in subcortical regions of the brain, known as the archicortex (Braak, 1974). Principal among these staining methods was the Golgi stain. Otherwise known as the black reaction, Golgi staining became popular mainly due to its ability to penetrate neuronal tissue, and to only dye a selective number of neurons within that tissue, allowing for easy observation of single neuronal structures. This was the main advantage of Golgi staining, as other stains penetrated too many neuronal structures, producing an image with many overlaying cellular structures, rendering the tissue useless for structural analysis. Another advantage posed by Golgi staining was its ability to stain neuronal processes such axons, and dendrites, providing scientists with visuals of neuronal processes that were never seen before. Thus, Golgi staining allowed for the discovery of the layered neuronal organization within the neocortex.

More advanced staining techniques have since been developed, some even incorporating the original Golgi stain with other chemicals (Rosoklija et al., 2014). Recently developed stains exploit unique chemical and physical characteristics of the structures of interest, which may be located intra or extracellularly. For instance, toluidine blue is one of such stains, developed long after the Golgi, with a high affinity for acidic structures, and therefore, serving as a useful stain for biological tissues with abundant deoxyribonucleic acid (DNA) and ribonucleic acid (RNA) molecules. Due to this affinity, toluidine blue (see Figures 1 and 2) staining is frequently used for highlighting specific regions of *in vivo* and *in vitro* biological samples.

As microscopy aided scientists in visualizing neurons and glial cells, it also allowed further understanding and visualization of neuronal processes and connections, such as synapses, dendrites and axons. Dendrites are known mainly for their ability to receive information from other, often neighbouring neurons (Nimchinsky et al., 2002). They are considered as the receivers of information and convey the received information as excitatory and inhibitory postsynaptic potentials within the neuron. Dendrites can integrate information from thousands of neighbouring neurons due to the presence of dendritic spines (Rochefort and Konnerth, 2012). Spines allow transient synaptic connections, accompanied by chemical isolation and synaptic specification (e.g. specific neurotransmitter action at specific concentrations).

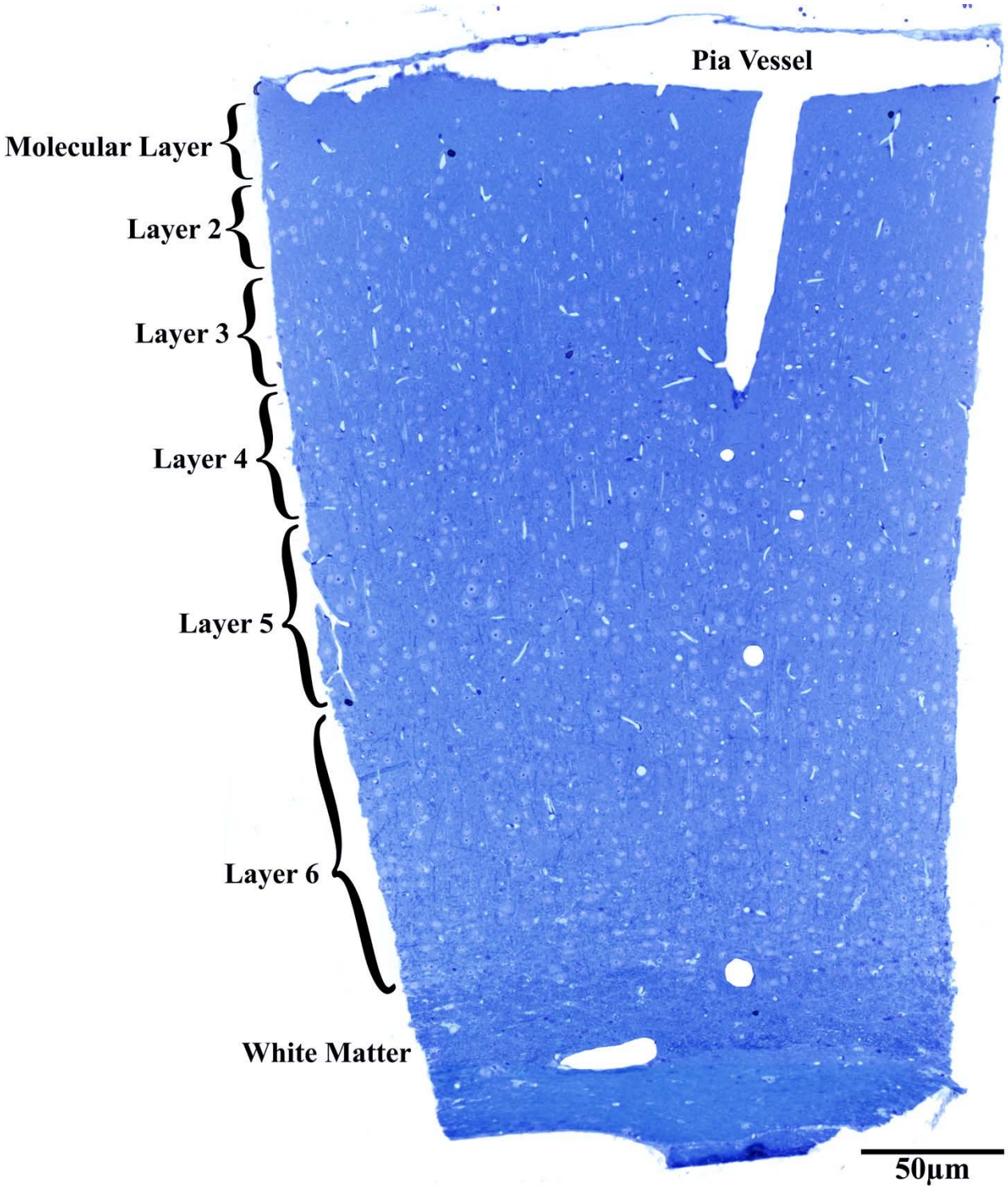

Figure 1. Toluidine blue stain light micrograph of layers 1-6 of an adult mouse SSC.
Cortical layers show distinct cellular morphology, with a variety of dendritic and axonal processes surrounding them. The molecular layer contains most of the axonal and dendritic processes, while layers 2-6 are largely composed of neuronal soma. Layers 1-3 are involved in interhemispheric communication and efferents that travel to the spinal cord. Layers 4 and 5 contain a large number of stellate and pyramidal neurons with layer 5 having the largest pyramidal neurons of all the layers. Along with layer 6 that mostly contains small pyramidal neurons, these layers send and receive information to subcortical structures such as the thalamus. White matter region is composed of a large number of axonal fibers supplied by layers 2-6, with its characteristic fibrous and dense apperance largely due to the high concentration of myelinated fibers. Semithin (0.5 µm) section.

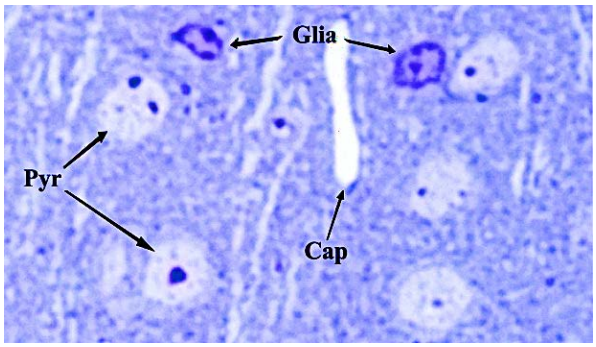

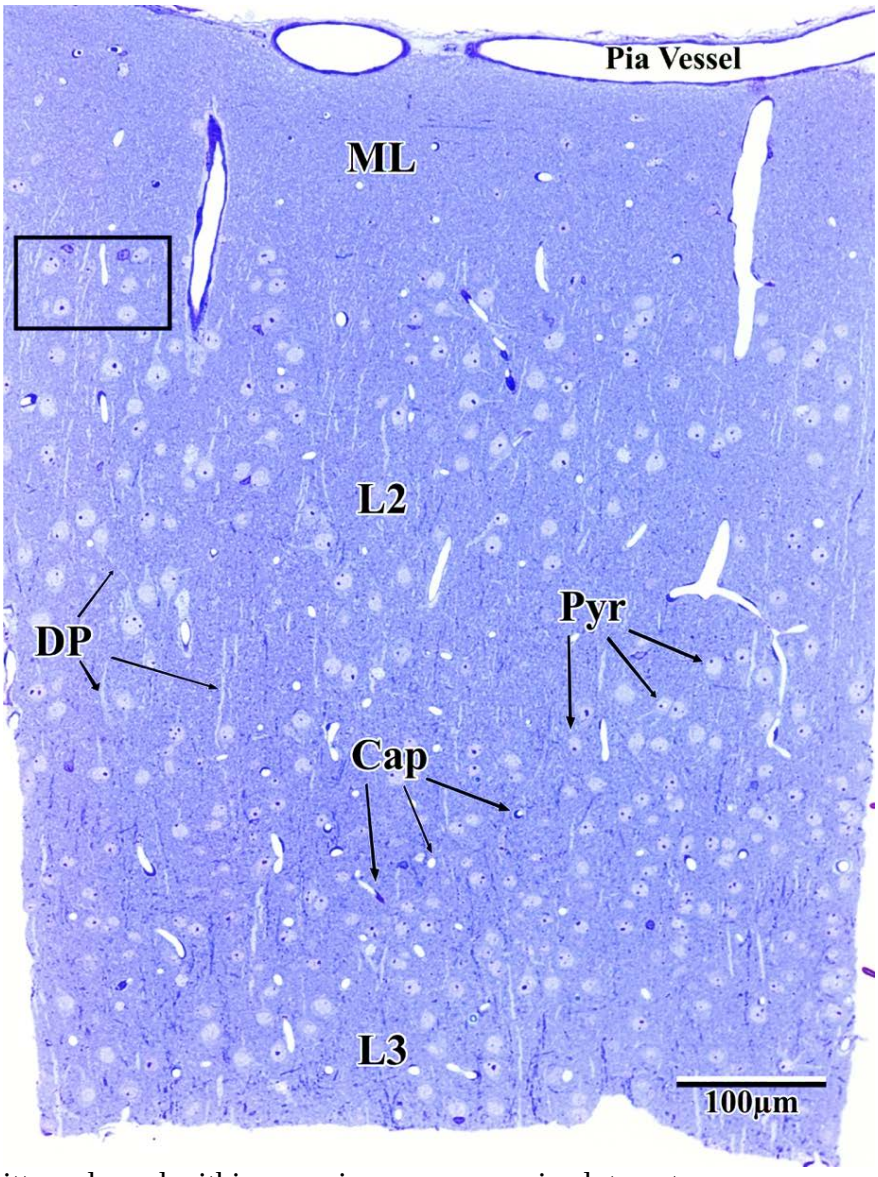

Figure 2. Light micrograph of a toluidine blue-stained section of adult mouse SSC showing layers 1-3. (Right) Pia mater, a component of the meninges, contains pial vessels that contribute to cortical perfusion. Situated below the pia, the molecular layer (ML) contains few if any neurons since it is mainly a site of dendritic and axonal connections, whereas, layers 2 (L2) and 3 (L3) contain high concentrations of pyramidal (Pyr) neurons with long dendritic processes (DP). Stellate neurons, astrocytes, and microglia are also common structures within L2 and L3, although they are harder to identify at lower magnifications due to their relatively small size. Saturated with a variety of cells, L2 and L3 contain a larger number of penetrating blood vessels and capillaries (Cap). Pyramidal neurons within L3 are larger than those found in L2 and are targets of corticocortical afferent and efferent connections. (Above) a closeup of the above image shows glial and neuronal structures.

The most common neurotransmitter released within axospinous synapses is glutamate (Chih et al., 2005). Excitatory glutamate receptors, α-amino-3-hydroxy-5-methyl-4-isoxazolepropionic acid (AMPA) and *N*-Methyl-D-aspartic acid (NMDA) receptors, are most likely to occupy the postsynaptic membrane of spines. Dendritic spines, by virtue of their protruding structures, also possess a profound ability to increase the surface area of the dendrite, allowing for more synaptic connections to be made with other cells (see Figure 3). However, the most critical feature of these structures lies within their ability to facilitate plasticity: making new connections based on neuronal circuit firing and learning (Malenka and Bear, 2004). The transient nature of these connections provides neurons with an infinite capacity to form new synaptic connections, and in this way, spines may be the underlying mechanism of neuroplasticity.

Regardless of the type of synaptic connection that is made with the postsynaptic neuron, the summation of postsynaptic potentials is eventually integrated into the latter portion of the soma, called the axon hillock. The integration of electrical potential within this region may result in the propagation of action potentials along the axon (Stuart et al., 1997). Neurophysiologists have closely studied the electrical properties of neurons during and following neurotransmission through methods such as patch-clamp recording. These studies contributed to our understanding of the way in which neuronal communication takes place and its chemical underpinnings (Ogden and Stanfield, 1981). Structural, electrical, and later biochemical, properties of cells allowed for their categorization based on such properties. Thus, within any specific category of neuronal or glial cells, subtypes of cells may exist that exhibit different electrical and chemical properties. Such complexity within the nervous system can, therefore, be considered as the fundamental basis as to why such complex cognitive and behavioural tasks are undertaken by the cerebral cortex (Koch and Laurent, 1999).

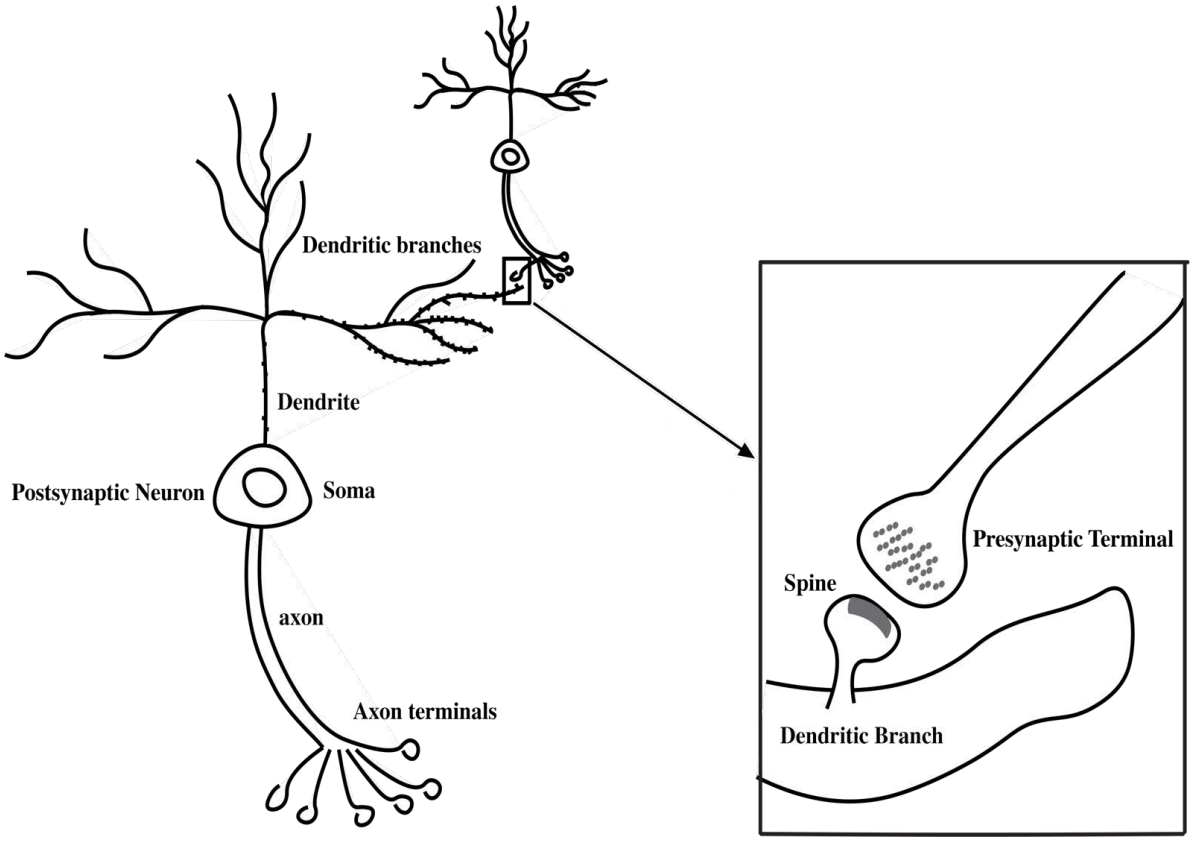

Figure 3: Pyramidal neurons forming synaptic connections.
Stereotypical spine morphology and synaptic connection between presynaptic and postsynaptic structures are illustrated above. To mimic the structural characterstics of pyramidal neurons, the soma was morphed into a triangular shape. Drawings are not to scale.

For this thesis, specific attention was paid to neurons located within the cerebral cortical layers 2-5. As a result of this, almost all of the neurons analyzed were cortical pyramidal cells (see Figure 1 and 2), named for their characteristic pyramidal-shaped cell body (Masland, 2004).

1.3 Glial cells: astrocytes

Currently, biological classification recognizes the existence of two distinct types of cells within the central nervous system: neuronal cells and glial cells. The former has been associated with electrical and conductive properties, responsible for the generating and processing sensory inputs and motor outputs (Freeman et al., 2003). Much less is known about the functions of glial cells which include such cell types as astrocytes, microglia, ependymal cells, radial glia, and oligodendrocytes. The functional roles of these cells have been classically considered as secondary, hence not as crucial as neurons, mainly due to their inability to propagate action potentials (Banerjee and Bhat, 2007). However, research on the function of glial cells and their differentiated progeny, has yielded many findings regarding the critical nature of these cells in supporting normal neuronal functioning (Hansson and Rönnbäck, 2003).

Research reports on neurodegenerative disorders have provided additional proof regarding the necessity of glial cells and their functions within the central nervous system. Scientists have found that many causes of neuronal apoptosis are in fact a direct result of abnormal metabolic processes and aberrant structural properties of glial cells (Miller et al., 2004). Supporting evidence has also been found for the involvement of glial cells in controlling neurotransmission, neuronal scaffolding, adhesive properties, insulation of neurons, and their control on capillaries (Auld and Robitaille, 2003; Banerjee and Bhat, 2008; Frotscher et al., 2003; Jackson and Haydon, 2008; Metea, 2006).

Research on astrocytes (see Figures 4 and 5) within recent years, has garnered much attention by neuroscientists (Abbott et al., 2006; Ballabh et al., 2004). Astrocytes serve as a critical component in neuronal homeostasis and have been implicated in controlling functions such as attenuation of blood pressure within major and penetrating blood vessels within cortical and subcortical regions. Thus, it is not surprising that astrocytes also serve a role in maintaining the integrity of the blood brain barrier (BBB) (Abbott et al., 2006). Since the blood vessels are often fully encapsulated by astrocytic endfeet, astrocytes serve as the second line of defence in denying the entrance of foreign materials into the brain, second to endothelial cells and their tight

junctions. To this end, they have also been shown to serve as storage systems for compounds that do make it across the BBB (Heni et al., 2011).

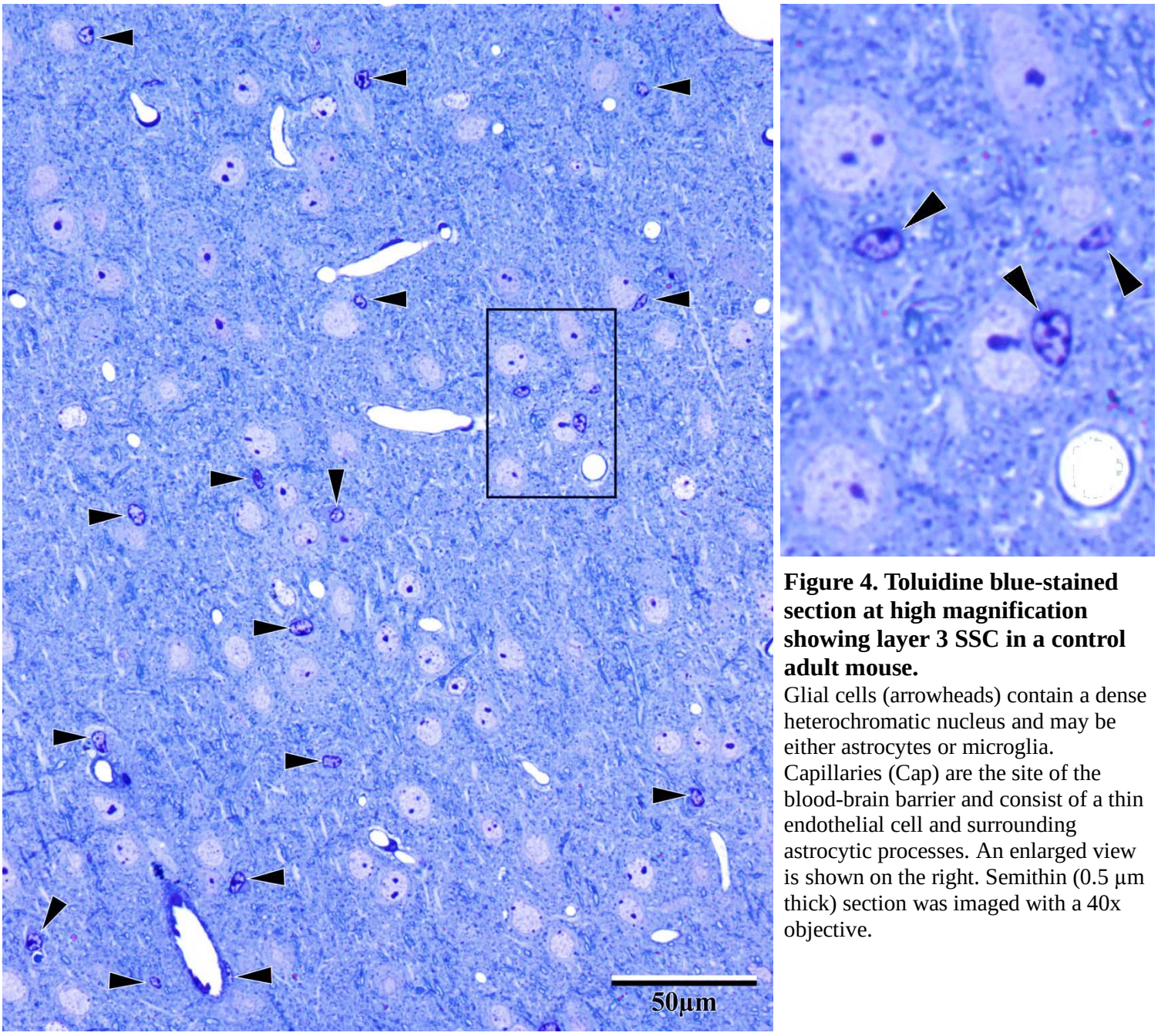

Figure 4. Toluidine blue-stained section at high magnification showing layer 3 SSC in a control adult mouse.
Glial cells (arrowheads) contain a dense heterochromatic nucleus and may be either astrocytes or microglia. Capillaries (Cap) are the site of the blood-brain barrier and consist of a thin endothelial cell and surrounding astrocytic processes. An enlarged view is shown on the right. Semithin (0.5 µm thick) section was imaged with a 40x objective.

Along with microglia, astrocytes are also known to make frequent connections with synaptic structures, specifically at the synaptic cleft (Paolicelli et al., 2011). Initially, astrocytes were believed to be involved as potential neuromodulators, adjusting the responsivity of postsynaptic neurons to presynaptic signalling. Although this remains to be the case, additional functionality of astrocytes such as reinforcing presynaptic and postsynaptic connections, and

serving enzymatic roles in synaptic neurotransmission such as reuptake, recycling and degradation of neurotransmitters and neuropeptides (Chung et al., 2015). In short, it is clear that astrocytes play a crucial role in neuronal functioning, and it is, therefore, not surprising that they have also been implicated in ischemia and post-ischemic neuronal remapping (Zhao and Rempe, 2010).

1.4 Neuronal substructures

The advent of high-resolution electron microscopy provided scientists with the ability to explore the subcellular structures common to all cells throughout the body (Kaneko et al., 2005). This is due to the inherent properties of electrons, which compared to photons, possess higher energy levels and therefore smaller wavelengths, allowing for higher resolving power to be attained by electron microscopes (Williams and Carter, 2009). With a few exceptions, every cell in the body possesses a plasma membrane, a nucleus (or multiple nuclei in some cells), mitochondria, endoplasmic reticulum, ribosomes, cytoskeletal structures (e.g. microtubules, intermediate filaments and microfilaments), lysosomes, Golgi bodies, vacuoles, vesicles and an amorphous cytosol (see Figure 5 and Appendix A). Such structures are very difficult to visualize using light microscopy despite the advances in tissue staining and immunohistochemistry. Resolving power for light microscopy is approximatively 0.30 μm while electron microscopes possess a resolving power of up to 0.0001 μm (Inoue and Oldenbourg, 1994). Electron microscopy, therefore, allowed for a higher level of understanding of cells and their corresponding functions (Scholtyseck and Mehlhorn, 1970). The discovery of these subcellular components and their relative concentration within different cells resulted in further categorization of cells within the central nervous system.

Organelles work in conjunction with one another to form a functioning cell/neuron (Mullins, 2005). Mitochondria, for example, are responsible for fulfilling the energy needs of cells by incorporating many critical biochemical processes such as the Krebs cycle within their specialized lumen, driving the electron transport chain which is responsible for the phosphorylation of adenosine mono- and di-phosphate to adenosine triphosphates. These organelles are present in high concentrations within neurons, especially within the presynaptic terminal due to the large amounts of energy that is required for synthesis and modification of neurotransmitters, chemical signalling, vesicle exocytosis, and the endocytosis of vesicles to retain the terminal integrity (Gray, 1963).

The energy synthesized by the mitochondria is temporarily stored within adenosine triphosphate bonds that are then utilized by other cellular structures for the synthesis of biomolecules essential for cellular functioning and communication. As mentioned, some of this energy is used in preparation, propa5 gation, and post-propagative processes relating to neurotransmission. However, the main source of energy consumption within neurons (and within most cells) is protein synthesis. The process of transcription and translation consumes a significant amount of energy (Tantama et al., 2013). Ribozyme and enzymes that partake in these cellular pathways degrade large amounts adenosine triphosphates due to the high level of accuracy employed in these processes (Rodnina et al., 1994). The process of transcription is initiated within the nucleus, and the resulting messenger ribonucleic acid (mRNA) is then transported into the endoplasmic reticulum or the cytosol for RNA editing and/or RNA splicing and will ultimately be translated into proteins via the use of ribosomes. Proteins synthesized by ribosomes on the rough endoplasmic reticulum are either packaged by the Golgi bodies and translocated to the plasma membrane for exocytosis, or remain within the cell where they contribute to the internal structure and function of the cell (Jewett et al., 2013).

The processes involved in the translation of proteins within the cell are analogous to those involved in neurotransmitter synthesis (Brodin et al., 1999; Younts et al., 2016). The synthesis of these molecules is primarily known to occur within the soma and carried to the presynaptic membrane using dynein and kinesin cargo proteins. Although neuropeptides are almost exclusively produced and packaged within the soma, small molecule neurotransmitters are often incorporated into vesicles by the soma in inactive/non-functional format, or they are merely synthesized at the presynaptic terminal. In some cases, for molecules partially synthesized at the soma, the transported vesicles also contain the necessary enzymes required to turn neurotransmitters into their active form (Lam et al., 1974). Regardless of the site of synthesis, small molecule neurotransmitters such as glycine, glutamate, gamma-Aminobutyric acid (GABA), and acetylcholine, all need to be loaded into neurotransmitting vesicles at the presynaptic terminal. Such processes require vesicular proteins such as vacuolar-type H^+-ATPase (V-ATPase) which is responsible for creating a proton gradient with high concentrations of H^+ within the interior of the vesicle (Patel et al., 2007). This gradient is then used to drive the loading of neurotransmitters into vesicles through an antiporter integral protein (e.g. vesicular glutamate transporter, otherwise referred to as VGLUT). The contents of these vesicles are then released into the synaptic cleft through exocytosis by the presynaptic terminal, and the

neurotransmitters are therefore free to act on receptors located on the postsynaptic terminal. Depending on the type of receptors present on the postsynaptic membrane, any number of responses can take place in the postsynaptic neuron. Upon neurotransmitter binding, ionotropic receptors simply increase ion conductance to cations or anions. On the other hand, metabotropic receptors activate intracellular secondary messengers, causing a downstream cascade of reactions within the postsynaptic neuron. For instance, M_1 muscarinic acetylcholine receptors (mAChR), are coupled with G_q (one of many G proteins), and once they are activated, they, in turn, activate G_q, which starts an intracellular cascade of reactions that begins with the activation of phospholipase C (PLC) (Nathanson, 2006).

Cytoskeletal structures (see Figures 6), such as microfilaments, microtubules, and intermediate filaments, are utilized within neurons for the transportation of vesicles to and from the presynaptic membrane, in addition to maintaining the shape and the integrity of the neuron and neuronal structures. Dyneins and kinesins are often responsible for such processes, with the latter carrying vesicles to the presynaptic terminal, while the former carries them away from the presynaptic membrane (Zhu et al., 2005). These proteins crawl along microtubules, that are connected to the cell membrane, and are responsible for supporting and retaining the shape of the neuron and neuronal structures (Fletcher and Mullins, 2010). Intermediate filaments (see Figure 6) are also responsible for structural integrity, primarily due to their more stable structures.

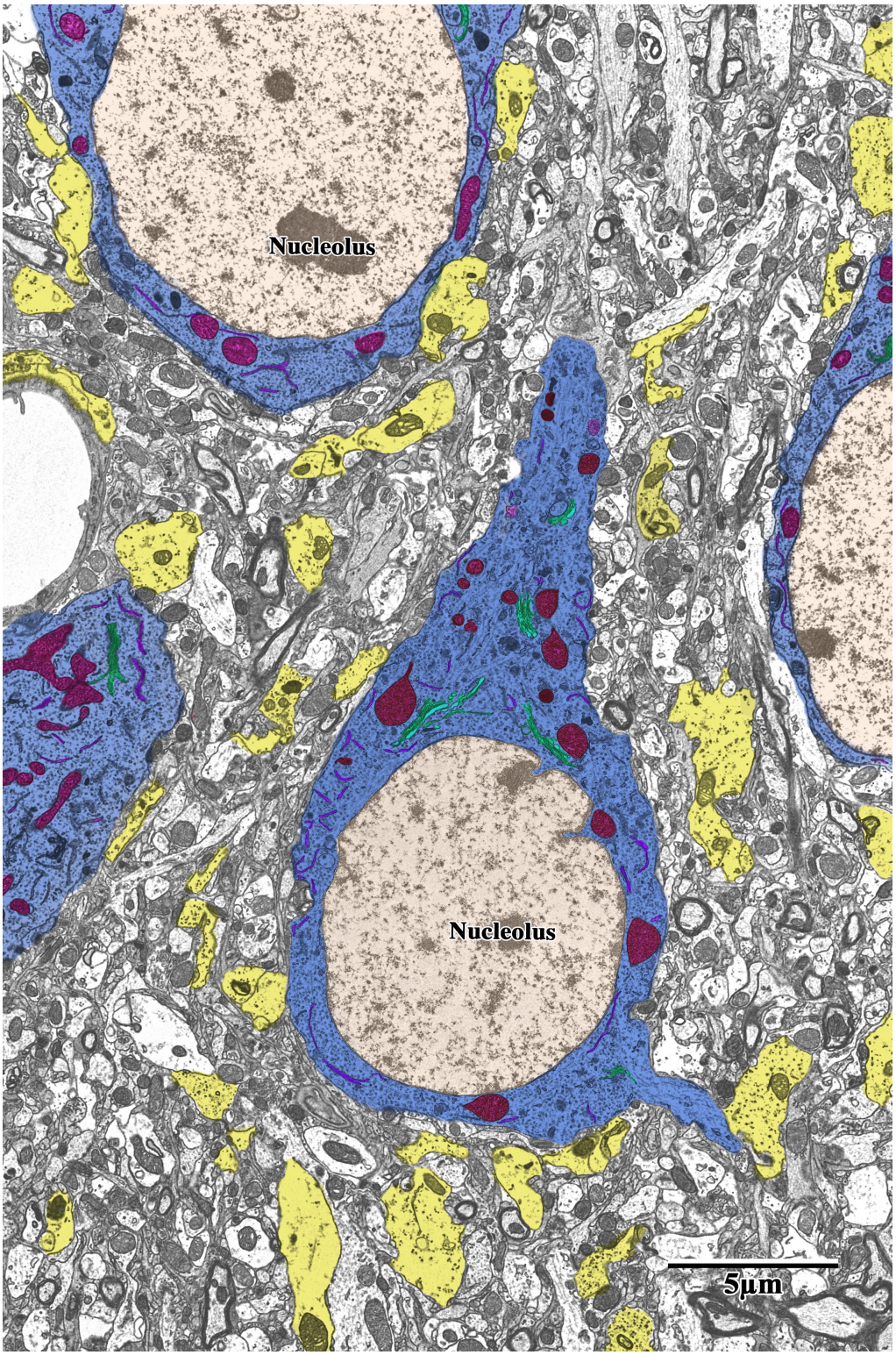

Figure 5: Pseudocoloured pyramidal neurons and astrocytic processes located within layer 5 of adult mouse SSC.
Cellular organelles were traced and coloured for identification. Outlined subcellular structures include: cytoplasm (blue), mitochondria (red), nucleus (orange), Golgi (green), endoplasmic reticulum (purple), and multivesicular bodies (pink). Visible astrocytic processes were also identified and psuedocoloured (yellow).

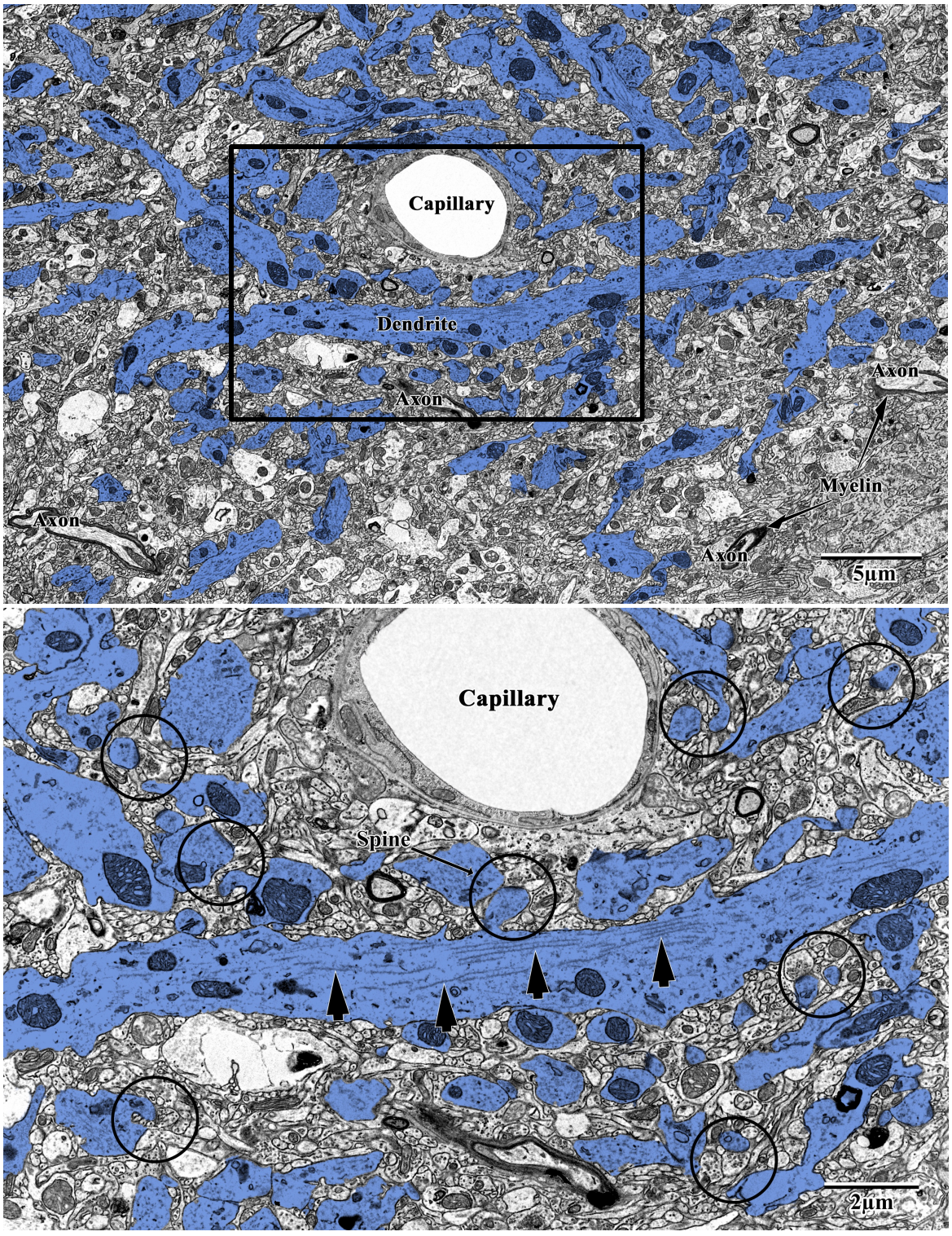

Figure 6. EM of dendritic processes and synaptic structures surrounding capillaries in layer 3 adult mouse SSC

Dendritic processes were identified based on cytoskeletal and organelle morphology and pseudocoloured in blue. (Above) conveys the widespread occupation of neuronal dendritic processes and synaptic structures and their proximity to capillaries. (Below) indicates cytoskeletal microtubules (short arrow) running along the length of a dendrite, along with synaptic connections(circles).

1.5 Synaptic Structures

The presynaptic terminal is the ending point of the axonal process (Murthy and De Camilli, 2003). This terminal is often filled with neurotransmitter vesicles, many of which may be located within the active zone. The receiving structure, the postsynaptic terminal (e.g. spine head), belongs to the receiving neuron (Sheng and Kim, 2002, 2011). The postsynaptic membrane often contains many ligand-gated ion channels, that, in response to neurotransmitter binding, will open their channels to specific ions. Excitatory synapses (see Figure 7), known as type I synapses, will result in the flow of cations into the postsynaptic terminal, while inhibitory neurotransmitters known as type II synapses, selectively allow the flow of anions (Morales et al., 2011). Interestingly, based on previous imaging studies, it has been shown that synapses with postsynaptic densities are excitatory synapses, while ones without the presence of postsynaptic density densities are inhibitory synapses.

Additional information regarding the nature of the synapse can be derived from vesicular morphology (Boyken et al., 2013; Castorph et al., 2010; Imig et al., 2014). Round, transparent, and small diameter (~50nm) sized vesicles are associated with excitatory synapses, while flattened, oval vesicles (~90nm) are associated with inhibitory synapses. Due to the electrophysiological properties of these synapses, inhibitory synapses are almost always found close to the cell body, while excitatory synapses are found in more distal sights on the dendrite. More information has been obtained in recent years regarding the type of neurotransmitter and ion channels that exist within different synapses. Excitatory synapses within the nervous system are mostly glutamatergic, while inhibitory neurotransmission is carried out by GABA and glycine (Murthy and De Camilli, 2003). The postsynaptic density, seen exclusively in excitatory or mixed synapses, was initially discovered in EMs, signified by darker electron dense regions on the inner aspect of the postsynaptic membrane (Boeckers, 2006). Postsynaptic density has since been postulated to represent a large cluster of proteins associated with the postsynaptic membrane that are responsible for the recruiting, maintaining, and supporting receptors on the postsynaptic membrane (Beique et al., 2006; Kim et al., 2007). Commonly associated postsynaptic density proteins include glutamate receptors (i.e. NMDA, AMPA, and kainate receptors), PSD95 protein which is involved in the anchoring of proteins to the postsynaptic receptors, and neuroligin which has adhesive properties and is a vital component of normal synaptic communication (Chubykin et al., 2007).

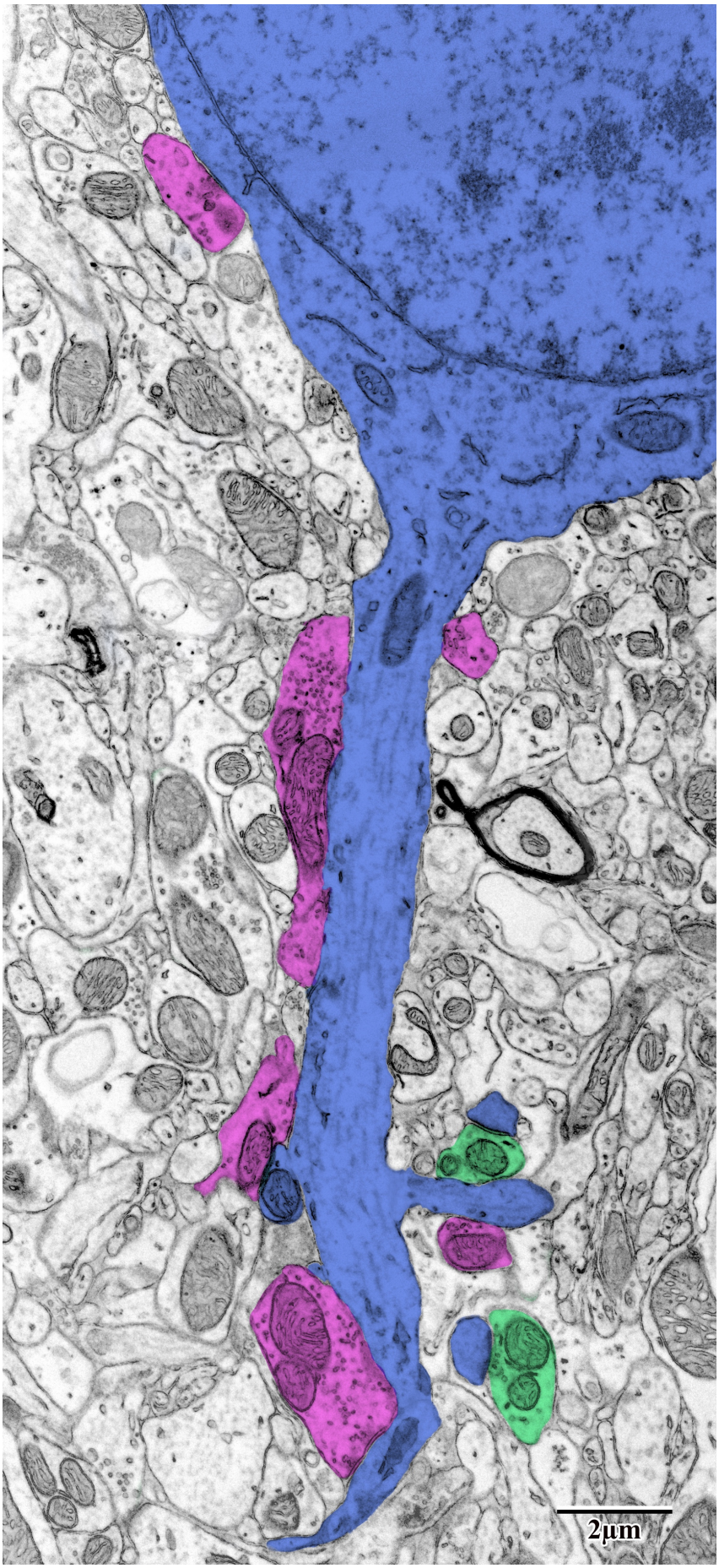

Figure 7: Inhibitory and excitatory synapses in layer 2 of adult mouse SSC. Pyramidal cell (blue) and associated postsynaptic structures were shown in association with presynaptic (green or purple) terminals. Presynaptic terminals forming inhibitory synapses (purple) typically are found on the cell soma and dendrite, whereas excitatory synapses (green) are located on dendritic spines.

In addition to the nature of the synapse (i.e. excitatory or inhibitory), there exist other differentiating qualities. Some of the most common synapses within the cerebral cortex include mixed synapses, perforated synapses, axosomatic synapses, compound synapses, and the traditional axodendritic synapses (Choquet and Triller, 2013; Nieto-Sampedro et al., 1982). Mixed synapses, which are difficult to identify in EMs, contain a mix of chemical and electrical methods of communication, involving both neurotransmission and conveying of electrical information through gap junctions. On the other hand, compound synapses are structurally situated so that the dendrite (or cell) is receiving information from multiple axons (or vice versa). Meanwhile, perforated synapses, another variant of the classical synapse, contains more than one active zone and postsynaptic density while the communication is limited to only one presynaptic and one postsynaptic terminal.

In sum, it is with the discovery of the variety of different neuronal structures and substructures, that a much more in-depth understanding of neuronal functioning has been achieved. The functions of such subcellular structures have been attained through a variety of experimental paradigms, some of which include the comparison of normal functioning cells to mutated, transgenic or diseased animal models (Donohue and Ascoli, 2011; Schmitz et al., 2011; Uylings and de Brabander, 2002). Animal models of ischemia have been utilized by a variety of researchers in neuroscience to study the underlying principles of cognitive and behavioural abnormalities seen in patients following cerebral infarction.

1.6 Stroke

Stroke is a general term referring to the restriction in blood supply that often has clinical consequences due to the body's continuous demand for oxygenated blood (Iadecola and Alexander, 2001). Many causes exist for the occurrence of stroke, chief among which include problems within the blood vessels themselves, such as vessel elasticity, which is usually a result of congenital diseases (Berweck et al., 2008; Rodan et al., 2012). However, the leading causes of stroke have often been attributed to atherosclerosis, embolism, and thrombosis, all of which are not directly influenced by congenital factors.

Atherosclerosis is a disease associated with the buildup of biological compounds and ions within blood vessels, resulting in the narrowing of blood vessels that eventually develop into restrictions in blood flow (Lusis, 2000). Multiple outcomes can occur in individuals afflicted with such a disease. Two of the most studied outcomes are chronic hypoxia within the organs

that are connected to the restricted blood vessel, and the occurrence of anoxia, a result of complete blockage of blood vessel, leading to the obstruction of blood flow in the ensuing organ (Hultén and Levin, 2009). A complete blockage is often not caused by the building of arteriolar plaques alone and often requires the addition of other dislodged materials within the circulatory system to contribute to previous plaque buildups. The dislodged material act in conjunction with arteriolar plaques in leading to the detrimental outcome of acute ischemia. On the other hand, the dislodging of large materials throughout the circulatory system, in the absence of plaques, are alone sufficient in causing a stroke. This phenomena, referred to as an embolism, is the lodging or aggregation of fat globules, blood clots (thrombosis), gasses, or foreign materials within the bloodstream, giving rise to occluded blood vessels. (Goldhaber and Bounameaux, 2012).

1.7 Types of cerebral infarction

Cerebral infarcts are often categorized into two groups: ischemic and hemorrhagic. Cerebral ischemia is defined as a condition in which blood supply to the brain or specific parts of the brain are impeded resulting in inadequate oxygen supply for the ensuing neural tissues, metabolic dysfunction, and eventually cell death (Broughton et al., 2009). An interruption of more than a few minutes often results in irreversible damage to brain tissue, with permanent loss of function due to significant neuronal death.

Hemorrhagic stroke is a result of intracranial bleeding (within the brain) that often results in the lack of blood flow to vital brain tissue due to the cranial bleed (Fisher, 1971). More lethal, however, is the rise in the intracranial pressure caused by the intracranial bleed, which can incur physical pressures onto sensitive brain areas, resulting in neuronal death. Hemorrhagic strokes are much less common than ischemic strokes, but their outcomes are often more lethal due to the increased risk of cranial collapse due to increased pressure. Individuals rarely survive this types of stroke, with almost half of the survivors, dying within a month following its occurrence (Broderick et al., 1993).

We have chosen to focus on ischemic strokes due to several reasons. Firstly, ischemic attacks are much more common, result in more living survivors, and are considered more idiopathic compared to hemorrhagic strokes (Lawrence et al., 1998). While ischemia is, correlated with old age and gender, hemorrhagic stroke is more associated with high impact traumatic brain injuries, skull fractures, high blood pressure, arteriovenous malformation and tumours. In other words, the less lethal variant of stroke remains to be the most elusive in its

mechanism of action and its origin. The animal model of ischemia, therefore, serves as an ideal paradigm for studying the underlying mechanism of neuronal recovery following ischemia, in a manner which is easily reproducible and most relevant to the human population (Hossmann, 1998; Majde, 2003).

1.8 Changes following cerebral infarcts

As a consequence of cerebral anoxia, a necrotic core is created within the neuronal tissue, which includes dead neuronal, glial, endothelial and red blood cells. Due to their importance and relevance within the cerebral cortex, neuronal cell death is postulated to be the most important factor underlying the cognitive deficits seen patients following ischemia (Fiedler et al., 2011; Shea and Di Tullio, 2013).

Although it is undoubtedly a contributing factor, neuronal death is probably not the only cause of cognitive deficit following stroke; glial cell may also be involved. Glial cells loss could result in cognitive deficits due to the transient disintegration of the BBB, the protective layer around blood vessels that aids in preventing the entrance of harmful substances in the blood supply from entering the brain. While microglia would phagocytose, such substances should they enter the brain, their numbers are often reduced during cerebral infarction, making neuronal tissue more vulnerable to foreign substances. Furthermore, due to the impermeable nature of the BBB, the immune system is excluded from the brain; although, once ischemia occurs, nervous system gains access (Banks and Erickson, 2010). Thus, the disintegration of the BBB, although transient, could result in a whole range of other neurological and neuro-metabolic dysfunction following the onset of stroke, even when the stroke may have occurred some time ago (Nahirney et al., 2016; Sandoval and Witt, 2008).

Despite the dire consequences of stroke, researchers and health practitioners have documented extensive recovery in afflicted patients within months following the occurrence of ischemia (Langhorne et al., 2011; Schaechter, 2004). Some researchers have postulated a mechanism for this recovery in which surrounding functional tissue undergo a process of reorganization and can form new synaptic connections, fulfilling the functions of deceased neurons (Hama et al., 2011; Watila and Balarabe, 2015). Others have hypothesized that some of the more transient effects of a stroke that patients “recover” from are not so much due to changes in connections and circuitry of the brain, but due to decreased activity within neurons following the onset of stroke (Clarkson and Carmichael, 2009). This inactivity may be due to adaptive

attempts of these cells to lower their metabolic activity in times of low oxygen availability, to better ensure survival. Affected patients have repeatedly reported regaining control of their limbs, reacquiring sensation in various areas of the body, all of which were lost for some time following the onset of ischemia (Connell, 2007; Langhorne et al., 2009).

While some patients report that they are regaining of functions, others report the loss of functions, a phenomenon that has also been observed in animal models (Arundine and Tymianski, 2004; Martin et al., 1998). Such adverse post-ischemic effects are a common occurrence, with post-ischemic depression being one of the most prominent examples (Schepers et al., 2009). While some may attribute this depression to the circumstances that afflicted patients may find themselves in, others argue that the depression is merely a manifestation of the global hypoexcitability of neurons within the brain (Kim et al., 2014; Machado et al., 2009). As evidenced in the recovery of some individuals following cerebral ischemia, there may be a high number of synaptic regeneration and reconfiguration of physiological activity in the brain following the onset of stroke. While some may experience the rewiring of the brain in a way that is beneficial, some patients may experience physiological changes that may be harmful. Additionally, it is indeed possible that the buildup of neurotoxins within neurons due to the lack of circulation would result in additional neuronal casualties (e.g. buildup of reactive oxygen species)(Olmez and Ozyurt, 2012).

While thus far, many different theories have been discussed regarding the underlying mechanisms of stroke, limited conclusive empirical evidence has been obtained. The sheer number of possible hypotheses posed by researchers hints to the degree in which such processes are unknown. Indeed, a more in-depth view of the cellular nature of stroke and biochemical changes that occur therein needs to be undertaken.

1.9 Regions of stroke

Research on stroke has mainly focused on the characteristics of necrotic tissue and the outfall of cellular infarction (Ünal-Çevik et al., 2004). Recently, however, the area immediately surrounding the necrotic zone has been of interest to several laboratories (Li et al., 1998). This region, initially referred to as the injured region, was later renamed as the PI and is located 200-300 μm from the infarct border (Brown et al., 2007, 2008, 2009; Nahirney et al., 2016). The PI has garnered interest due to its injured but viable tissue morphology. One of the main characteristics of cerebral PI is that, unlike infarct tissue, it retains functional blood vessels and

circulation. Due to its viability and its higher degree of perfusion, this region has been hypothesized to be involved in neuronal recovery. This hypothesis has served as the driving force for much of the research being done in this region.

Researchers investigating the PI have taken two different approaches in their investigations. One approach has been in understanding the loss of neurons within the infarct and the PI, following the onset of stroke. Researchers taking this approach have utilized multiple different assays to visualize the degree of neuronal loss in the PI, compared to normally perfused tissue. Conventionally, these studies were only conducted on animal models; however, recent advances in neuroimaging techniques such as positron emission tomography, have allowed neuroscientists to visualize selective neuronal loss in human subjects.

Another approach taken in studying the PI has focused on the possible role of this region in recovery and rehabilitation. Researchers have been investigating the neuroplasticity and capability of these neurons to repair and recover from the damage they have endured during cerebral occlusion. Initial research within the PI attempted to assess the mechanism by which neuroplasticity within this region might take place. Reports of such research indicated that PI recovery follows a series of steps. The first step occurs following the occurrence of stroke, which involves the loss of neurons within the infarct region, and short dendritic neurons within the PI (Carmichael et al., 2017). Meanwhile, while spines maintaining proximal connections are lost, those maintaining distal connections remain intact; these longer spines (~1.40 μm) remain as the majority 6 hours following the occurrence of stroke. When allowed more recovery, however, medium length spines far outnumber long spines, which may be indicative of synaptic growth, turnover, or retraction (Brown et al., 2007). These different morphological changes have been attributed to the attempts of these remaining live neurons to establish new functional connections with synapses proximal to them while maintaining their distant connections. This remapping process possesses similarities to the process of synaptic pruning(Carmichael et al., 2017). It might be the case that longer spines remain stimulated by their healthier distal connections, and hence maintain their connections, while those of short or moderate size may no longer be receiving input. In sum, there seem to be multiple complex processes that take place following stroke, which may result in the synergistic recovery within the PI.

Animal models have been extensively used within this field of research due to the high degree of experimental control and manipulation that researchers can exercise (Bacigaluppi et al., 2010). Using animal models, neuronal activity can be compared before and after the stroke,

the location of the stroke can be manipulated, and the environment that the animals reside in (to control for environmental effects of stroke) can also be manipulated (Fluri et al., 2015). Focal occlusions have been induced within various model organisms using a variety of techniques for inducing stroke. Least invasive among these methods is the photothrombosis model. This method, originally developed by Watson *et al.* (1985), utilizes Rose Bengal, a photoactivatable dye, which upon activation at the appropriate frequency (532 nm), produces reactive oxygen species which damages nearby endothelial cells, recruiting platelets and initiating thrombosis, causing a blockage in blood flow with the area of activation. The methodology has since been improved and adapted for better care of the animals since its initial implementation, and it remains the most effective methodology to induce reproducible, minimally invasive, cerebral infarctions within the cerebral cortex (Labat-gest and Tomasi, 2013).

1.10 Mouse model of stroke

There are many benefits to the methodology of stroke described above, as it allows for a high degree of experimental control and accuracy. The focal nature of ischemia will result in better understanding of the widespread disruption and recovery in areas adjacent to the infarct zone. More importantly, however, the focal nature of this induced stroke allows for the infarct to be localized to one hemisphere, leaving the contralateral hemisphere intact. Many researchers using mouse models have utilized this to their advantage to compare affected tissue in one hemisphere, with tissue collected from the unaffected contralateral hemisphere of the same animal (Brown et al., 2008, 2012; Nahirney et al., 2016). This results in a high degree of control due to the within-animal design that has since been used in many biological experiments(Charness et al., 2012). Whereas in global ischemia, the afflicted mice would be compared with sham mice, focal and hemisphere specific induction of stroke allows for each animal to serve as its own control, eliminating any noise in the data due to individual differences (van de Pol and Wright, 2009; Yonekura et al., 2004).

Lastly, it is worth noting that the choice of the animal model is also important. Mice possess similar cerebral vasculature and neuronal physiology to humans (Ghanavati et al., 2014), and are closely related to humans from an evolutionary standpoint. Additionally, due to the large number of publications using this animal model and their easily manipulated genome (i.e. transgenic cell lines), the use of mice has often become a necessity for researchers in neuroscience. Mice are by far the primary animal model used for studying stroke (Casals et al.,

2011), and hence this thesis has also utilized mice as the animal model, not only to allow comparison with previous studies but to also take advantage of the convenience provided by this animal model.

1.11 Focal cerebral infarct within the SSC

Throughout the primate evolutionary lineage, the SSC has held on to its core function: processing of tactile information (Beck et al., 1996; Kaas et al., 1979; McGeoch et al., 2015). The SSC, located in the region immediately posterior of the central sulcus in the primate brain, is often known as the primary somatosensory cortex (S1). The numerical value associated with this area is due to its primary and hence essential functions in detection and locating the area of sensation. Briefly, S1 is involved in the following types of sensation: proprioception, thermoception, nociception, tactile and textual features, and shape information (Friedman et al., 2004). S1 receives dense inputs from the thalamus regarding sensory information, information that it then relays following processing, to higher association areas, such as the secondary somatosensory cortex (S2). Higher sensory processing and incorporation of sensory data then takes place (Weisz et al., 2014), ultimately leading to motor action.

Due to its central location within the anterior regions of the parietal lobe, immediately following the post-central gyrus, the SSC is commonly the site of cerebral infarction (Ng et al., 2007). Most ischemic attacks occur due to a blockage of the medial cerebral artery, the main artery that supplies the cortical and subcortical structures of the cerebrum (Engel et al., 2011). Cerebral infarction is often spread over the primary SSC and the primary motor cortex, due to the close proximity of the two regions. Located on either side of the central sulcus (Kaas, 2004; Seitz et al., 1998). Ischemic epidemiology therefore almost always includes a loss of sensation and motor function of various areas within the body following the onset of stroke.

There are significant benefits in the induction of stroke within the somatosensory or even the sensorimotor cortex.This is due to the underlying nature and organization of the sensorimotor gyri. Specifically, both the primary motor cortex and the SSC are somatotopically organized (Kaas et al., 1979). In other words, both areas contain distinct regions with populations of neurons that are responsible for motor acts and sensory information associated with specific areas of the body. Many neuroscientists have thoroughly researched somatotopic mapping, and these findings have allowed others in this field to observe the changes (Winship and Murphy, 2009) in the somatotopic organization of the sensorimotor cortex following ischemia. In fact,

such studies on somatotopic mapping and remapping provide the most substantial support for the presence of remapping processes within the PI. This is because following several weeks of recovery, PI neurons initiate responding to sensory and motor stimulation that were previously associated with neurons within the necrotic regions (Brown et al., 2008; Tennant et al., 2017). Thus, the sensorimotor cortex provides clear advantages in terms of its location and its function for the induction of stroke and the photothrombotic paradigm.

With regards to the induction of ischemia, the SSC provides a convenient option due to the ease of accessibility of cortical regions (Engel et al., 2011; Labat-gest and Tomasi, 2013). Although research has been done on the PI and necrotic tissue of subcortical structures within model organisms, such experiments entail complicated surgical procedures due to their location (Umegaki et al., 2005). There is also a higher degree of difficulty in inducing focal ischemia, due to the presence of more integral vasculature within subcortical regions with widespread branches that feed into more superficial cortical regions. Regardless of these differences, researchers using the subcortical model of stroke have reported previously mentioned phenomena common to cortical ischemia which include cellular penumbra, transient peri-infarct depolarization (PID), and higher levels of excitability (Umegaki et al., 2005). Thus, the sensorimotor cortex is often the target region for the induction of cerebral ischemia, due to its superficial location, ease of access, and since it is the region in which cerebral infarction most often occurs.

1.12 Characteristics of the PI

The presence of pyknotic nuclei along with the loss of functioning and identifiable capillaries, serve as clear signs of infarct tissue. Markers of the PI, located approximately 200 μm from the infarct border, include the overwhelming presence of white blotches, which may have been functioning dendritic or astrocytic processes before the stroke. A loss of perfusion and cellular density are also common occurrences. Within light microscopy studies, apperant differences can be seen between the PI located proximal ($\leq$ 100 μm) to the infarct border and areas distal (>100 μm) to it. There are much more prominent sightings of white blotches and aberrant dendritic and vasculature as a function of proximity towards the infarct border. More microscopic features of the PI can be spotted in EMs. One of the most prominent indicators is the glycogen buildup within astrocytes and the enlarged mitochondrial lumen, a feature that is present across different cell types, but especially noticeable in astrocytes. Less prominent

markers include the overall swelling of astrocytes within the PI and the inflammation and disintegration of BBB components surrounding the functioning capillaries within this region. Within the infarct region, similar blotches and aberrant cellular structures and their surroundings can be seen, as was shown previously in brightfield images. There are hardly any discernable capillaries and cellular structures within this region. The few cellular structures that are found are almost always pyknotic nuclei.

1.13 Rationale

Little is known regarding the morphological consequences of cerebral ischemia within the necrotic core. Little is known about the morphological and structural features of the PI. The benefit that can be derived from the results of this thesis are threefold. Ultrastructural differences between the PI and control tissue may provide insights regarding critical structural features that are necessary for proper neuronal functioning, as facilitated by synaptic communications. Study of the PI and its morphology may provide further insights into the morphological underpinnings of cortical remapping. Lastly, the findings of this thesis provide clues as to the mechanism by which cellular organelles and synaptic structures (e.g. postsynaptic density) change as a result of ischemia. By focusing on the PI, this thesis can address the effects of ischemia on viable yet affected neurons. With the aid of high-resolution microscopy, characteristics of such changes in microscopic structures can be observed and quantified.

Methodology

2.1 Materials and methods

All animal procedures were performed in accordance with the animal care protocols set forth by the University of Victoria Animal Care Centre and the Canadian Council on Animal Care. Photothrombotic stroke was induced by Dr. Craig Brown and Dr. Patrick Reeson (University of Victoria, Victoria, BC, Canada). The methodology of the stroke is detailed in the following section. Samples from five adult mice (variable ages: 3 months and 18 months) were used for both contralateral and ipsilateral (stroke containing hemisphere) comparisons for intra- and inter-animal analysis. All mice were subject to photothrombotic stroke and allowed 72 hours of recovery prior to sample collection.

2.2 Stroke within the SSC

Focal unilateral stroke was induced within the SSC corresponding to the forelimb region based on previous research by Watson et al. (1985) and further adjusted for the purposes of this thesis. Ischemia was induced via photochemical activation of disodium tetraiodo-tetrachloroflurescein, commonly known as Rose Bengal, which then initiates a cascade of reactions resulting in *in vivo* platelet aggregation in the blood vessels (Labat-gest and Tomasi, 2013). Although the original methodology developed by Watson et al. (1985) was catered to photothrombosis in rats, the methodology has since been adopted to utilize this technique in other organisms.

Initially, mice were anesthetized using 1.5% isoflurane in medical air with a flow rate of 0.7 L/min. They were then fitted to a stereotaxic frame for the remainder of the procedure. Body temperature was maintained via the use of a heating blanket, with a feedback rectal thermometer, allowing for the stabilization of the organism's body temperature at 37ºC. Essentially, the goal of this initial step was to stabilize the organism and to maintain appropriate body temperature in order to minimize the harm to the animals (beyond the scope of experimental manipulation).

Following stabilization, the organisms were prepared for photothrombosis. The area where the laser light would be applied was marked, following the retraction of the scalp. The marked area of the skull was then thinned using a dental drill, to approximately 50% of its original thickness. It has been shown previously that the skull would be sufficiently translucent to green light (originally tested with 560 nm light) and would be able to transmit photochemical

activation of Rose Bengal (Watson et al., 1985). This makes this method of induction a non-invasive technique since the green laser replaces the need for craniotomy.

Green laser (532 nm in this method, 17 mW power light, 1.5 mm diameter light Beta Electronics) was applied for 15 minutes to the thinned square region of the skull (1.5 x 1.5 mm) five minutes following intraperitoneal (into the visceral cavity) injection of Rose Bengal. The amount of Rose Bengal administered to each animal was based on a 110 mg/kg (weight of Rose Bengal over weight of the animal) formula. Following surgery, close monitoring of heart rate and body temperature of each animal took place. Mice were then returned to their home cages for recovery.

2.3 Perfusion, fixation, sectioning, and microdissection

Recovery was allowed for 72 hours following the induction of ischemia; the mice were exposed to isoflurane for deep anaesthetization. Securing the animal using dissecting pins, an incision was initiated at the mouse's belly. The incision was then continued upwards towards the thoracic cavity ending at the throat. Following exposure of peritoneum tissue, the abdominal cavity was exposed while carefully displacing the liver to the side as to prevent damage. Exposing of the abdominal cavity yielded access to the beating heart. The left atrium and ventricle were first identified, and following identification, the left ventricle was penetrated using a butterfly needle. Subsequently, transcardial perfusion using heparinized phosphate-buffered saline (PBS) was conducted for a 5 minute duration. The loss of colour seen in the liver was used as an indicator regarding the adequate circulation of heparin. The needle was then used to allow the passage of 75 ml of fixative containing 2% glutaraldehyde and 2% paraformaldehyde in 0.15 M cacodylate buffer throughout the circulatory system. The fixative was administered at a slow rate to ensure maximum tissue preservation; therefore, the administration of the entire solution lasted approximately 10 minutes. The fixative solutions were obtained from Electron Microscopy Sciences, Hatfield, PA, USA.

Organs were then extracted and left in fixative for 24 hours at a temperature of 4ºC. Following the 24-hour period, the brain was cut into 200 μm thick coronal sections using a vibrating microtome (Leica model VT1000S). Coronal sections containing the SSC were microdissected into 1 mm^2 tissue blocks. Microdissection was carried out under a stereomicroscope (Olympus SZ61 Dissecting Microscope) accompanied with flexible fibre optic lighting. Tissue was collected from both hemispheres of the brain and organized into separate

compartments: stroke and non-stroke tissue. Post-fixation of the samples was conducted based on the traditional osmium tetroxide-potassium ferrocyanide (OsFeCN) staining technique for electron microscopy samples: 1% osmium tetroxide-potassium ferrocyanide solution in sodium cacodylate buffer solvent was applied to the samples for 2 hours at room temperature while on a rotating mixer. The samples were then rinsed twice with deionized water.

Samples were *en bloc* stained with 2% uranium acetate (aq) for 2 hours on a rotating mixer. Dehydration was then performed by immersing the sample in ascending ethanol (50%, 70%, 80%, 95%, 100%) concentrations, with 15 minutes for each ethanol concentration except when using 100% ethanol; the samples were exposed to 100% ethanol mixture twice for 30 minutes.

Due to the presence of epoxide in the infiltration solutions and their relatively robust hydrolysis, the post-fixation and dehydration processes were conducted under the fume hood at atmospheric moisture levels. Sample infiltration using a 1:1 (v/v) mixture of 100% ethanol and Spurr's Low Viscosity resin (containing: Cycloaliphatic Epoxide Resin, diglycidyl ether of polypropylene glycol, nonenyl succinic anhydride dimethylaminoethanol), obtained from Electron Microscopy Sciences, for one hour was then induced. The samples were transferred to Spurr's resin overnight onto an angled rotating mixture. Approximately 12 hours later, samples were mixed with Spurr's resin once again before being embedding in BEEM capsules (BEEM Incorporated, West Chester, PA, USA).

2.4 Light microscopy sectioning

Glass knives were used for the acquiring of semithin sections (~0.5 μm) on Reichert-Jung UltraCut E Ultramicrotome. The sections were then stained with toluidine blue (aq) for light microscopy imaging and inspection. The sections were collected on standard microscope slides and coverslipped using Cytoseal mounting medium.

2.5 Light microscopy imaging

Scale bar calculations were conducted using calibration imaging data obtained from the Nahirney Laboratory. Images of light microscopy slides were taken using Olympus BX51 brightfield microscope and Olympus DP73 digital camera set at 4800 by 3600 pixels resolution. Images were used for qualitative purposes focusing on the overall characteristics of ischemic and control tissues. Images were captured using the 20x and 40x objectives. Based on the acquired

toluidine blue sections, tissue samples were trimmed down to smaller areas using a razor blade for ultrathin sectioning and electron microscopy analysis.

2.6 Transmission electron microscopy sectioning

Following trimming of samples for ultrathin sectioning, 70 nm-80 nm sections were acquired using a diamond knife (Diatome) and transferred onto 200 hex copper mesh grids, obtained from Electron Microscopy Sciences (see Figure 8).

2.7 Transmission electron microscopy imaging

Replica carbon grid images (Electron Microscopy Sciences), obtained previously in the Nahirney laboratory, were used for scale bar calculations for all images and magnifications. Samples were surveyed using a JEM-1400 (JOEL) transmission electron microscope, and images were captured with an Orius SC1000 digital camera (Gatan) set at 4008 by 2672 pixels resolution (Gatan Digital Micrograph software was used for controlling the digital camera, capturing images using the camera, and saving of acquired images).

The PI (defined as <200 μm from the infarct border) located in the ipsilateral ischemic hemisphere were imaged. The contralateral non-ischemic tissue of the same mice were also imaged. In total 10 hemispheres were inspected. For quantitative analysis (see below) a total of 10 images were used for each mouse, yielding a total of 50 test field images.

Several regions and neuronal structures were imaged throughout data collection. Images of pyramidal neurons and their associated dendritic processes were imaged from both hemispheres for qualitative purposes. These images were captured at lower magnifications, to ensure that all visible processes of neurons were captured. Additionally, images of capillaries and the

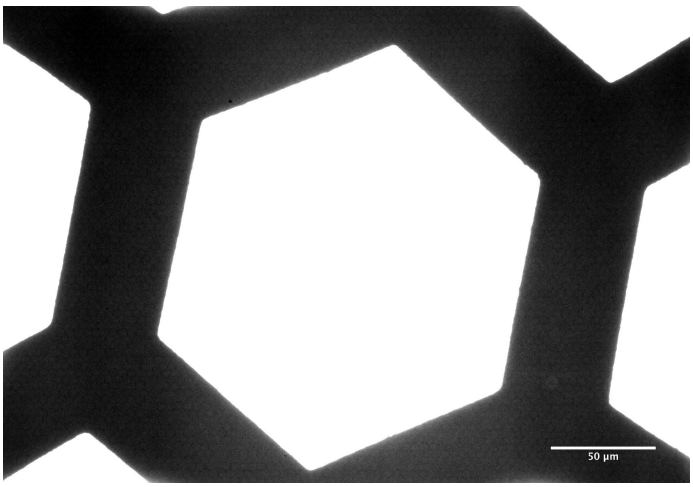

Figure 8: EM of a single mesh belonging to a 200-hex copper mesh grid
Coated with a thin layer of carbon, mesh grids are commonly used as a platform for tissue visualization within the electron microscope. 200 mesh grids allow imaging of small sections, since a higher number of hexagons are available to support the sample.

surrounding structures were also taken at low magnification (~ 5,000x magnification) for qualitative analysis (see Appendix A). Within the PI, the integrity of the capillaries, along with associated astrocytic endfeet, were used as qualitative indicators of the PI.

Synaptic regions were imaged at 30,000x, 40,000x, 50,000x, 60,000x, 80,000x magnification. Synaptic regions were imaged randomly, approximately within (<100 μm) of capillaries. For quantitative analysis, only images captured at 30,000x magnification were used. In some cases, following the identification of neuronal (neurons showing apical dendrites, axosomatic synapses, viable neurons within the PI zone, and identifiable neurons within the infarct zone) and synaptic structures (e.g. defined synaptic cleft, postsynaptic density, presynaptic density, vesicles within the active zone), images were captured at higher magnifications (i.e. 40,000x, 50,000x, 60,000x, 80,000x) for qualitative analysis.

2.8 Quantitative analysis

Morphometric analysis was conducted on images captured at 30,000x magnification, located near capillaries (but no capillaries in the images themselves), and without the presence of any neuronal cell bodies within the test field. The test field area was found to be 6.58 by 4.39 μm (28.89 μm^2) at this magnification.

A total of 50 images were used for quantitative analysis, 5 images captured from each hemisphere. The intra-animal analysis consisted of comparing images from the contralateral and ipsilateral (ischemic) hemispheres of each mouse, while, the inter-animal analysis was done by averaging the means calculated for each mouse. The latter was done in an attempt to control for the limitations of the repeated measures design and to obtain additional information about the variability that exists across the animals.

2.10 Synapse identification criteria

Synaptic count per test-field was one of the measures that were quantified in this study. Compared to recent research conducted on synaptic morphology (Burette et al., 2015), a more lenient criterion was utilized for the identification of synapses. The following structures were categorized as synaptic structures (see Figures 9, 10 and Appendix A): round clear-core vesicles, flattened clear-core vesicles, postsynaptic density, spine apparatus, presynaptic density, synaptic cleft, vesicles within the active zone, and multivesicular bodies. Certain characteristics were considered more important in the decision-making process. A simple point system was

constructed to aid with the identification process (see table 1). If the structures had a combined score greater than or equal to five, then the structure was counted as a synapse. If their score was lower than five, they were not counted as synapses and not incorporated in the quantification process of synapse density per test field. Synapses with synaptic clefts touching the left or the bottom side of the image were also not counted.

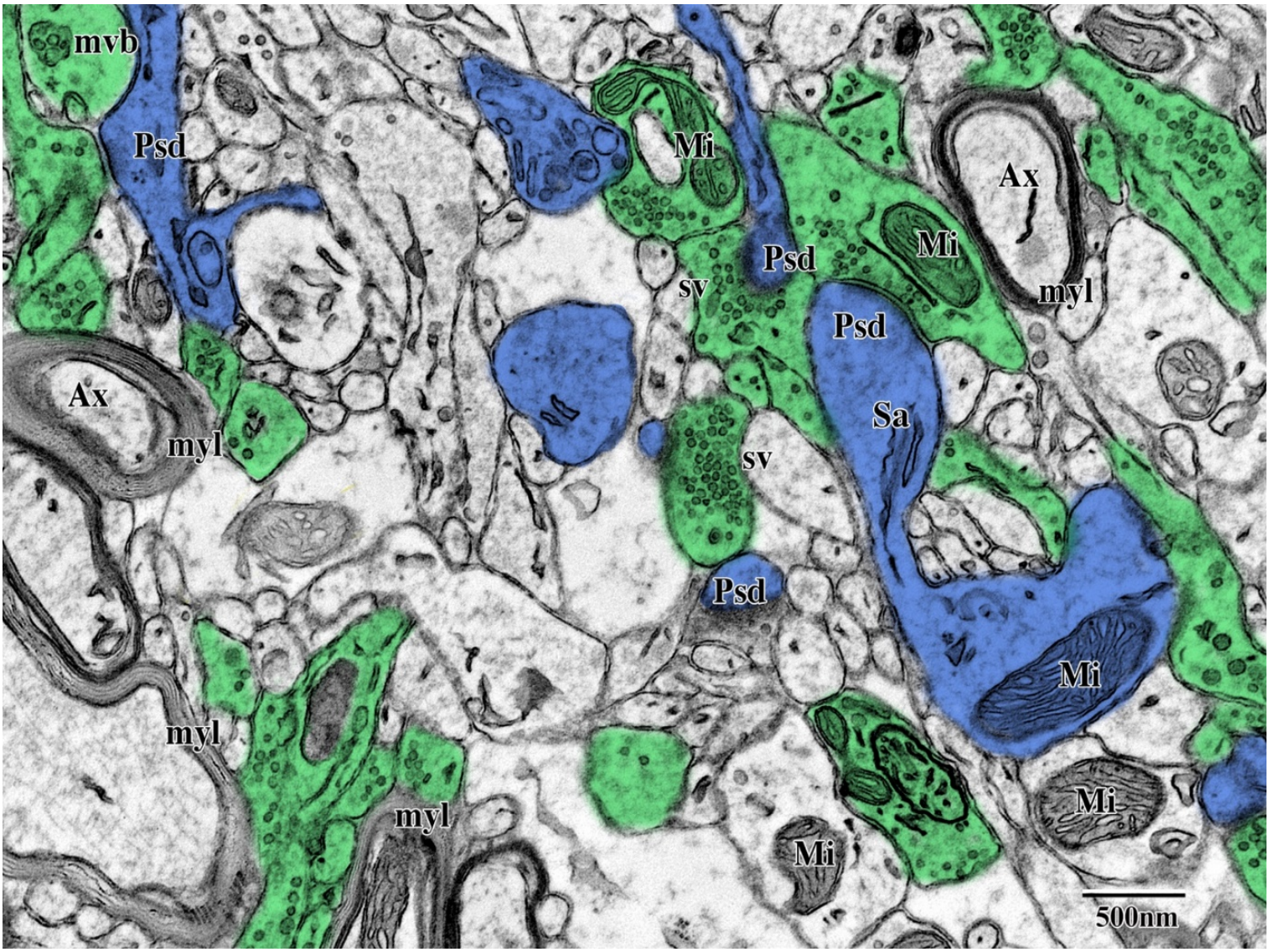

Figure 9. EM of synaptic structures located with layer 5 of adult mouse SSC.
Postsynaptic (blue) and presynaptic structures (green) were identified based on criteria and pseduocoloured. All synapses were identified as excitatory synapses, most of which exhibited postsynaptic densities and round clear vesicles. Ax, axon. Mi, Mitochondria. myl, myelination. mvb, multivesicular bodies. Psd, postsynaptic density. Sa, spine apparatus. sv, synaptic vesicles. Syc, synaptic cleft.

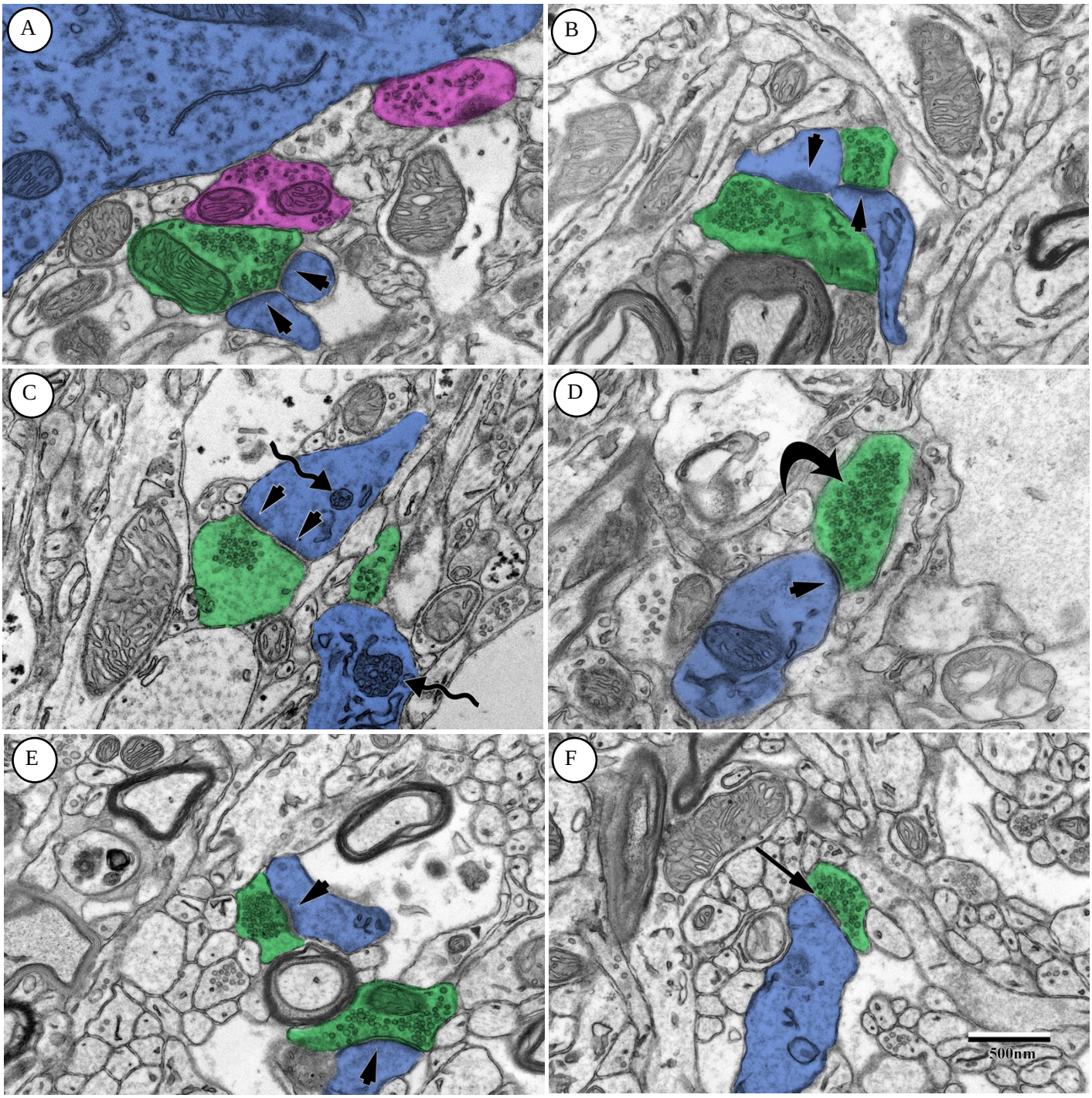

Figure 10. High magnification EM of synaptic structures found in layer 2-5 of adult mouse SSC cortex. Presynaptic structures for inhibitory synapses (purple) and excitatory synapses (green) were pseudocolored along with the receiving postsynaptic terminal (blue). (A) shows axosomatic inhibitory synapses and axodendritic excitatory compound synapse with postsynaptic densities (short arrows). Inhibitory synapses contain flattened vesicles. (B) shows excitatory synapses with large postsynaptic densities. (C) a perforated synapse with two postsynaptic densities is shown. Postsynaptic structure includes a multivesicular body (wavy arrow). (D) shows an excitatory synapse with a clearly visible synaptic cleft and round synaptic vesicles (curved arrow). (E) contrasts excitatory synapses with varying degrees of postsynaptic densities and clarity of synaptic cleft. (F) exhibits another example of clear synaptic cleft (arrow).

Table 1: Quantified identification criteria for synaptic structures

Based on the criteria detailed above, a point system was introduced for synaptic identification to make the identification process more objective. Points were assigned according to the prominence and the frequency in which such structures are seen at synapses. Structures with a score ≥ 5 were identified as synapses and included in related analyses. A total of 13 points possible

Structure	Points attributed to structures
round core vesicles	2
flattened core vesicles	2
presynaptic density	2
postsynaptic density	2
presence of delineated synaptic cleft	2
vesicles within the active zone	1
spine apparatus	1
multivesicular bodies	1

2.11 Synaptic vesicle count

Vesicles were identified as such if they possessed both of the following characteristics: clear/transparent core along with a completely visible membrane along the perimeter of the vesicle (see figure 11). From every analyzed test field, three presynaptic terminals were randomly selected and the vesicles bound by the presynaptic terminals were counted.

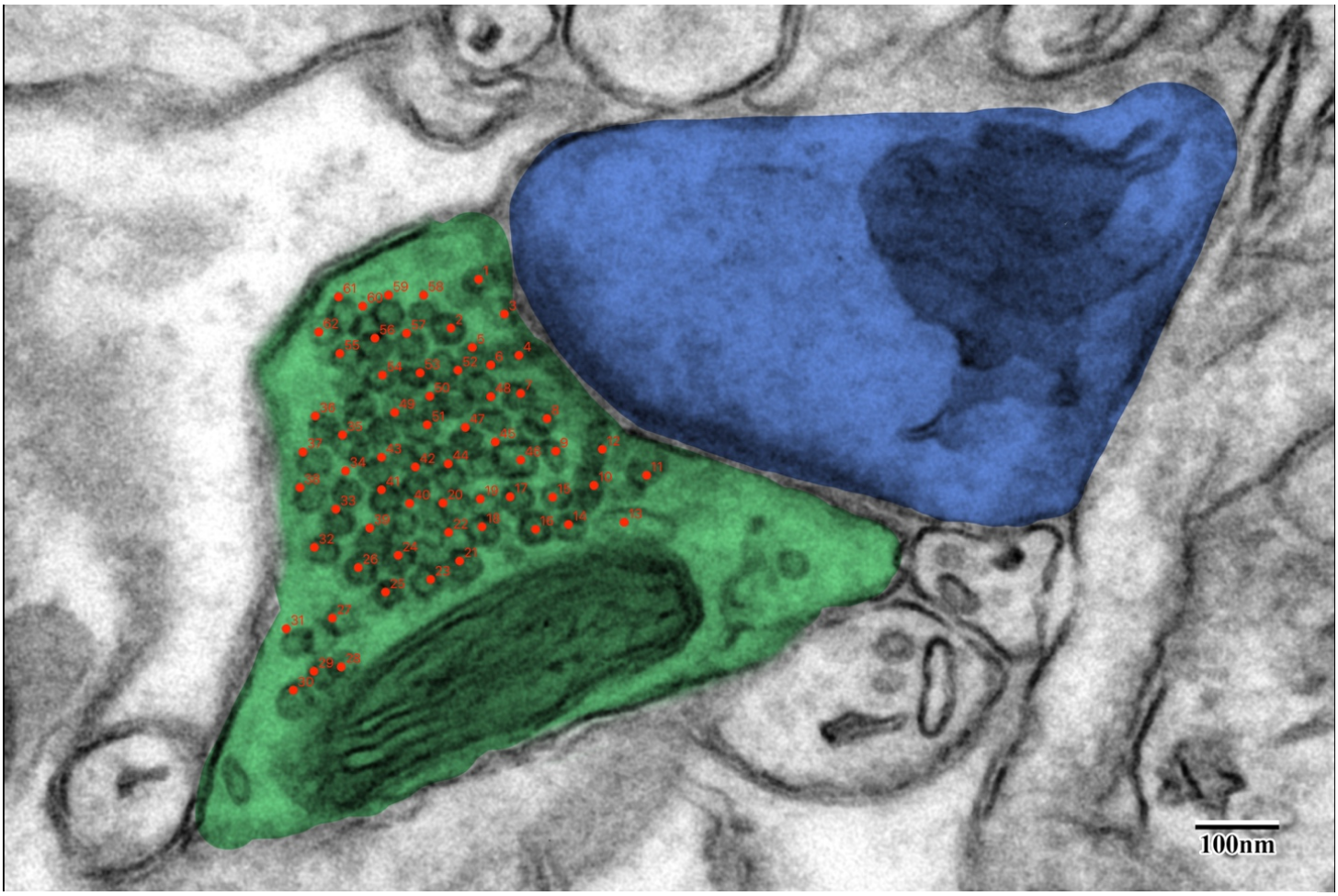

Figure 11: High magnification EM with synaptic vesicle count

Vesicle were counted within the presynaptic terminal. Only those enclosed within the presynaptic terminal; directly apposing the postsynaptic terminal were counted. Vesicles not located within the active zone, were not counted. Based on this criteria, a total of 62 vesicles were identified and counted in this image. Image taken at 120,000x magnification.

2.12 Criteria for Identification of Other Structures

Several synaptic and neuronal structures were identified and incorporated for analysis based on specified criteria. Regions occupying vesicles were quantified as presynaptic regions and incorporated in area analysis, while regions opposing presynaptic terminals (as laid out by the criteria) were identified as postsynaptic terminals. Mitochondria were identified solely based on the presence of membrane-enclosed cristae (see Appendix A). Structures with lighter staining mitochondria that also possessed intermediate filaments were classified as astrocytes. Either characteristics (i.e. lighter mitochondria or characteristic filaments) were determined as sufficient markers of astrocytes. Astrocytes located within the PI also exhibited large amounts of glycogen granules, which was used as an additional marker for astrocytes. Lastly, postsynaptic densities were identified as dense regions directly opposing the presynaptic membrane and encapsulated by the post-synaptic terminal. Following identification of structures based on their respective characteristics, areas occupied by presynaptic and postsynaptic terminals, mitochondria, astrocytes, and postsynaptic densities, were traced with Photoshop (Adobe). Thresholding of images was followed by the measurement of the traced area (calculated using ImageJ).

2.13 Statistical analyses

Different levels of analyses were conducted with the obtained results. To begin with, the differences in counts and areas measured were compared across control and stroke hemispheres for each mouse; mean values within each category were calculated for each hemisphere and compared using a paired/dependent samples t-test. Following intra-animal comparison, condition means for contralateral and ipsilateral (stroke) hemispheres were averaged across all mice (contralateral and ipsilateral were averaged independently). For measures (i.e. areas and counts) in which the cumulative means (mean of means) comparison was found to be significant (or four out of five mice showed significant differences within a particular category), the additional intra-condition analysis was conducted and tested for significance using one-way ANOVA statistical testing. Post-hoc statistical testing was also conducted (Tukey's test). These statistical tests were utilized as a way to ascertain whether significant differences can be attributed to individual variability. Due to the lack of studies on this topic, and the blindness of the experimenter to the directionality of data (e.g. smaller or larger values for one condition vs. another), a two-tailed hypothesis was set in place for all tested measures. For all quantitative and statistical analysis, Excel (Microsoft) and XLSTAT-Pro (Addinisoft) software were used, respectively.

Results

3.1 Qualitative analysis: light microscopy

Changes can be observed when comparing control and ischemic tissue (see figure 16). While control tissue shows adequate perfusion, ischemic tissue embodied deteriorating levels of perfusion (high to low levels of perfusion as a function of proximity to the necrotic core). Similarly, while perfused tissues exhibited high neuronal densities, stroke tissues showed much lower levels of cellular density, which is progressively lowered as a function of proximity to the necrotic core

Additionally, when comparing PI and control regions, a similar neuronal density is observed (see figure 19). However, neurons within the PI zone exhibit visibly aberrant and variant structures (i.e. elongated thin cell bodies, enlarged cell bodies with no dendritic processes, smaller nuclei to cell body area ratio). PI maintains some similarity to control tissue in that they have retained functioning capillaries. In contrast, capillaries (and their remnants) within the necrotic core seem to have entirely degenerated, to the point that their structure is not discernable. Despite the functioning capillaries, however, the PI often contains capillaries with abnormal morphology, and visible signs of disruption (i.e. pericyte show swollen morphology, vacuolization within and around disintegrated tight junctions of the endothelial cells).

Three distinct layers were defined within ischemic tissue sections. The intact zone showed perfusion levels similar to that of the contralateral region. The PI, defined as the area with reduced perfusion that show recognizable non-occluded capillaries. White blotches and frothy morphology permeate this region, increasing with proximity to the necrotic core. Finally, the necrotic core was defined as the area where no identifiable cerebral vasculature could be found. Any recognizable capillaries within this region were occluded with red blood cells.

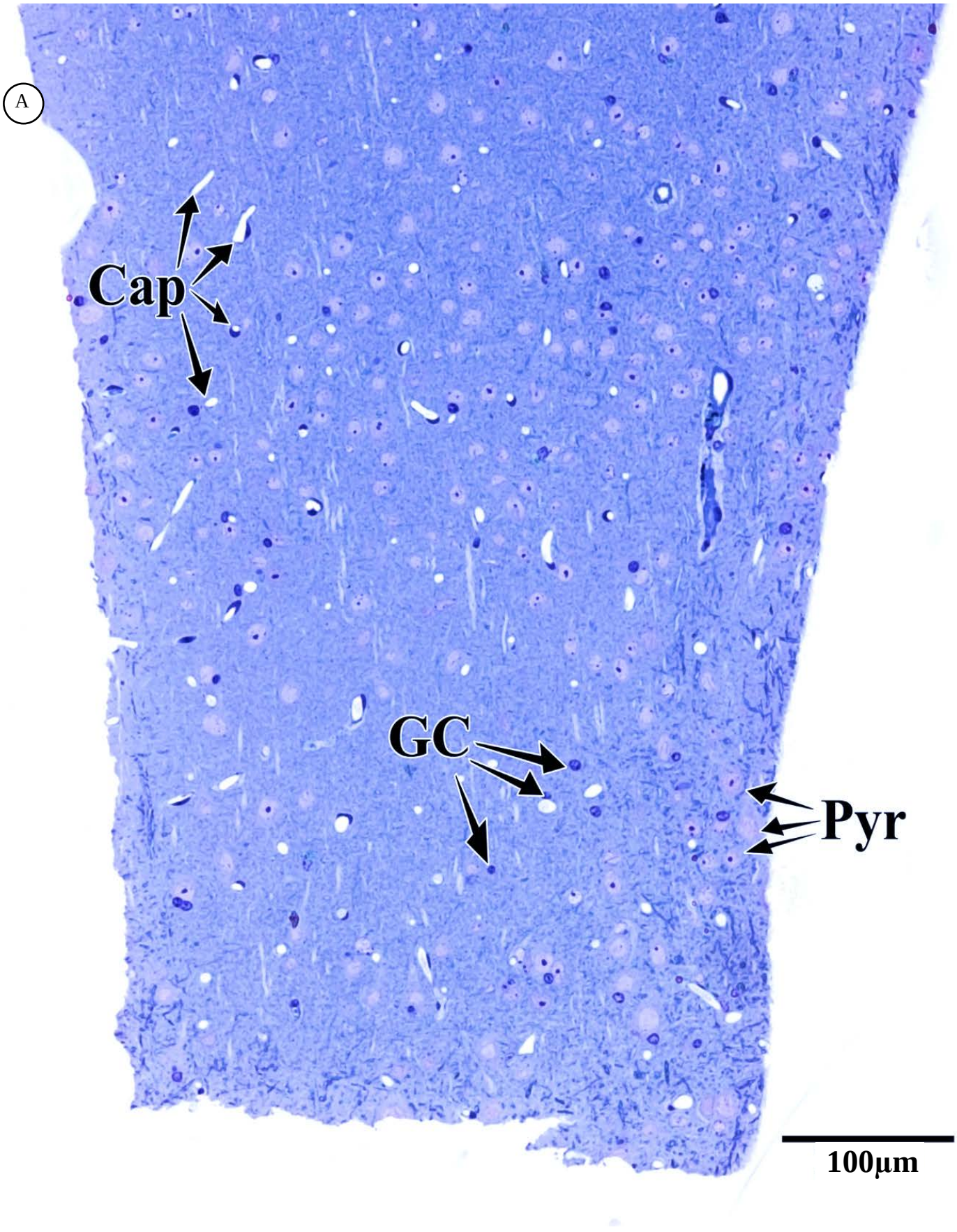
A
Cap
GC
Pyr
100µm

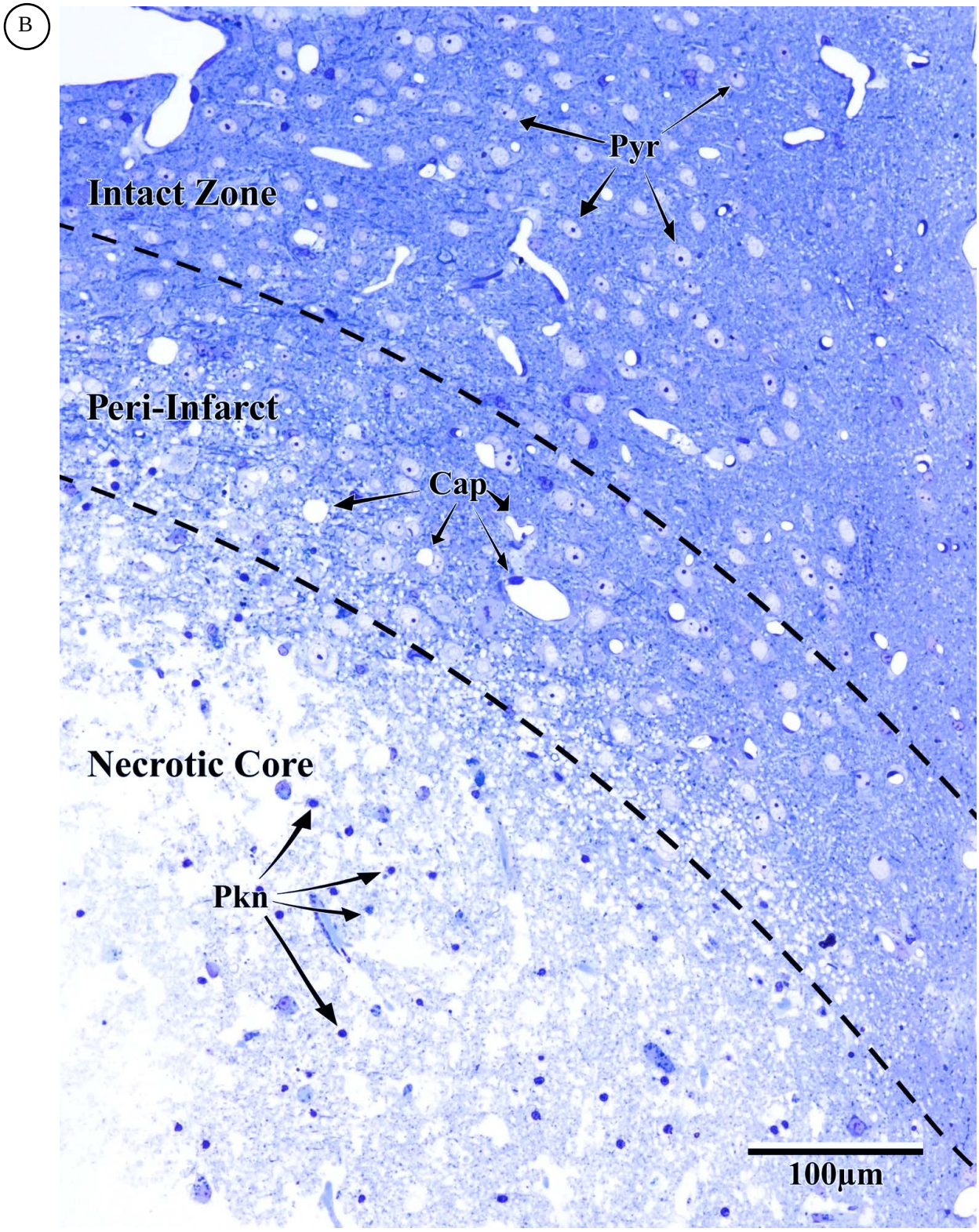

Figure 12. Low magnification toluidine blue-stained sections of control (A) and ischemic (B) tissue within layer 3-5 of the adult mouse SSC

(A) exhibits consistent levels of perfusion, with relatively consistent pyramidal (Pyr) and glial cell (GC) size. Similar orderly and consistent morphology can be within capillaries (cap). (B) shows a gradual lack of perfusion within tissues, with high levels of perfusion within the intact zone, and little to no perfusion within the necrotic core. The dotted lines denote the approximate location of the border that exists between the intact, peri-infarct, and necrotic zone. Cap shows irregular and varieble sizes within the PI, while no such structures can be seen in the necrotic core. Collapsed cellular structures referred to as Pyknotic nuclei (Pkn) signify the severity of degeneration at the infarct core.

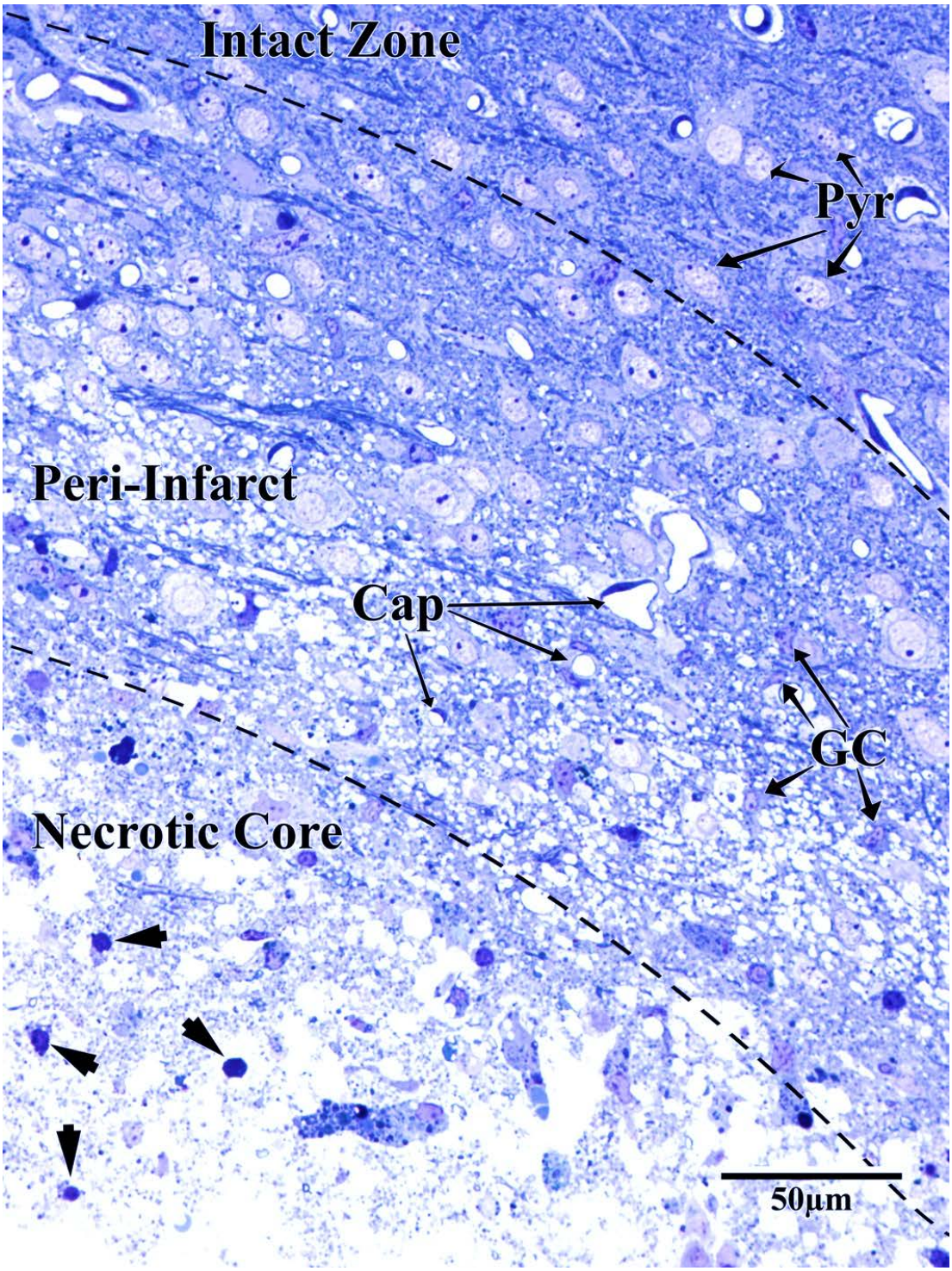

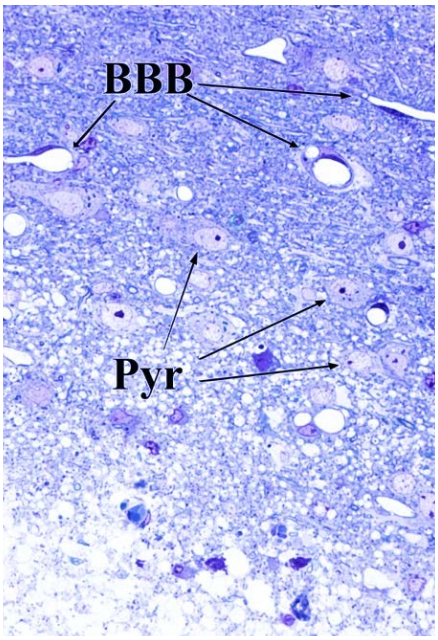

Figure 13. High magnification toluidine blue-stained section of ischemic tissue within the SSC (Left) shows the 3 regions commonly seen near the edge of the necrotic focal point. (Left) shows a gradual decrease in perfusion and decreased concentration of pyramidal (pyr) neuron with increasing proximity to the infarct border. Pyknotic nuclei (short arrows) presenting with collapsed and shrunken nuclei can repeatedly be observed within the nectoric core. (Right) focuses exclusively on the PI which exhibits loss of perfusion accompanied by a substantial decrease in the number of recognizable capillaries (Cap) in the region proximal to the infarct border. Compromised morphology of the BBB can be implied due to the presence of vaculoes surrounding functioning blood vessels.

3.2 Qualitative analysis: EMs

EMs confirmed all qualitative observations from light microscopy images. Aberrant dendritic structures reported in light microscopy images, and their relative increase with increased proximity to the necrotic core. Aberrant neuronal processes appear hollow, mainly due to the absence of any organelles or cytoskeletal structures. Also, even when subcellular structures were seen (i.e. mitochondria and spine apparatus), they often showed characteristically inflamed or even exploding/disintegrated structures.

Beginning at 4,000x magnification (see figures 14-17), differences can be seen between PI and control tissue. Whereas normal tissue exhibited an organized arrangement of cellular structures (in comparison to the prototypical neuron) with typically sized subcellular structures and organelles, the PI showed a high level of disorganization typical of damaged tissues such as organelles (swollen mitochondria), along with unrecognizable neuronal/glial processes devoid of any intracellular structures. At higher magnifications (i.e. 8,000x and above), changes were observed within astrocytes. While in healthy tissue very little sign of glycogen buildup can be seen within the astrocytic cytoplasm, vast amounts of glycogen granules were observed in astrocytic structures in the PI.

Interestingly, very noticeable differences can be seen when comparing the PI with tissue from the necrotic core. While organelles and subcellular macromolecules are noticeable in the PI, very little evidence for such structures can be seen within the infarct tissue. There is a pervasive presence of hollow dendritic structures along with an increase in unidentifiable structures. Additionally, there appears to be a lower number of glycogen granules within astrocytes located in the infarct region compared to those of the PI.

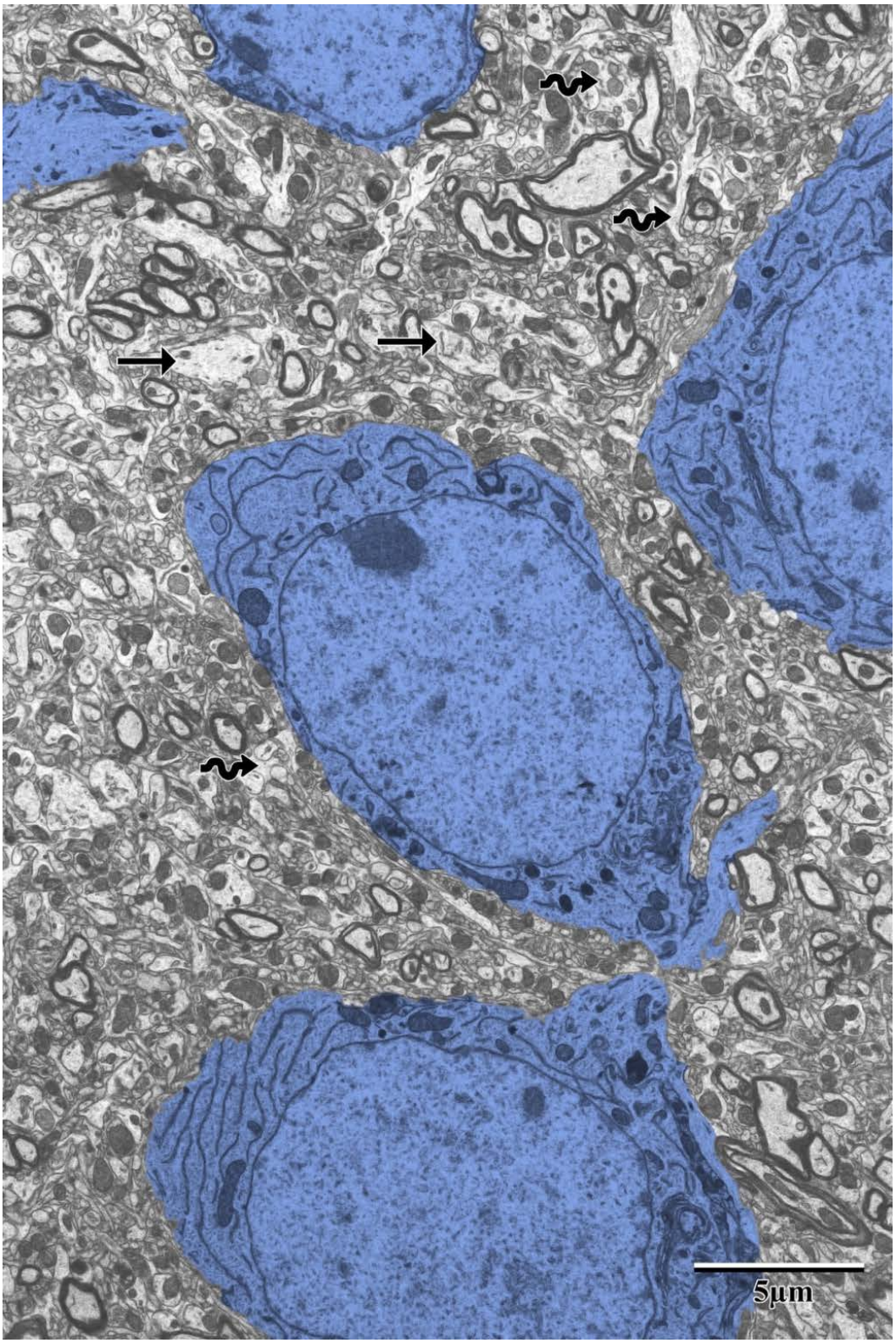

Figure 14: Pyramidal neurons within the contralateral SSC of adult mouse. Within layer 5 of the SSC, pyramidal neurons (blue) exhibited round and wide morphology. Cellular processes (arrows) show clear signs of organelle and cytoskeletal structures. Astrocytes (wavy arrow) show a clear morphology and occupy a relatively limited space.

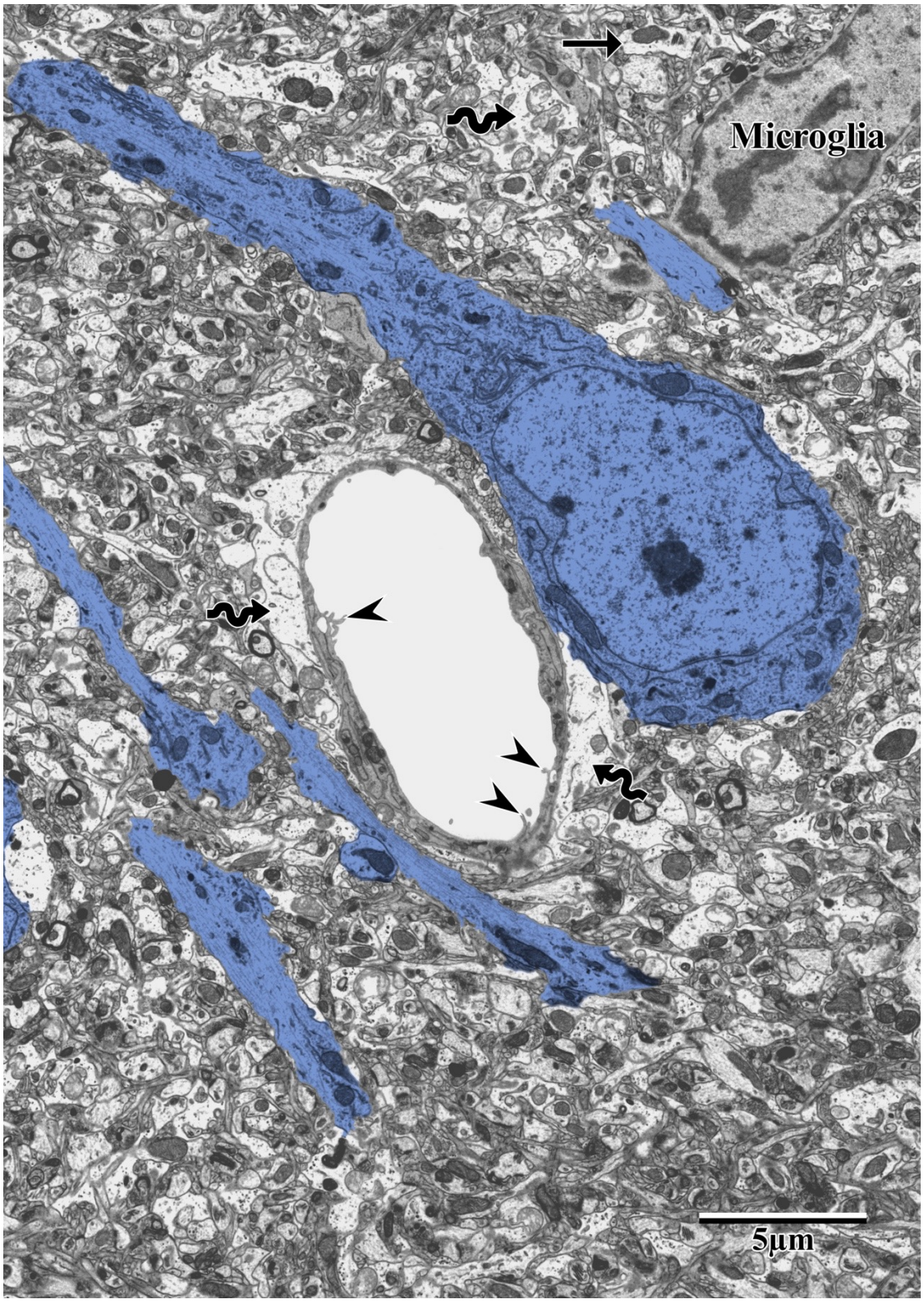

Figure 15: Pyramidal neurons located within the distal PI.
Pyramidal neurons (blue) located within layer 3 of the SSC exhibited elongated morphology. Cellular processes (long arrows) show clear signs of organelle and cytoskeletal structures, at levels comparable to control tissue. Astrocytes (wavy arrow) show clear but swollen morphology, with the addition of small concentrations of glycogen granueles not visible in control tissues. Endothelial tight junction (arrowheads) disintegration, along with formation of vacuoles, can be seen along the perimeter of the capillary.

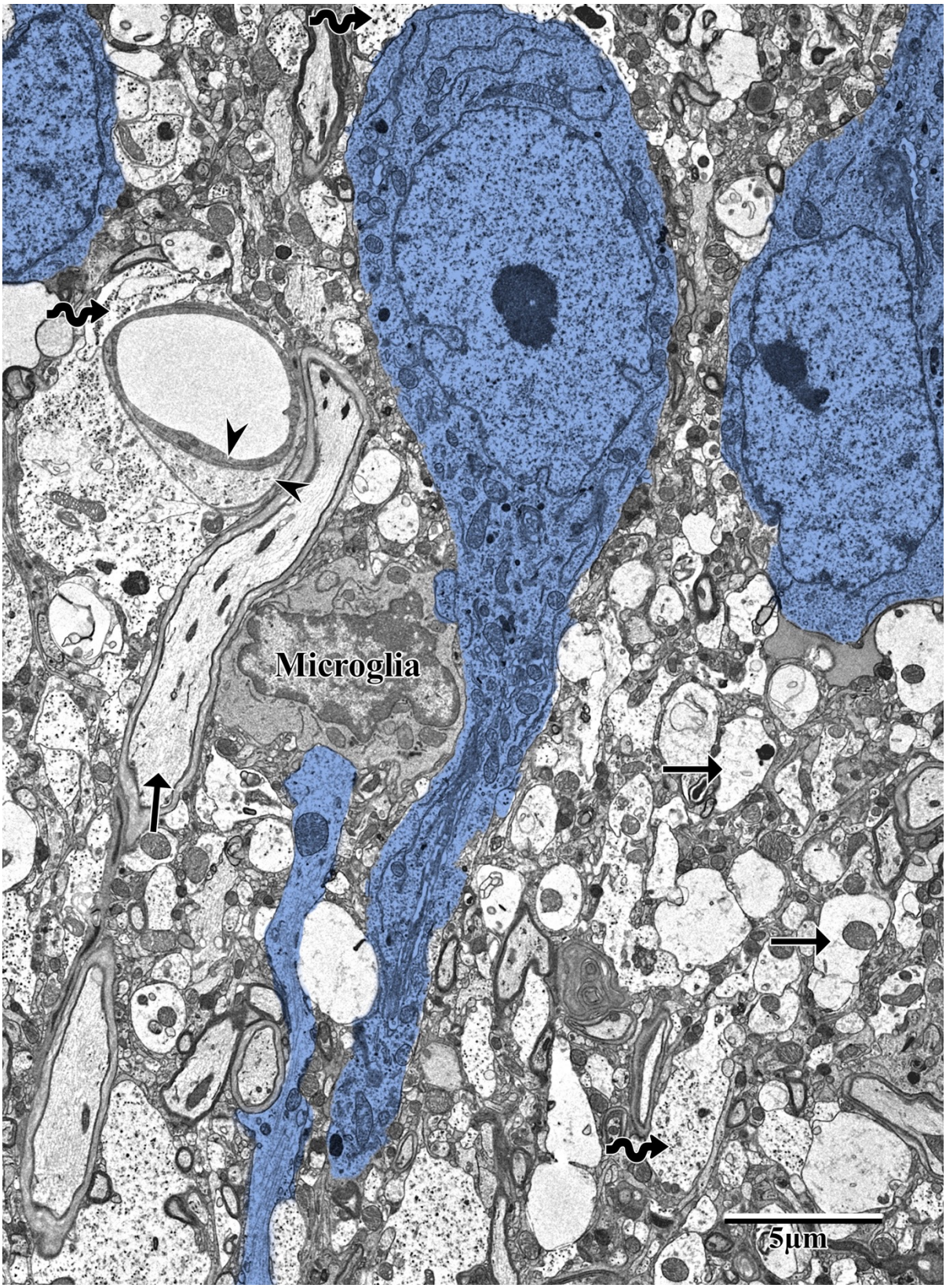

Figure 16. Pyramidal neurons within the proximal PI.
Pyramidal neurons (blue) located within layer 5 of the SSC show cellular processes (arrows) with organelle and cytoskeletal structures present but to a lesser extent compared to the distal PI. Astrocytes (wavy arrow) exhibit swollen morphology, with larger concentrations of glycogen granules compared to distal PI. Swelling of structures surrounding the capillary (arrowhead) suggests disruption of the BBB and its integrity. Occasional microglia were seen in the vicinity of neurons and capillaries.

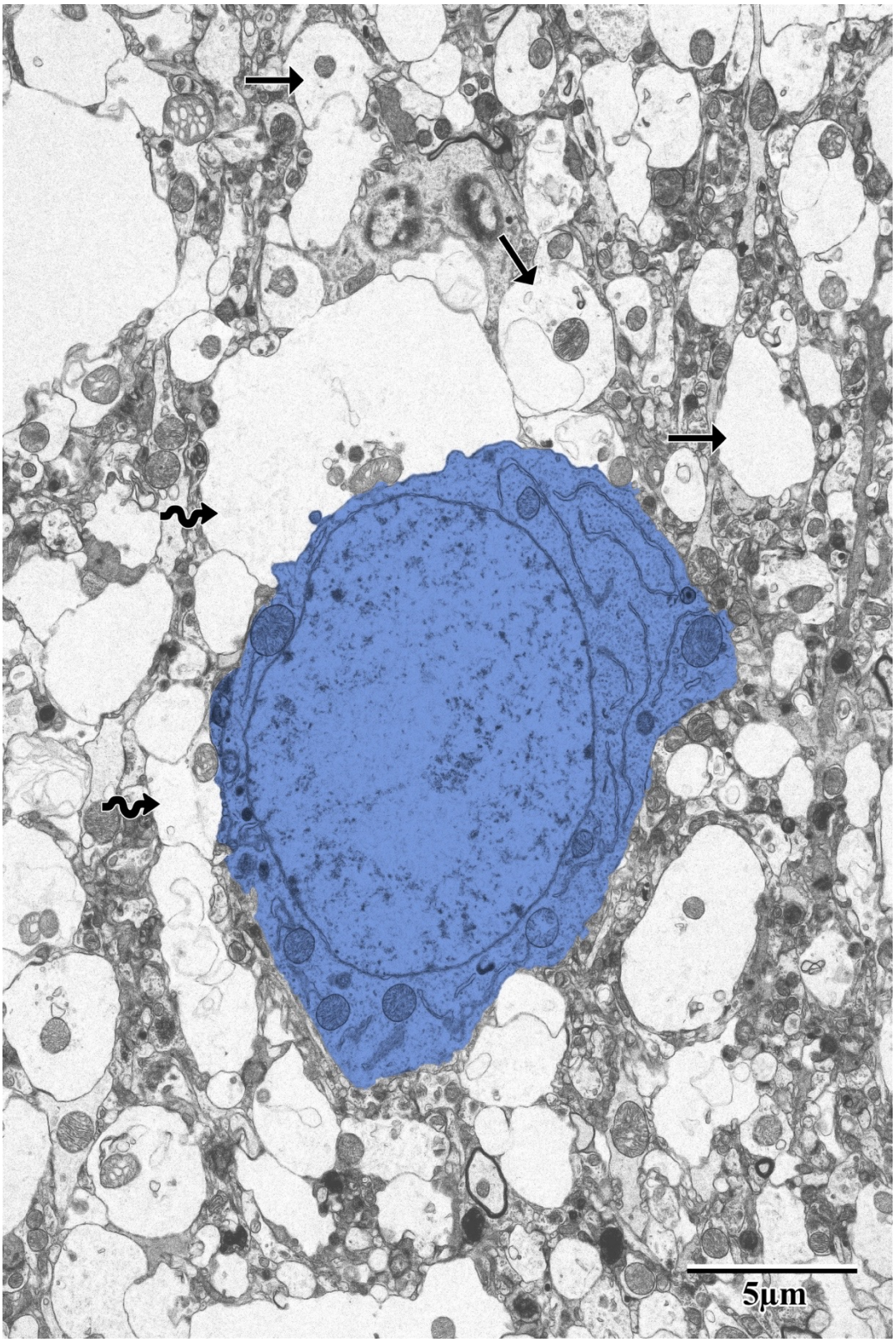

Figure 17: Pyramidal neuron located within the infarct zone.
Pyramidal neuron (blue) located in layer 3 of the SSC. Presence of barren dendritic processes (arrow) devoid of organelles and cytoskeletal structures was noted. Astrocytes (wavy arrow) were difficult to identify with no signs of glycogen granules.

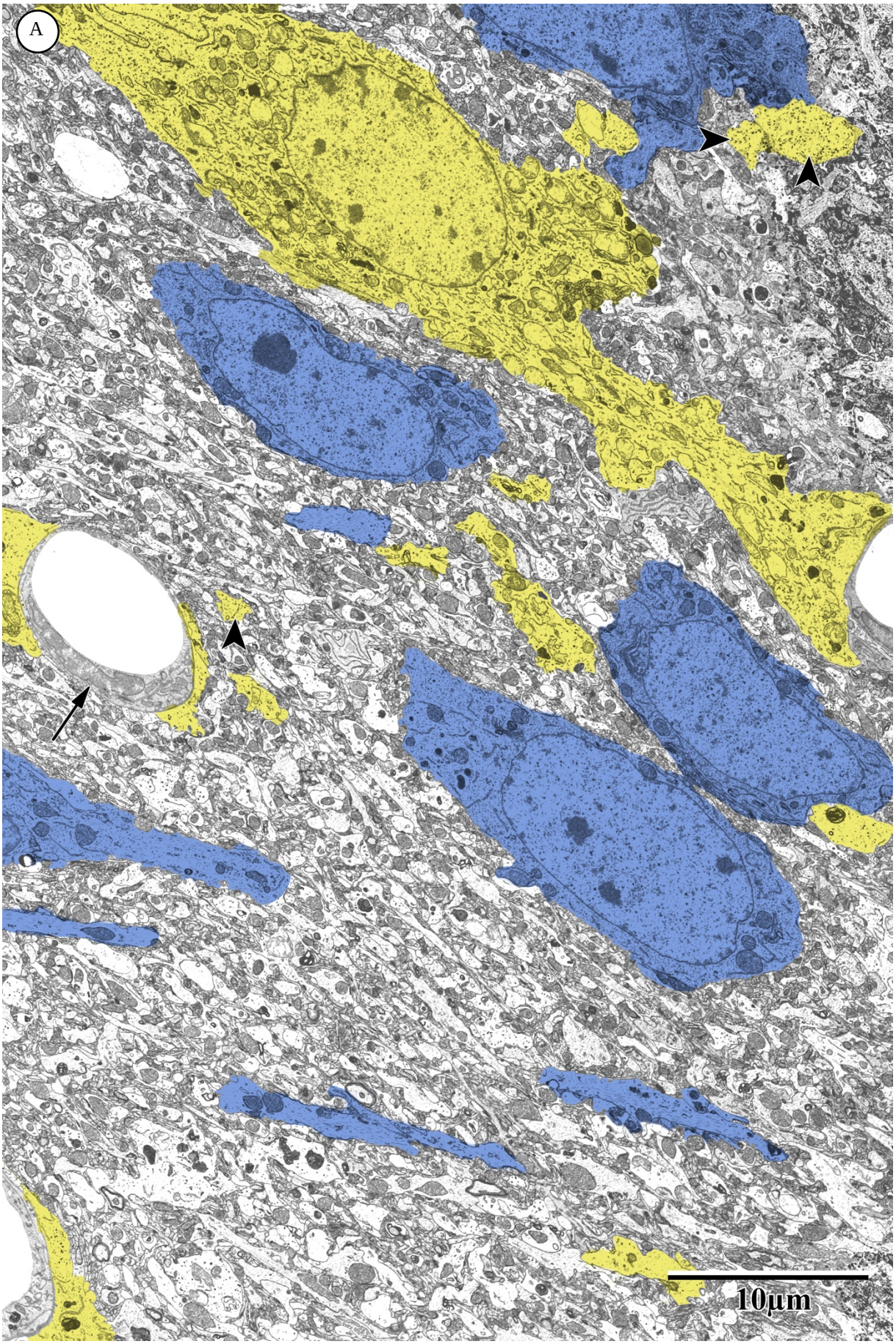
A
10µm

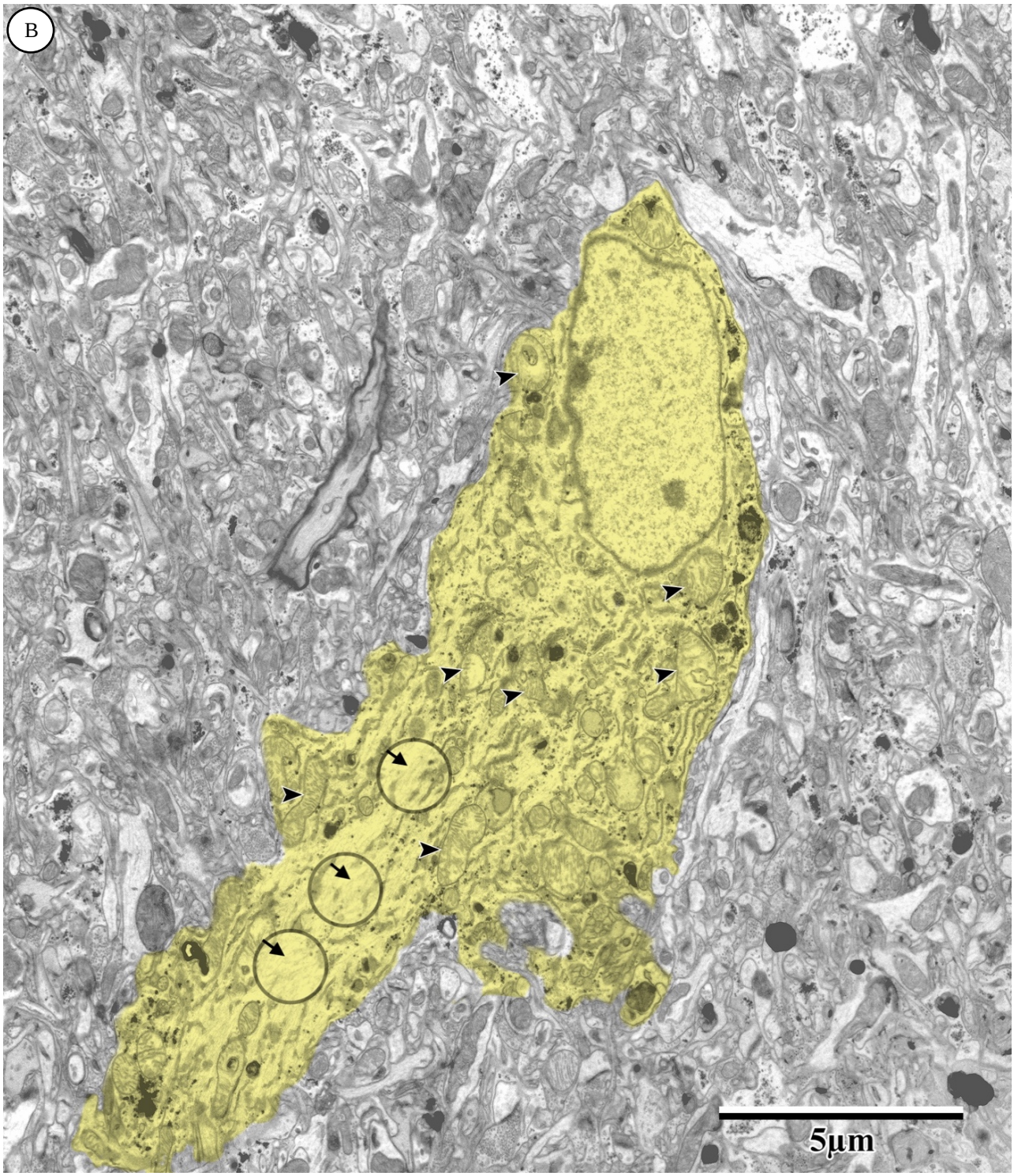

Figure 18. Pseudocoloured astrocytes within layer 3 of the PI.
(A) shows typical distribution of astrocytic processes (yellow) and cellular morphology within close vicinty of pyramidal neurons (blue). High concentrations of glycosidic granules (arrowheads) are present in astorcytic processes. Signs of inflammation within capillary structures (arrow) can also be seen. (B) shows the morphology of a single astrocyte, with a clear view of the internal cellular structures. Swollen mitochondria (arrowheads) have been indicated throughout the astrocyte. Highly magnified regions of the astrocytic cytoplasm (circles) allow close observation of cytoskeletal structures (arrows). Images captured at 2500x (A) and 5000x (B) magnification of astrocytic structures located within the PI.

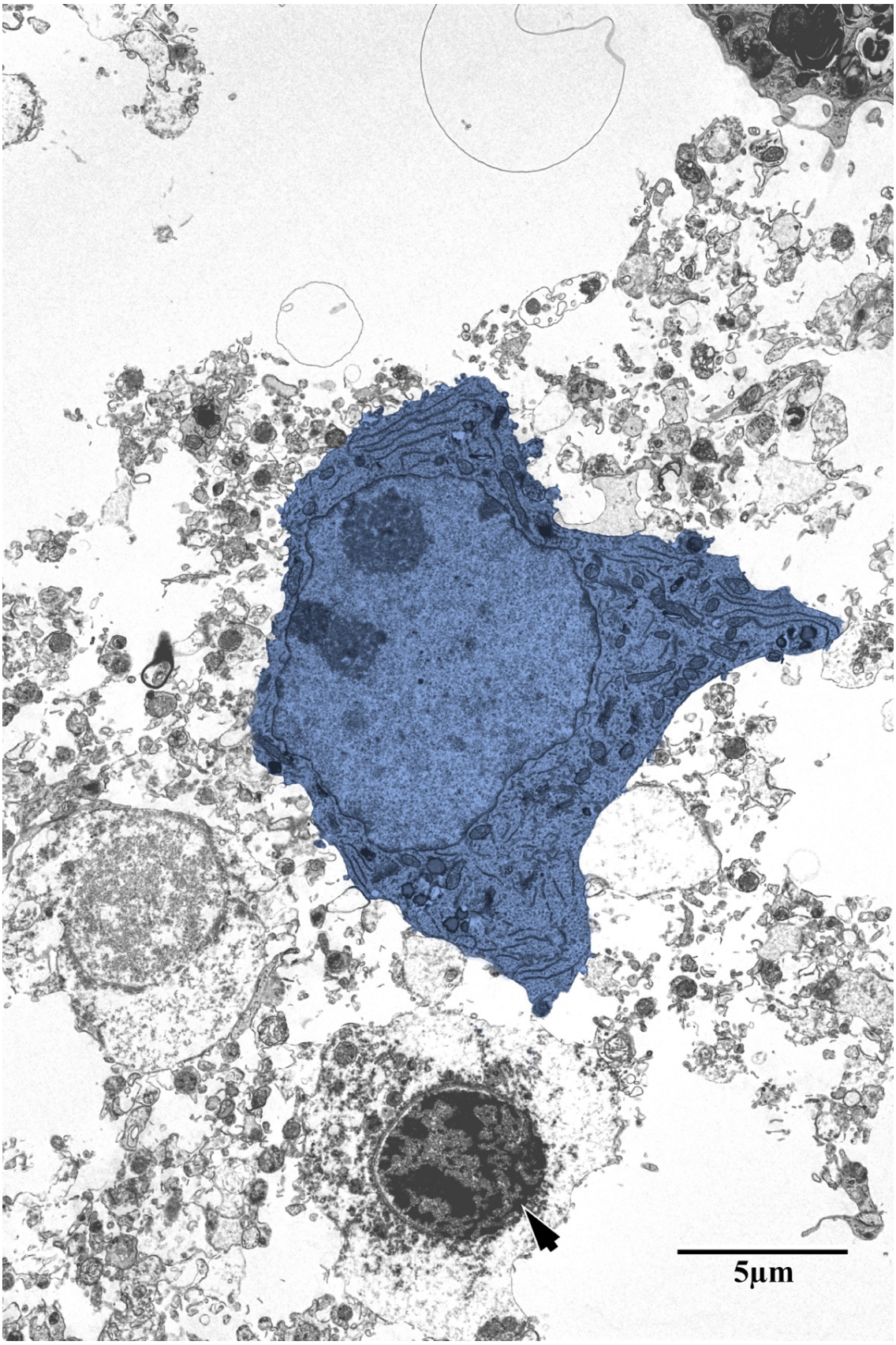

Figure 19. Low magnification EM of neuron and pyknotic nucleus of glial cell in the necrotic core.

A degenerating neuron (blue) and glial cell (arrow) are seen surrounded by degenerating neuropil tissue. No identifiable synapses were seen within this region.

3.3 Qualitative analysis: embossing technique

Special attention was given to a computational manipulation technique in which subcellular structures where to be found more pronounced and their structures more discernable. Based on observation, and with the appropriate filters (Adobe Photoshop), images were found to show much more detailed topography, allowing for structures such microtubules, microfilaments, mitochondria, RER and postsynaptic density to be more clearly visualized compared to the original image (see Appendix B).

3.4 Quantitative analysis: synaptic density lower in the PI

The number of synapses, identified using the synaptic criteria outlined above, were quantified and compared across PI and contralateral hemispheres (see figures 22 and 23). Within PI images examined, there was an average of 7 synapses per test field, while in control tissue, there were ~18 synapses (see table 2). A total of over 600 synapses were identified and incorporated in synaptic density calculations and analysis.

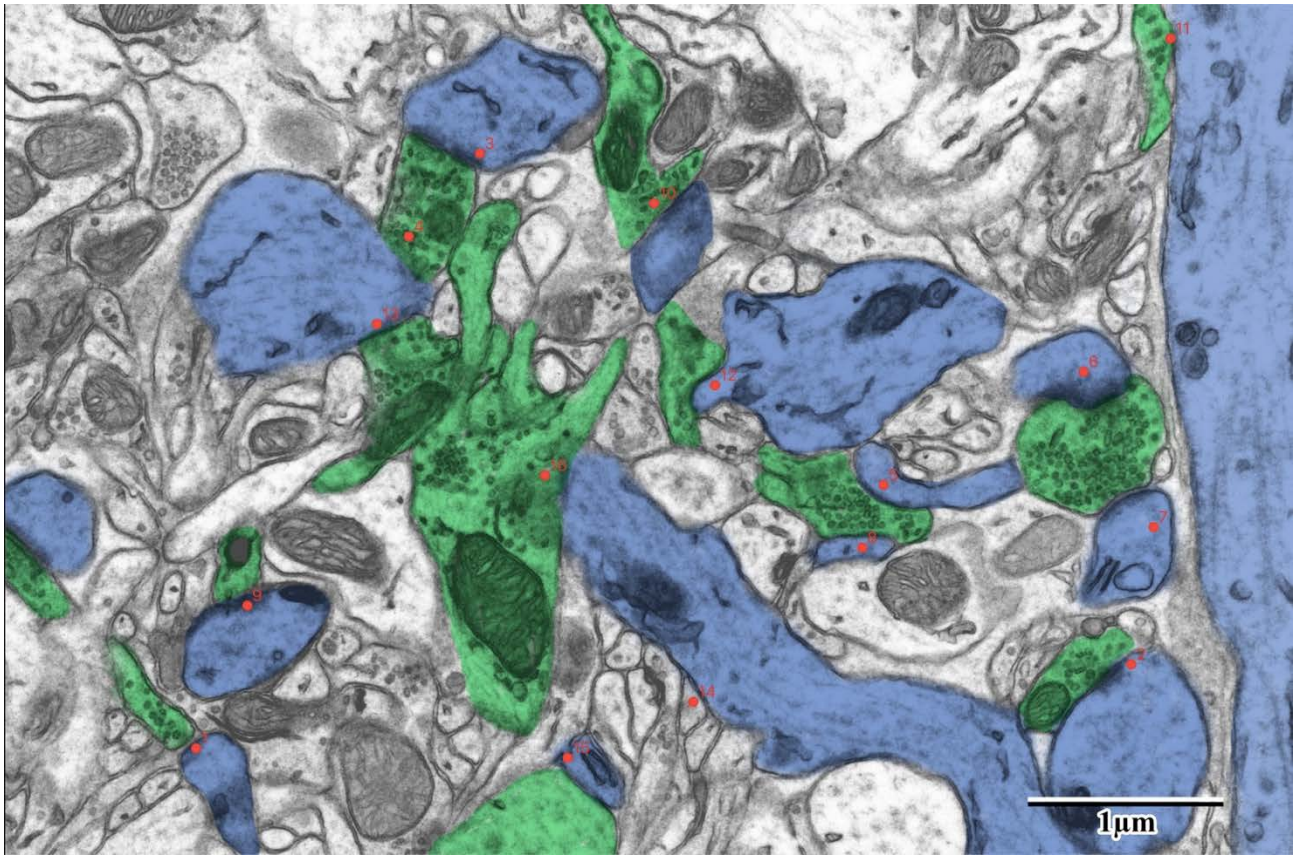

Figure 20. Synapse count within control tissue of adult mouse SSC.
Synapses were identified and counted. Synapses with synaptic clefts touching the bottom or the left side of the image were not counted. In image above, 16 synapses were counted, all of which were excitatory synapses. Image taken at 30,000x magnification.

Following statistical analysis, significantly higher density of synapses was found in control tissue compared to the PI. Two samples t-test (paired sample) was conducted to compare each animal's control hemisphere to the that of the PI. All mice showed significantly lower synaptic count per test field in the PI (6.58 µm by 4.39 µm; see Appendix C for the data for each the mice). Comparison of overall means (mean of contralateral and mean of PI) indicated a significantly larger synaptic count in the control hemisphere compared to the ischemic hemisphere ($p<0.0001$, DF=4; see figure 23 and table 2). One-way ANOVA analysis found that synaptic count was not significantly different across contralateral hemispheres of the mice (Mean=18.520 ±2.365, DF= 20, F=1.147, p=0.364). Conversely, synaptic count was found to be significantly different across ischemic hemispheres (mean=10.040 ±1.594, F=4.646, p=0.008). Post-hoc analysis confirmed ANOVA findings.

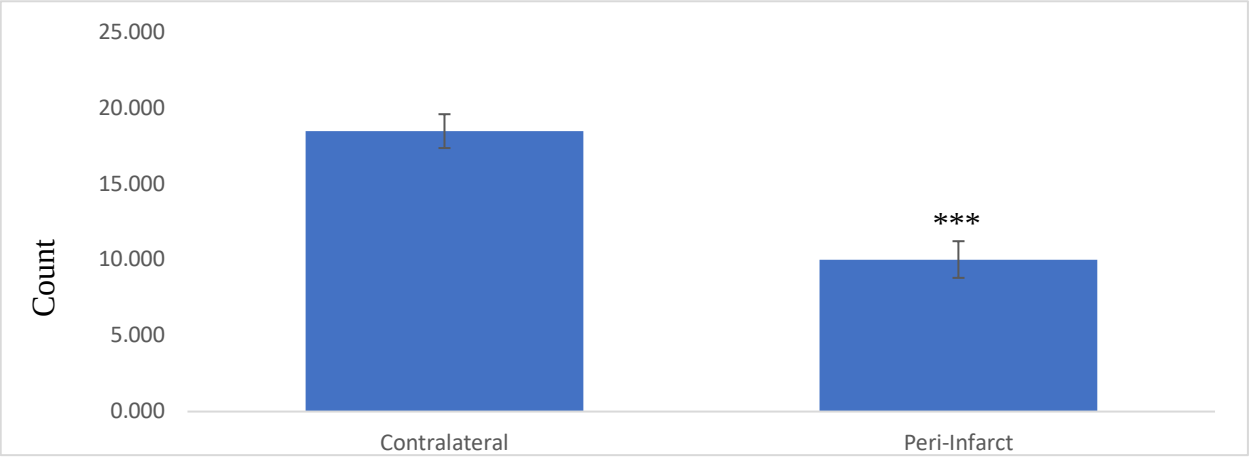

Figure 21: Cumulative mean comparison of synaptic density per test field.
Data from each animal's contralateral and the PI were collected and used to calculate the cumulative mean for each type of tissue. Significant differences ($p<0.0001$; denoted by ***) were found between the number of synapses per test field when comparing the experimental and the control group. An average of 18.520 synapses were found in contralateral images whereas only an average 7.200 synapses were found within PI images.

Table 2: Mean comparison of synaptic density per test field
The table includes a summary of the different means compared and the standard deviation that exists between the two groups. Relatively small standard deviations were present in both contralteral and PI images analyzed.

Variable	Number of Mice	Minimum	Maximum	Mean	Std. deviation
Contralateral	5	17.000	19.800	18.520	1.119
PI	5	5.000	8.000	7.200	1.304

3.5 Quantitative analysis: astrocytes inflammation in the PI

The area occupied by astrocytes and their processes was calculated following identification (using the criteria for astrocytic identification described above), tracing, and thresholding of these structures. Acquired areas were quantified and compared across PI and contralateral hemispheres (see figures 22 and 23). Within PI samples, astrocytes occupied an average of 6.5 ±0.97 μm^2, while in control tissue they occupied 2.8 ±0.54 μm^2. A total of 50 test fields were used to quantify and compare astrocytic area.

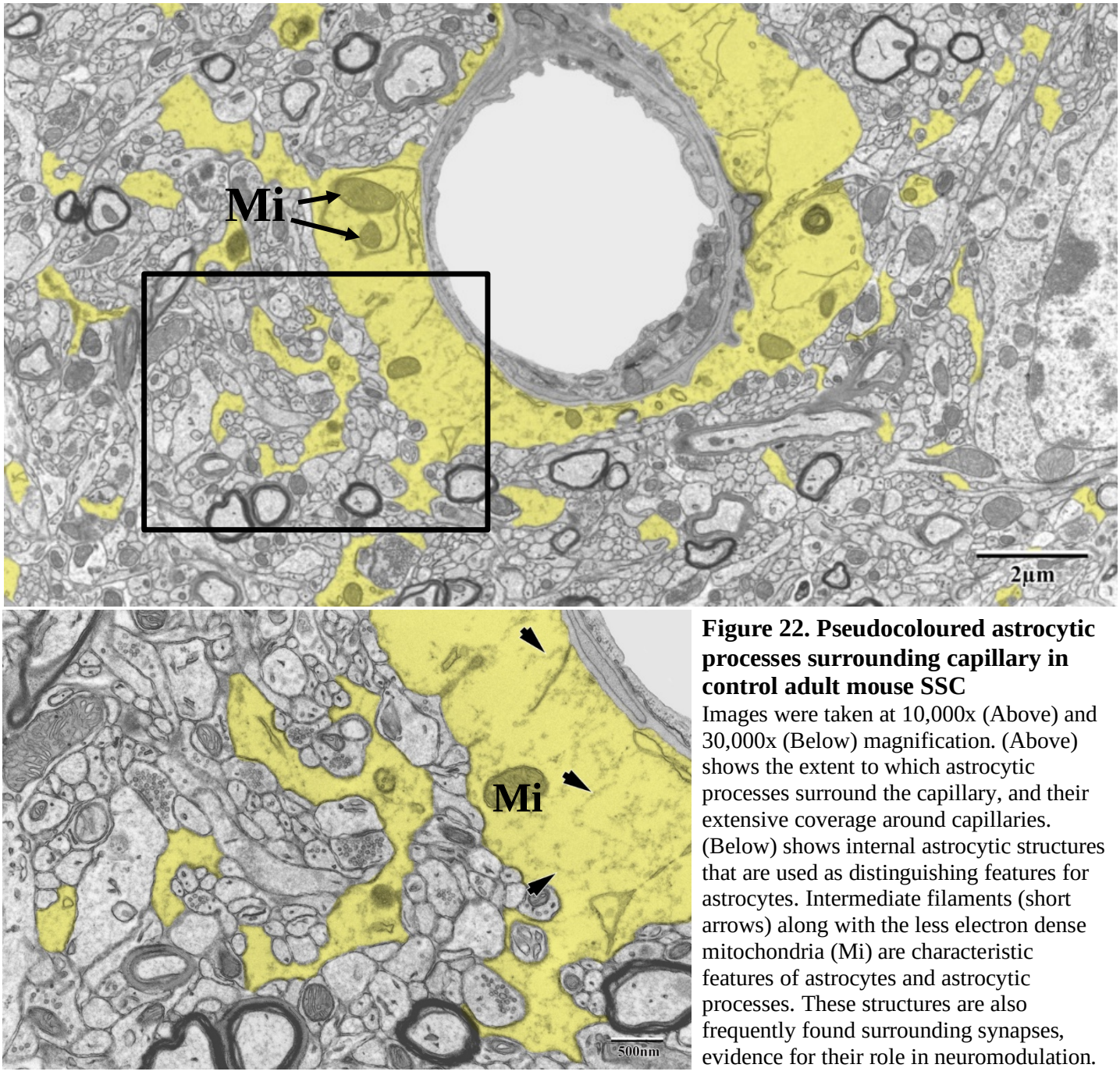

Figure 22. Pseudocoloured astrocytic processes surrounding capillary in control adult mouse SSC
Images were taken at 10,000x (Above) and 30,000x (Below) magnification. (Above) shows the extent to which astrocytic processes surround the capillary, and their extensive coverage around capillaries. (Below) shows internal astrocytic structures that are used as distinguishing features for astrocytes. Intermediate filaments (short arrows) along with the less electron dense mitochondria (Mi) are characteristic features of astrocytes and astrocytic processes. These structures are also frequently found surrounding synapses, evidence for their role in neuromodulation.

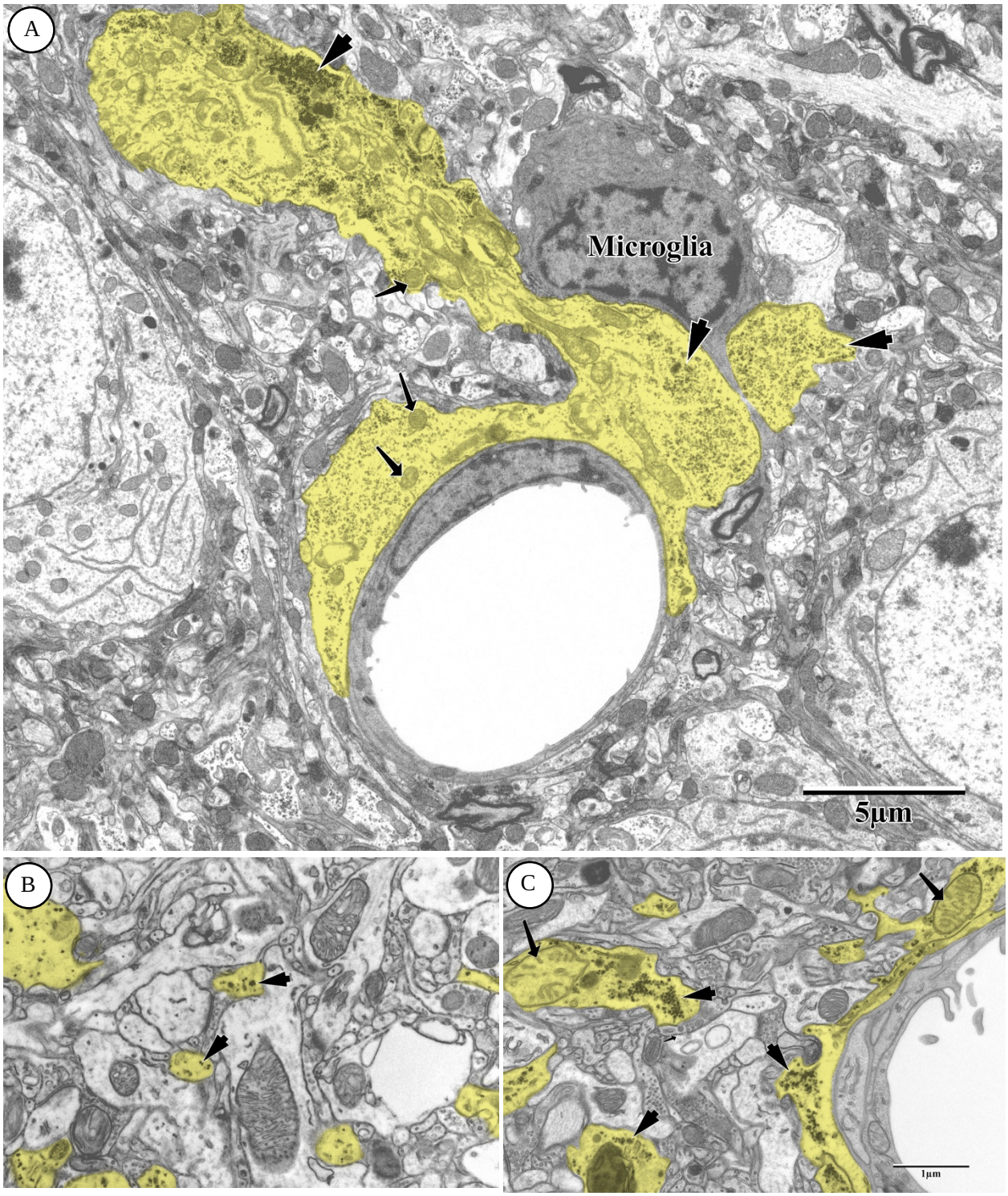

Figure 23: Tracing of astrocytic endfeet within the PI.
Image was captured at 5,000x magnification from layer 2/3 of the SSC. Lighter mitochondria (arrows) was one of the major identifying characteristic for astrocytic structures (yellow) as described above. Astrocytes within the PI also show a high concentration of glycogen granules (arrowheads) and swollen degenerating mitochondria. Additionally, the presence of microglia in close proximity to astrocytic processes suggests the presence of inflammation within these structures.(A) shows an example of astrocytic processes surrounding capillaries. (B) is an example of a PI test field used for quantification of astrocytic area. (C) displays lighter mitochondria (long arrows) and glycogen granules (short arrows) in astrocytic processes at higher magnification than to (A).

Tracing of astrocytic processes per test field in the contralateral and ipsilateral hemisphere of each mouse indicated that astrocytes occupied a larger area in PI versus contralateral tissue. This difference was found to be significant in all of the mice. Comparison of overall means corroborated the relationship established in comparing PI and control tissue from each of the mice (p=0.0004, DF=4; see table 3 and Appendix C). Within-condition comparison of means yielded no significant difference between contralateral hemispheres across different mice (mean=2.809 ±0.974, DF=20, F=1.756, p=0.147, R^2=0.260). Likewise, no significant difference was found in the astrocytic areas within PI across different mice (mean=6.503 ±1.994, DF=20, F=1.217, p=0.335, R^2=0.196).

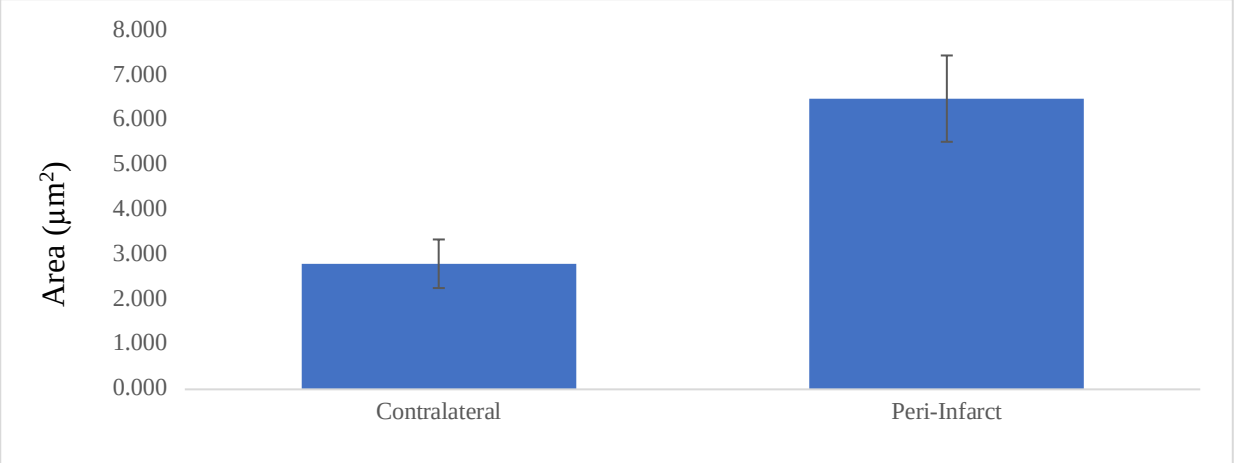

Figure 24: Mean comparison of astrocytic area per test field (6.58 µm x 4.39 µm).
Data from each animal's contralateral and the PI were collected and used to calculate the cumulative mean for each type of tissue. Significant differences (p=0.0004; denoted by **) were found between the astrocytic area per test field when comparing the experimental and the control group. Astrocytic area was found to be a mean of 2.809 μm^2 within the control whereas astrocytes occupied an area an average of 6.503 μm^2 within the PI.

Table 3: Mean comparison of astrocytic area per test field
The table includes a summary of the different means compared and the standard deviation that exists within the two groups. Relatively small standard deviations were present in both contralateral and PI images analyzed.

Variable	Number of mice	Minimum	Maximum	Mean	Std. deviation
Contralateral	5	2.081	3.426	2.809	0.544
PI	5	5.699	7.692	6.503	0.966

3.6 Quantitative analysis: postsynaptic density area in the PI

The area occupied by postsynaptic densities at identified synapses was calculated following identification (using the criteria for postsynaptic density identification described above), tracing, and thresholding of these structures. Acquired areas were quantified and compared across PI and contralateral hemispheres (see figures 26 and 27). Within PI samples, astrocytes occupied an average of 0.25 ±0.13 μm^2 while in control tissue they occupied 0.09 ±0.05 μm^2. A total of 50 test fields was used to quantify and compare postsynaptic density area.

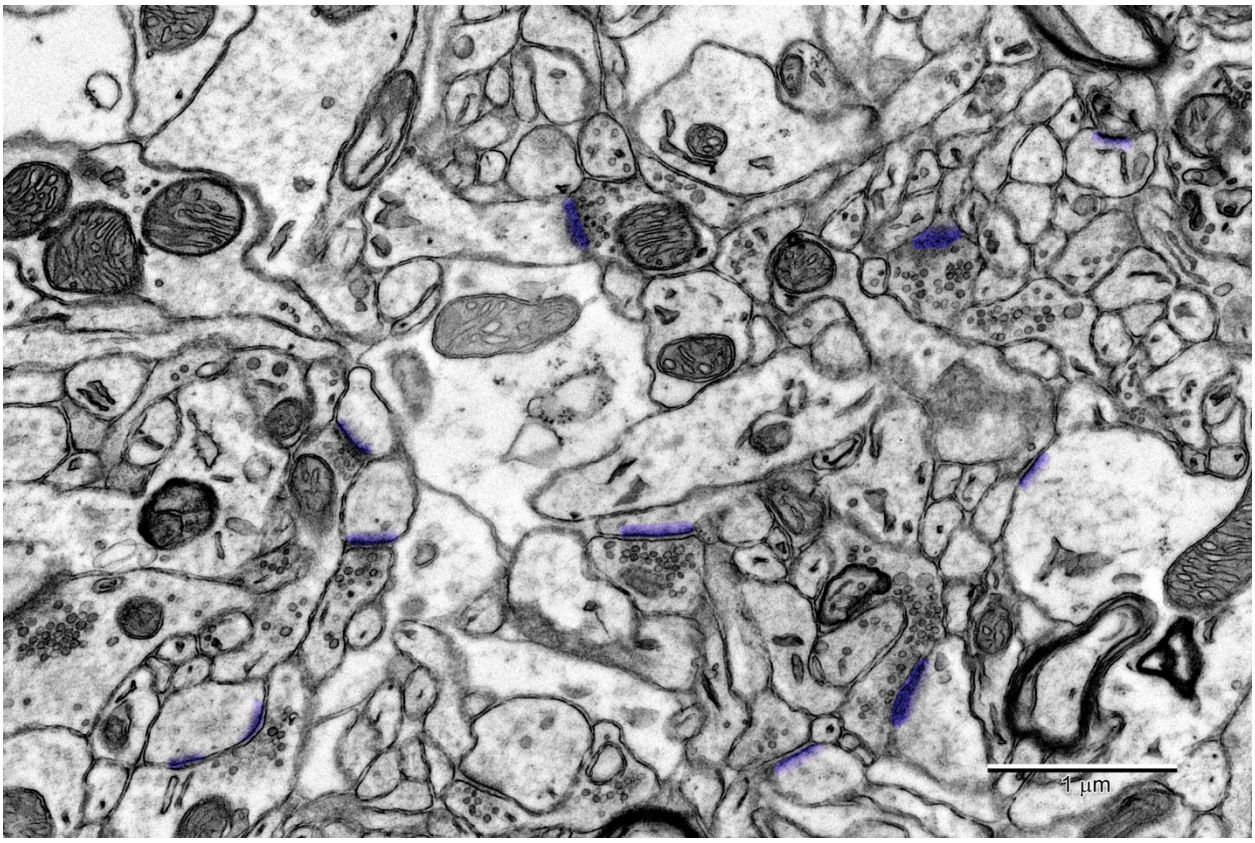

Figure 25. Pseudocoloured postsynaptic density area per test field (6.58 µm x 4.39 µm). Image was captured at 30,000x magnification from layer 2/3 of the SSC within the control hemisphere. Dense postsynaptic structures (violet) was one of the major identifying characteristic for astrocytic structures (yellow) as described above. Postsynaptic density was found to be significantly reduced within the PI. Based on observations, this made synapses within the PI akin to inhibitory synapses, despite the presence of round synaptic vesicles that are commonly found in excitatory synapses.

Tracing of postsynaptic densities per test field in the contralateral and ipsilateral hemisphere of each mouse indicated that postsynaptic densities occupied a smaller area in PI versus control tissue. This difference was found to be significant in four of the mice. Comparison of means corroborated these findings (p=0.014, DF=4; See Appendix C). Within-condition

comparison of means yielded a significant difference between contralateral hemispheres across different mice (mean=0.247 ±0.134 μm^2, DF=20, F=18.095, $p<0.0001$, $R^2=0.784$). Conversely, no significant difference was found in the postsynaptic density areas within the PI across different mice (mean=0.090 ±0.049 μm^2, DF=20, F=15.450, $p<0.0001$, $R^2=0.756$).

Table 4: Mean comparison of postsynaptic density area per test field

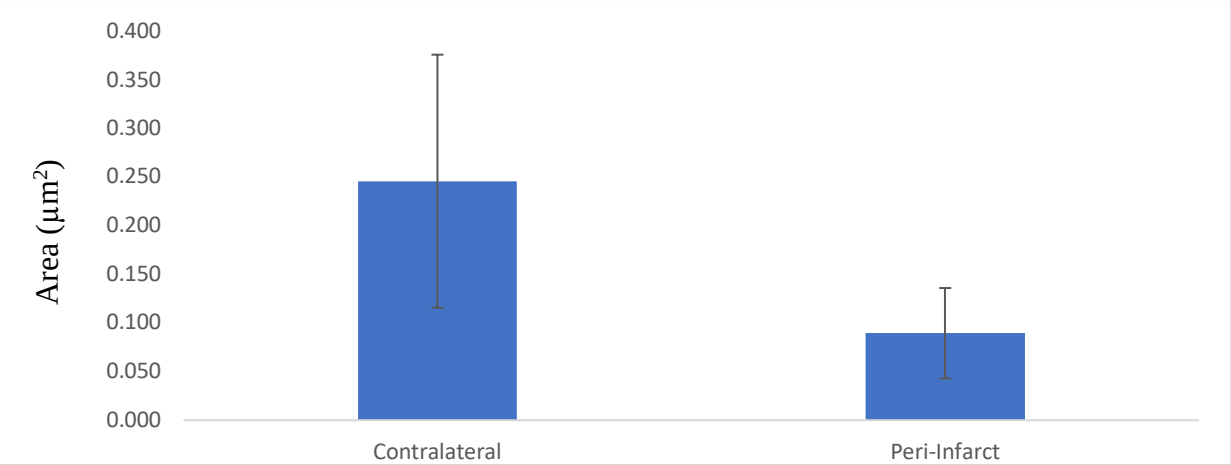

Figure 26: Mean comparison of postsynaptic density area per test field
Data from each animal's contralateral and the PI were collected and used to calculate the cumulative mean for each type of tissue. Significant differences ($p<0.05$; denoted by *) were found between the postsynaptic desnity area per testfield when comparing the experimental and control groups. Postsynaptic area was found to be a mean of 0.246 μm^2 within the control whereas postsynaptic densities occupied an average area of 0.090 μm^2 within the PI.
The table includes a summary of the different means compared and the standard deviation that exists within the two groups. Relatively large standard deviations were present in contralateral and PI images analyzed.

Variable	Observations	Minimum	Maximum	Mean	Std. deviation
Contralateral	5	0.178	0.479	0.246	0.130
PI	5	0.065	0.173	0.090	0.047

3.7 Quantitative analysis: variability in mitochondrial area

The area occupied by mitochondria was calculated following identification (using the criteria for mitochondria identification described above), tracing, and thresholding of these structures. Acquired areas were quantified and compared across PI and contralateral hemispheres (see figures 28 and 29). In four out of five mice, mitochondria were found to occupy substantially larger areas compared to the PI. Mitochondria occupied an average of 6.00 ±5.01

μm^2 in the PI, while in control tissue they occupied 1.56 ±0.16 μm^2. A total of 50 test fields were used to quantify and compare mitochondrial area.

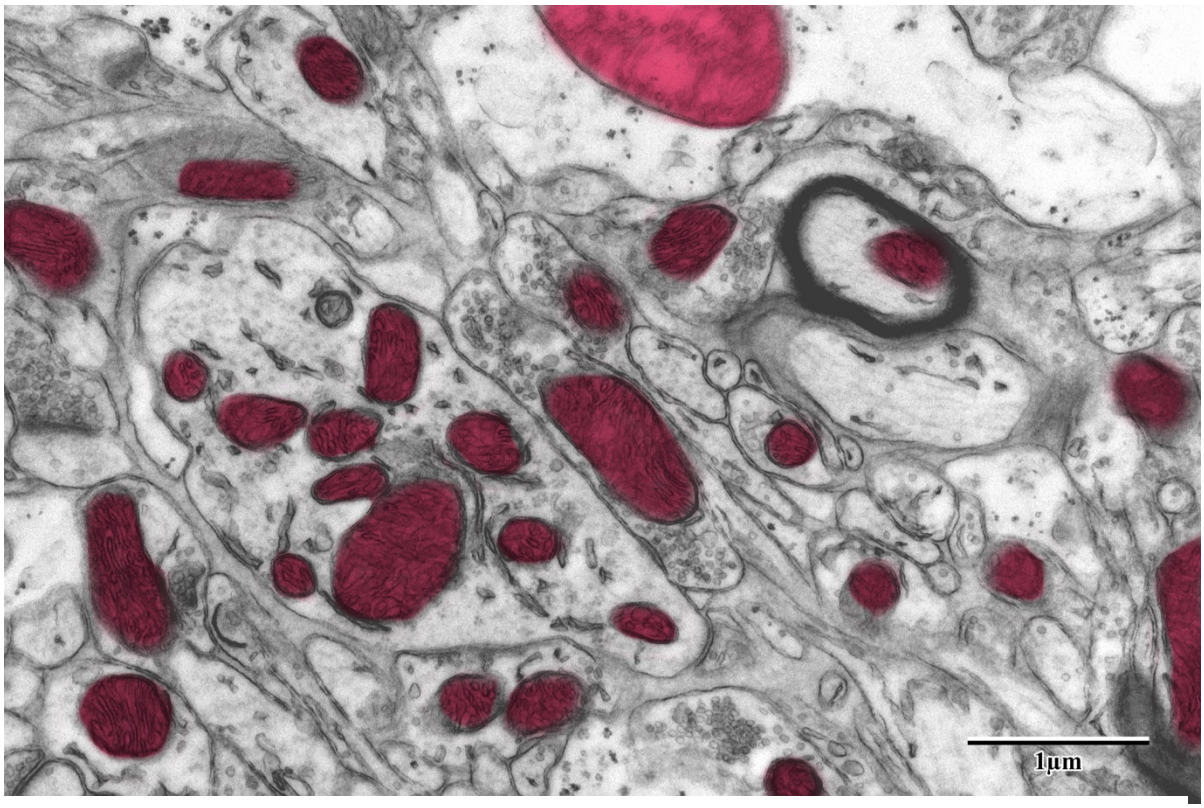

Figure 27: Pseudocoloured mitochondrial area per test field.
Image was captured at 30,000x magnification from layer 3 of the SSC within of the PI. Mitochondria (red) were found to be significantly larger within the PI for four of the five mice.

Tracing of mitochondria per test field in the contralateral and ipsilateral hemisphere of each mouse indicated to a limited extent, that mitochondria occupied a larger area in PI versus control tissue. This difference was found to be significant in four of the mice. Comparison of cumulative means, however, did not corroborate this finding ($p=0.088$, $DF=4$; see table 5 and Appendix C). Within-condition comparison of means yielded no significant difference between contralateral hemispheres across different mice (mean=1.557 ±0.446, $DF=20$, $F=0.628$, $p=0.648$, $R^2=0.112$). Conversely, a significant difference was found in the mitochondrial areas within the PI across different mice (mean=5.9 ±4.944, $DF=20$, $F=15.450$, $p<0.0001$, $R^2=0.874$).

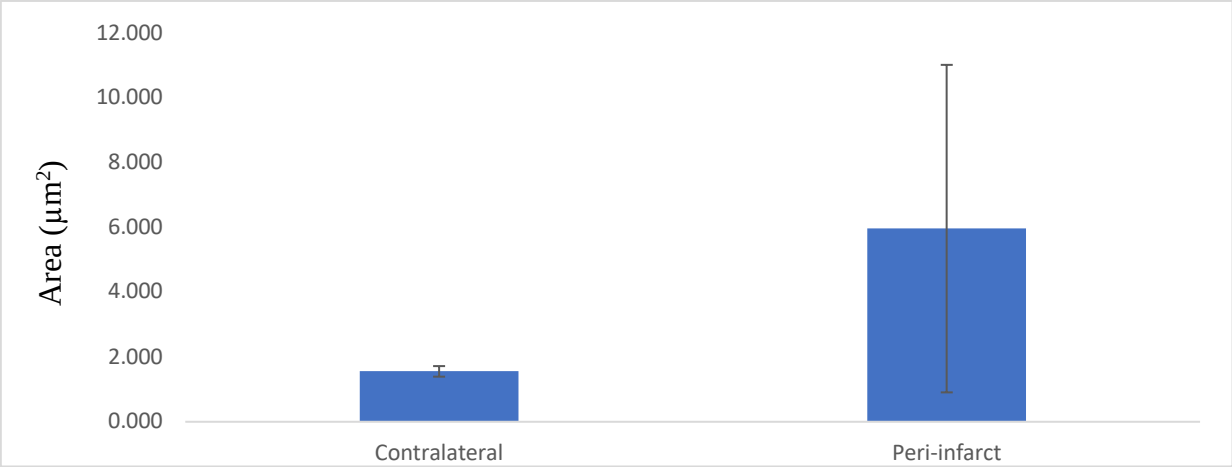

Figure 28: Mean comparison of mitochondria area per test field.
Data from each animal's contralateral and the PI were collected and used to calculate the cumulative mean for each type of tissue. No significant difference ($p>0.05$) was found between the mtochondrial area per testfield when comparing the experimental and control groups. This may be due to the large variability in mitochondrial area in the PI.

Table 5: Cumulative mean comparison of mitochondrial area per test field.
The table includes a summary of the different means compared and the standard deviation that exists within the two groups. Note that there is a large difference between means, and there is much variability within the PI.

Variable	Observations	Minimum	Maximum	Mean	Std. deviation
Contralateral	5	1.294	1.704	1.557	0.163
PI	5	1.693	14.495	5.967	5.064

3.8 Quantitative analysis: no difference in pre- and postsynaptic areas

The area occupied by pre- and postsynaptic structures was calculated following identification, tracing, and thresholding of these structures. Acquired areas were quantified and compared across the PI and contralateral hemispheres (see figures 30 and 31). No difference was found in the pre- or postsynaptic area. Presynaptic structures occupied an average area of 7.27 ±0.54 μm^2 in the PI, while in control tissue they occupied 7.51 ±1.16 μm^2. Postsynaptic structures occupied an average area of 12.12 ±2.21 μm^2 in the PI, while in control tissue they occupied 11.32 ±1.49 μm^2. A total of 50 test fields were used to quantify and compare presynaptic and postsynaptic structures and their associated areas.

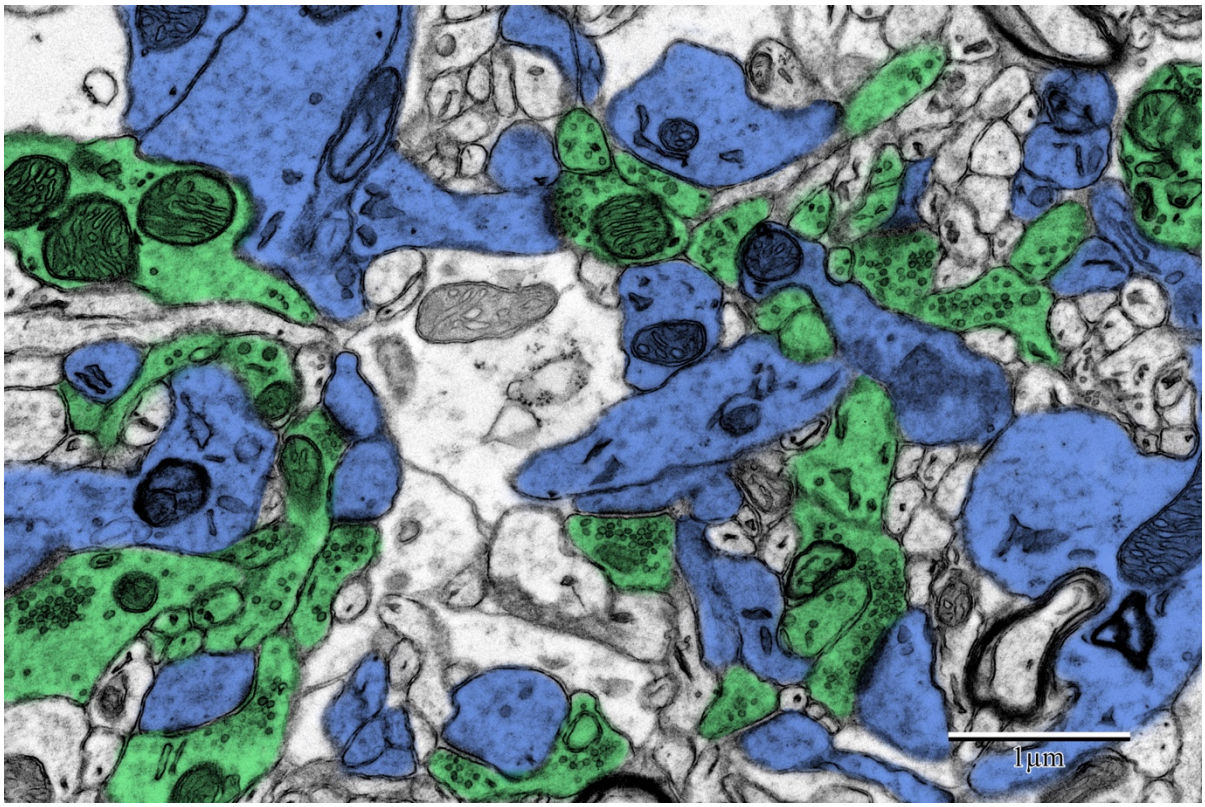

Figure 30. Presynaptic and postsynaptic area per test field within layer 3 adult PI SSC. No significant difference was found within and between mice when comparing presynaptic (green) and postsynaptic (blue) structures in the PI and control tissues. In this particular testfield, the area occupied by presynaptic structures was 7.3 µm^2 while postsynaptic structures occupied 10.8 µm^2.

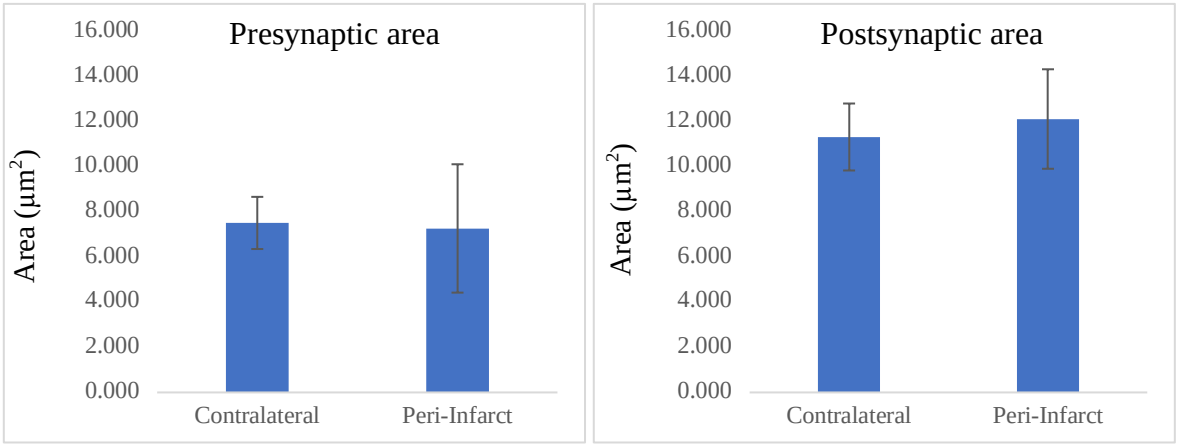

Figure 29. Mean comparison of presynaptic and postsynaptic area per test field. Data from each animal's contralateral and the PI were collected and used to calculate the cumulative mean for each type of tissue. No significant differences ($p>0.05$) were found between the presynaptic and postsynaptic area per test field when comparing experimental and control groups.

Tracing of presynaptic and postsynaptic regions per test field in the contralateral and ipsilateral hemisphere of each mouse showed no significant difference. Comparison of cumulative means of presynaptic areas did not show significance either (p=0.628, DF=4; see appendix for distribution). Similarly, comparison of cumulative means of postsynaptic areas also showed no significant difference (p=0.541, DF=4; see Appendix B for distribution).

Table 6: Mean comparison of presynaptic area per test field.
The table includes a summary of the different means compared and the standard deviation that exists within the two groups. Relatively small standard deviations were present in contralteral and PI images analyzed.

Variable	Observations	Minimum	Maximum	Mean	Std. deviation
Contralateral	5	6.095	8.878	7.514	1.157
PI	5	6.791	8.028	7.269	0.540

Table 7: Mean comparison of postsynaptic area per test field.
The table includes a summary of the different means compared and the standard deviation that exists within the two groups. Relatively small standard deviations were present in contralateral and PI images analyzed.

Variable	Observations	Minimum	Maximum	Mean	Std. deviation
Contralateral	5	9.751	13.140	11.323	1.485
PI	5	9.970	15.486	12.120	2.206

3.9 Quantitative analysis: no difference in vesicle density

Counting of synaptic vesicles enclosed by the presynaptic terminal showed no significant difference in any of the mice. Comparison of cumulative means of synaptic vesicle density within the control and the PI did not show significance either (p=0.186, DF=4; see table 8, figure 31, and Appendix B for the distribution).

Table 8 Synaptic vesicle density comparison between contralateral and the PI.
The table includes a summary of the different means compared and the standard deviation that exists within the two groups. Relatively large standard deviations were present in contralteral and PI images analyzed.

Variable	Number of Mice	Minimum	Maximum	Mean	Std. deviation
Contralateral	5	43.067	62.800	48.493	8.269
PI	5	34.533	48.533	41.467	5.925

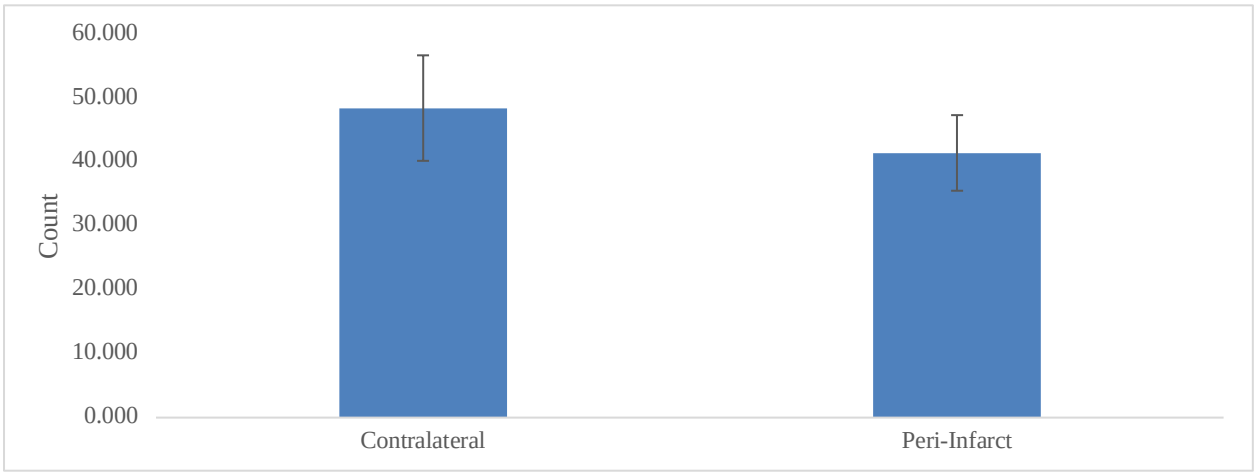

Figure 31. Cumulative mean comparison of synaptic vesicle count per test field.
Data from each animal's contralateral and the PI were collected and used to calculate the cumulative mean for each type of tissue. No significant difference ($p>0.05$) was found between the synaptic vesicle count per testfield when comparing experimental and control groups.

Discussion

With the use of light and transmission electron microscopy, imaging data were collected from ischemic and control hemispheres of five mice. Qualitative analyses were initially conducted to ascertain differential visual characteristics between control, the PI and necrotic tissues. Several differential characteristics were identified in both light and electron microscopy images. Quantitative analyses were then implemented onto the numerical data, consisting of structural density counts and comparison of areas occupied by different cellular structures. A total number of synapses were found to be significantly lower within the PI region when compared to unaffected brain tissue. The area occupied by astrocytes was found to be significantly higher in the PI region whereas post-synaptic densities were found to be significantly lower in the PI region compared to control. The mitochondrial area was found to be significantly different in intra-animal analyses (for four of the mice) but not significant in the inter-animal analysis. The area occupied by presynaptic terminals, postsynaptic terminals were not found to be significantly different, and vesicle content in presynaptic terminals showed no significant difference between the PI and control tissues.

4.1 Qualitative differences: light microscopy

Qualitative differences using light microscopy images captured for each animal revealed striking characteristics unique to each tissue region. The PI exhibited characteristically functioning blood vessels compared to the necrotic core (capillaries were hard to find in this region). However, these blood vessels showed aberrant shapes and displayed evidence of vacuolization within intact and control tissues. These observations were consistent with previous findings (Haley and Lawrence, 2017; Nahirney et al., 2016; Sims and Yew, 2017)

The dendritic and cellular analysis was limited to light microscopy images due to the limited resolution afforded by this microscopic technique. Despite this, these images showed signs of aberrant dendritic structures with characteristically blank interior areas devoid of any recognizable organelles. These aberrant neuronal structures were frequently found and at higher concentrations in areas more proximal to the infarct border. On the contrary, astrocytic expansion underwent a parabolic change. The distal PI showed slightly enlarged astrocytes. Astrocytes within the proximal infarct zone showed similar but amplified morphology, with increased inflammation. This ‘amplified’ morphology was then restored to levels similar to those of the

distal PI zone past the infarct border. Finally, at the necrotic core, very few discernable astrocytic processes could be identified.

4.2 Qualitative differences using transmission electron microscopy

The qualitative observations spotted in light microscopy images were confirmed by observations of the EMs. Cellular structures located within the PI zone showed progressively more aberrant morphology with increasing proximity to the infarct border. Inflammation within astrocytes increased with increasing proximity to the necrotic core, reaching their largest size within the proximal PI region. Past the infarct border, astrocytes assumed a more shrunken configuration. Likewise, the steady increase of glycogen granule concentration seen from the distal to the proximal PI was reversed, to the point that identifiable astrocytic structures showed seemingly no glycogen granules within the necrotic core. Blood vessels within the necrotic core were unrecognizable. Fully formed and shaped blood vessels were absent within these regions. In extremely rare cases, capillaries were spotted with fully disintegrated tight junctions, or even with exploding endothelial cell nuclei.

4.3 Synaptic density and astrocytic area

Both synaptic density and astrocytic area were found to be significantly different when comparing PI imaging data with control data. Intra and inter-animal analysis corroborated these findings. Synaptic density was found to be significantly lower within the analyzed the PI in all mice when compared to their contralateral hemisphere and when their results were incorporated into cumulative analysis across all mice. Additional analyses were conducted in order to investigate the variability across mice within stroke and non-stroke hemispheres. ANOVA and post-hoc testing revealed no significant difference ($p=0.364$) between the different mice and their synaptic density within control samples. Interestingly, however, both ANOVA and post-hoc testing revealed significant variability in synaptic density of the PI across all mice. This variability in synaptic density within the PI may be a result of the variable nature of ischemia, especially thrombosis, in their ability and extent to which they disturb neuronal tissue and their extracellular environment. Additionally, the degree of disruption within nearby capillaries, the associated BBB structures, and the ionic contents of the extracellular environment could also influence synaptic density.

The decrease in synaptic density observed may also be explained by inflammation of astrocytes. A significant difference in astrocytic area was found for all mice in both intra and

inter-animal analyses. The astrocytic area was shown to be significantly larger in the PI. These findings corroborate previous research findings (Nahirney et al., 2016; Sims and Yew, 2017; Thrane et al., 2014). A potential mechanism for this inflammation may be a result of fluid uptake, driven by the drastic increase in glycogen granules within astrocytes. Free glycogen granules would, in turn, result in an imbalance in osmolarity within the cytoplasm of astrocytes, resulting in the diffusion of water into the cell.

Works by previous researchers have indicated that this widespread presence of glycogen granules alludes to the functionality of astrocytes as energy storage systems for neuronal tissues (Hossain et al., 2014; Kajihara et al., 2001). This metabolic functionality of astrocytes makes intuitive sense due to the proximity of astrocytic endfeet to blood vessels, and their role in regulation and transportation of materials across the BBB. The widespread accumulation of glycogen granules within astrocytes may be due to the energy deficient state of ischemia. It would, therefore, be logical to find these energy storage systems participating in glycogen polymerization to prepare for future incidents of low nutrient states.

4.4 Altered subcellular structures: postsynaptic density and mitochondrial area

Research within the past decade has made critical contributions in providing possible mechanisms for synaptic loss and cortical remapping within the PI (Brown et al., 2009; Grefkes and Ward, 2014; Kim et al., 2017; Nahirney et al., 2016). Most of such studies, focusing on cortical stroke, have utilized light microscopy methodology such as confocal/two-photon microscopy. These microscopic methods have much versatility in their applications, as they can be applied within *in vivo* paradigms, where model organisms are allowed to recover, and their recovery following stroke can be captured. This research paradigm allows further imaging applications to be implemented such as time-lapse imaging, which has been utilized to view dendritic growth as a function of time (Brown et al., 2009; Rochefort and Konnerth, 2012). Despite its temporal strengths, however, this methodology lacks the spatial resolution to ascertain the morphological changes that occur within and between neurons. The resolving power provided by light microscopy is insufficient in its ability to convey relatively smaller subcellular structures. As such, there has been scant research findings regarding the cellular structures of the PI (e.g. extracellular processes, intracellular organelles, and protein complexes).

Through examination and quantification of internal neuronal structures, we found significant differences in postsynaptic density area and mitochondrial area. Postsynaptic density,

earlier described as a cluster of dense proteins occupying areas within the vicinity of the postsynaptic membrane of excitatory neurons (Boeckers, 2006), were seen to be downregulated in the PI. The intra-animal analysis yielded a significant difference in postsynaptic density area for four of the five mice. Additionally, we also found significant differences the inter-animal analysis. Within-condition analyses across all mice indicated a significant difference between postsynaptic density areas in control tissue; however, no significant difference was found when comparing data collected from all mice. Variable postsynaptic density is fathomable within control tissue. Different types of synapses (i.e. type I and type II) exhibit different amounts of postsynaptic density and each image might have a different distribution of synapses which may account for the variation seen in control tissue. However, the lack of variation seen in the PI may be suggestive of the mechanisms by which synaptic activity may be altered in this region. In fact, close inspection of previous research on the functionality of postsynaptic density proteins in allowing the binding of glutamate receptors onto the postsynaptic membrane indicates that perhaps the ability of the postsynaptic neuron to propagate fast excitatory potential may be altered (Brown et al., 2008; Lai et al., 2014)

In addition to changes in postsynaptic density, the area occupied by mitochondria was also found to have changed significantly in the PI. The qualitative examination of the PI mitochondria revealed swelling/bursting morphology not seen in the control hemisphere. The quantitative analysis yielded a significant increase in mitochondrial area for four of the mice. Conversely, no significant difference in mitochondrial area was found when overall means were compared. Although this outcome may seem to weaken the obtained results, further within-condition analysis (see Appendix C) found significant variability of mitochondrial area across different mice. Part of this variability is due to the disintegration of inflamed mitochondria within the PI. Degeneration of mitochondria also made it difficult to recognize structures that may have previously been mitochondria. In contrast to the PI, no significant difference was found in the area occupied by mitochondria within control tissue. Collectively, these analyses indicate that perhaps the lack of significance in the cumulative means may be due to the considerable variability exhibited by mitochondria located within the PI. It could also suggest that perhaps the degree to which mitochondrial area changes following stroke is different for different mice, and that a more stochastic model should be adopted in predicting mitochondrial size within the PI.

4.5 No significant difference in synapse area and vesicle content

No significant difference was found in comparing the area occupied by presynaptic and postsynaptic structures following analysis. No significant difference was found in intra- and inter-animal analyses, meaning that not only was there no difference in the area of these structures at a cumulative level, but individual mice also showed no difference in the areas occupied by these structures. Furthermore, no directional trends were spotted. Likewise, no significant difference was found in synaptic vesicle count located within the presynaptic terminals. High levels of variability were detected in both control and to a more considerable extent, the PI.

Increase in the relative sizes of presynaptic terminals and postsynaptic spines were seen in our observations of the PI and contralateral EMs. It is therefore possible that both presynaptic and postsynaptic processes undergo inflammation to the same degree; therefore, they also tend to occupy a similar total area in affected and not affected tissue. It is also highly likely that our experimental paradigm of calculating the area of various neuronal processes within a test field does not capture the change that is seen in these tissues. Perhaps a closer look should be taken on the number of individual pre- and postsynaptic structures rather than the total area occupied by such structures. In addition, no significant differences were found in synaptic vesicle count when comparing synapses within the PI and those of the contralateral hemisphere. The inability to find a significant difference in synaptic count is, in our opinion, largely due to the clustering of synaptic vesicles, and their aggregation within the active zones. This prevented us from attaining accurate counts of the number of synaptic vesicles within the terminals that were observed. We were also limited by the two-dimensional nature of EMs, in which all the vesicles within the presynaptic terminal could not possibly be counted from a single cross-section of a tissue. Perhaps a three-dimensional reconstruction of such structures should be completed to attain more accurate results.

4.6 Limitations

4.6.1 Definition of the synapse and synaptic structures

Although many researchers have previously examined the structural and morphological structures of synapses within the SSC (Brown et al., 2009; Seitz et al., 1998; Takatsuru et al., 2009; Winship and Murphy, 2009), almost no previous inquiries have been made on the synaptic morphology of infarct region and the PI. The qualitative analysis found visible differences in

synaptic organization and neuronal configuration. A large number of unrecognizable structures was seen in neuronal processes. These ambiguous synaptic structures made it difficult to ascertain the identity of the viewed structures. This inability to recognize such structures may be responsible for the large portion of the variability seen within our data.

4.6.2 Identification of inhibitory synapses

Special attention was given to identifying inhibitory synapses within the PI based on previous electron microscopy studies (High et al., 2015). Based on our data, there may be a generalized loss of postsynaptic density seen within the synapses of the PI. If this is indeed the case, then synapses that may have been identified as inhibitory, may, in fact, be excitatory. Based on qualitative observations, inhibitory synapses were much more common in the PI compared to control tissue.

4.6.3 Test field magnification

Deciding on the appropriate magnification that will yield the most representative dataset for analysis often involves analytical and mathematical considerations. The decision to include a test field of 6.58 by 4.39 μm, acquired at 30,000x magnification, was decided upon following stereological grid-point counting method (Wong et al., 1996; see Appendix D). This method was chosen due to its unbiased and random nature and since it has been a method of cell counting and analysis used in previous research (Franzén et al., 2005; St. Pierre et al., 2016). 1 μm^2 grid (8 by 8 squares) was overlaid onto a low magnification EM. This size of the grid was chosen to allow for a maximum of 64 intersections, therefore, allowing for up to 64 synapses to be counted in the lower magnification images. Synapses with synaptic clefts that were intersected by the grid were counted, and this number was then compared to higher magnification images located within the same field of view. Each grid intersection is analyzed independently and solely based on the criteria of intersection described above. 30,000x magnified images were found to be representative, and the number of synapses within this test-field was found to equal the number of synapses counted in the lower magnified EM. Therefore, due to the resolution, the detail afforded by analyzing higher magnification images, and the stereological analysis, a test field of 6.58 by 4.39 μm was deemed appropriate to be used for quantitative measures for this study. The most significant issue in analyzing images collected for this study was that PI EMs seemed to require a larger test field due to the swelling of astrocytes and subcellular processes (i.e. mitochondria), while control tissue showed the opposite effect, where the designated test field contained too many structures.

It is worth noting that the size of the test field plays a vital role in the results and the conclusions made within imaging studies (Von Bartheld, 2002). The size of the test field can have an immense effect on the outcome of imaging experiments and may skew the data. It is, therefore, a limitation of this study, due to time constraints, that pilot studies were not conducted for in-depth stereological analysis to take place.

4.7 Future Directions

If a similar experimental paradigm were to be pursued, it would be beneficial to incorporate data from more animals and to incorporate tissues from animals at various stages of recovery following ischemia. These improvements would allow for more conclusive information to be attained regarding synaptic morphology and the mechanism underlying recovery (or deterioration) of synaptic structures. Additionally, a timeline of changes in neuronal morphology could be constructed. Lastly, this methodology would allow more direct information to be gathered regarding the underlying mechanisms of cortical remapping and/or degeneration of the PI in recovering animals.

Despite the changes discussed above to improve the methodology adopted within this study, there is also a need for a new experimental paradigm to be adopted (i.e. imaging method) which would allow high spatial resolution while observing living tissues. Should a method similar to confocal imaging be adopted (potentially one with higher resolution and magnification capabilities), it would be beneficial to image different layers of tissue which would allow for three-dimensional reconstruction of synapses in a feasible time frame. This methodology would provide the most conclusive evidence by allowing time-lapse imaging data to be collected, and therefore a temporal timeline to be constructed. A potentially viable imaging technique may have already been developed that would fit these requirements: *in vivo* scanning electron microscopy (Lim et al., 2006).

Conclusion

The findings of this study suggest that there are qualitative and quantitative differences in neuronal and synaptic morphology between PI and control tissues. Qualitatively, light micrographs of the PI showed viable but injured morphology of cells with visible lack of perfusion compared to the intact zone and control tissue. The necrotic core showed no functioning capillaries and exhibited a lack of perfusion. EMs of distal PI contained swollen astrocytes with glycogen granules, disintegrated tight junction, and swollen mitochondria, compared to control tissue. Proximal PI shows similar but more pronounced morphology compared to the distal, with highly swollen astrocytes containing large aggregates of glycogen granules and inflammation within BBB structures. The incidence of unidentifiable cellular processes was much higher within the proximal infarct zone compared to that of the distal. Lastly, the infarct zone contained rarely any viable and identifiable cellular structures and virtually no capillaries. Collapsed pyknotic nuclei were also very common within this region. Quantitatively, we found that the PI contained lower synaptic density, astrocytic inflammation, swollen mitochondria, and a much lower postsynaptic density compared to control tissue.

References:

Abbott, L. F. (2008). Theoretical Neuroscience Rising. *Neuron* 60, 489–495. doi:10.1016/j.neuron.2008.10.019.

Abbott, N. J., Rönnbäck, L., and Hansson, E. (2006). Astrocyte-endothelial interactions at the blood-brain barrier. *Nat. Rev. Neurosci.* 7, 41–53. doi:10.1038/nrn1824.

Adrian, E. D. (1948). The organization of the nervous system. *Nurs. Times* 44, 206. doi:10.1007/978-1-4899-2919-8_1.

Arundine, M., and Tymianski, M. (2004). Molecular mechanisms of glutamate-dependent neurodegeneration in ischemia and traumatic brain injury. *Cell. Mol. Life Sci.* 61, 657–668. doi:10.1007/s00018-003-3319-x.

Auld, D. S., and Robitaille, R. (2003). Glial Cells and Neurotransmission. *Neuron* 40, 389–400. doi:10.1016/S0896-6273(03)00607-X.

Bacigaluppi, M., Comi, G., and Hermann, D. M. (2010). Animal models of ischemic stroke. Part two: modeling cerebral ischemia. *Open Neurol. J.* 4, 34–38. doi:10.2174/1874205X01004020034.

Ballabh, P., Braun, A., and Nedergaard, M. (2004). The blood-brain barrier: An overview: Structure, regulation, and clinical implications. *Neurobiol. Dis.* 16, 1–13. doi:10.1016/j.nbd.2003.12.016.

Banerjee, S., and Bhat, M. A. (2007). Neuron-Glial Interactions in Blood-Brain Barrier Formation. *Annu. Rev. Neurosci.* 30, 235–258. doi:10.1146/annurev.neuro.30.051606.094345.

Banerjee, S., and Bhat, M. A. (2008). Glial ensheathment of peripheral axons in Drosophila. *J. Neurosci. Res.* 86, 1189–1198. doi:10.1002/jnr.21574.

Banks, W. A., and Erickson, M. A. (2010). The blood-brain barrier and immune function and dysfunction. *Neurobiol. Dis.* 37, 26–32. doi:10.1016/j.nbd.2009.07.031.

Beard, D. J., Murtha, L. A., McLeod, D. D., and Spratt, N. J. (2016). Intracranial Pressure and Collateral Blood Flow. *Stroke* 47, 1695–1700. doi:10.1161/STROKEAHA.115.011147.

Beck, P. D., Pospichal, M. W., and Kaas, J. H. (1996). Topography, architecture, and connections of somatosensory cortex in opossums: Evidence for five somatosensory areas. *J. Comp. Neurol.* 366, 109–133. doi:10.1002/(SICI)1096-9861(19960226)366:1<109::AID-CNE8>3.0.CO;2-7.

Beique, J.-C., Lin, D.-T., Kang, M.-G., Aizawa, H., Takamiya, K., and Huganir, R. L. (2006).

Synapse-specific regulation of AMPA receptor function by PSD-95. *Proc. Natl. Acad. Sci.* 103, 19535–19540. doi:10.1073/pnas.0608492103.

Berweck, S., Walther, M., Brodbeck, V., Wagner, N., Koerte, I., Henschel, V., et al. (2008). Abnormal motor cortex excitability in congenital stroke. *Pediatr. Res.* 63, 84–8. doi:10.1203/PDR.0b013e31815b88f1.

Binienda, Z., Holson, R. R., Chen, F. X., Oriaku, E., Kim, C. S., Flynn, T. J., et al. (1996). Effects of ischemia-hypoxia induced by interruption of uterine blood flow on fetal rat liver and brain enzyme activities and offspring behavior. *Int. J. Dev. Neurosci.* 14, 399–408. doi:10.1016/S0736-5748(96)00025-1.

Boeckers, T. M. (2006). The postsynaptic density. *Cell Tissue Res.* 326, 409–422. doi:10.1007/s00441-006-0274-5.

Boyken, J., Grønborg, M., Riedel, D., Urlaub, H., Jahn, R., and Chua, J. (2013). Molecular Profiling of Synaptic Vesicle Docking Sites Reveals Novel Proteins but Few Differences between Glutamatergic and GABAergic Synapses. *Neuron* 78, 285–297. doi:10.1016/j.neuron.2013.02.027.

Braak, H. (1974). On the structure of the human archicortex. I. The cornu ammonis. A Golgi and pigmentarchitectonic study. *Cell Tissue Res.* 152, 349–83. doi:10.1007/BF00223955.

Brett, M., Johnsrude, I. S., and Owen, A. M. (2002). The problem of functional localization in the human brain. *Nat. Rev. Neurosci.* 3, 243–249. doi:10.1038/nrn756.

Broderick, J. P., Brott, T. G., Duldner, J. E., Tomsick, T., and Huster, G. (1993). Volume of intracerebral hemorrhage: A powerful and easy-to-use predictor of 30-day mortality. *Stroke* 24, 987–993. doi:10.1161/01.STR.24.7.987.

Brodin, L., Bakeeva, L., and Shupliakov, O. (1999). Presynaptic mitochondria and the temporal pattern of neurotransmitter release. *Philos. Trans. R. Soc. Lond. B. Biol. Sci.* 354, 365–72. doi:10.1098/rstb.1999.0388.

Broughton, B. R. S., Reutens, D. C., and Sobey, C. G. (2009). Apoptotic mechanisms after cerebral ischemia. *Stroke* 40. doi:10.1161/STROKEAHA.108.531632.

Brown, C. A., Campbell, M. C., Karimi, M., Tabbal, S. D., Loftin, S. K., Tian, L. L., et al. (2012). Dopamine pathway loss in nucleus accumbens and ventral tegmental area predicts apathetic behavior in MPTP-lesioned monkeys. *Exp. Neurol.* 236, 190–197. doi:10.1016/j.expneurol.2012.04.025.

Brown, C. E., Aminoltejari, K., Erb, H., Winship, I. R., and Murphy, T. H. (2009). In vivo

voltage-sensitive dye imaging in adult mice reveals that somatosensory maps lost to stroke are replaced over weeks by new structural and functional circuits with prolonged modes of activation within both the peri-infarct zone and distant sites. *J. Neurosci.* 29, 1719–34. doi:10.1523/JNEUROSCI.4249-08.2009.

Brown, C. E., Li, P., Boyd, J. D., Delaney, K. R., and Murphy, T. H. (2007). Extensive Turnover of Dendritic Spines and Vascular Remodeling in Cortical Tissues Recovering from Stroke. *J. Neurosci.* 27, 4101–4109. doi:10.1523/JNEUROSCI.4295-06.2007.

Brown, C. E., Wong, C., and Murphy, T. H. (2008). Rapid Morphologic Plasticity of Peri-Infarct Dendritic Spines After Focal Ischemic Stroke. *Stroke* 39, 1286 LP-1291. Available at: http://stroke.ahajournals.org/content/39/4/1286.abstract.

Burette, A., Collman, F., Micheva, K. D., Smith, S. J., and Weinberg, R. J. (2015). Knowing a synapse when you see one. *Front. Neuroanat.* 9, 1–8. doi:10.3389/fnana.2015.00100.

Carmichael, S. T., Kathirvelu, B., Schweppe, C. A., and Nie, E. H. (2017). Molecular, cellular and functional events in axonal sprouting after stroke. *Exp. Neurol.* 287, 384–394. doi:10.1016/j.expneurol.2016.02.007.

Casals, J. B., Pieri, N. C. G., Feitosa, M. L. T., Ercolin, A. C. M., Roballo, K. C. S., Barreto, R. S. N., et al. (2011). The use of animal models for stroke research: a review. *Comp. Med.* 61, 305–13. Available at: http://www.ncbi.nlm.nih.gov/pubmed/22330245%5Cnhttp://www.pubmedcentral.nih.gov/articlerender.fcgi?artid=PMC3155396.

Castorph, S., Riedel, D., Arleth, L., Sztucki, M., Jahn, R., Holt, M., et al. (2010). Structure Parameters of Synaptic Vesicles Quantified by Small-Angle X-Ray Scattering. *Biophys. J.* 98, 1200–1208. doi:10.1016/j.bpj.2009.12.4278.

Charness, G., Gneezy, U., and Kuhn, M. A. (2012). Experimental methods: Between-subject and within-subject design. *J. Econ. Behav. Organ.* 81, 1–8. doi:10.1016/j.jebo.2011.08.009.

Chih, B., Engelman, H., and Scheiffele, P. (2005). Control of excitatory and inhibitory synapse formation by neuroligins. *Science (80-.).* 307, 1324–1328. doi:10.1126/science.1107470.

Choquet, D., and Triller, A. (2013). The dynamic synapse. *Neuron* 80, 691–703. doi:10.1016/j.neuron.2013.10.013.

Chubykin, A. A., Atasoy, D., Etherton, M. R., Brose, N., Kavalali, E. T., Gibson, J. R., et al. (2007). Activity-Dependent Validation of Excitatory versus Inhibitory Synapses by Neuroligin-1 versus Neuroligin-2. *Neuron* 54, 919–931. doi:10.1016/j.neuron.2007.05.029.

Chung, W. S., Allen, N. J., and Eroglu, C. (2015). Astrocytes control synapse formation, function, and elimination. *Cold Spring Harb. Perspect. Biol.* 7. doi:10.1101/cshperspect.a020370.

Clarkson, A. N., and Carmichael, S. T. (2009). Cortical excitability and post-stroke recovery. *Biochem. Soc. Trans.* 37, 1412–1414. doi:10.1042/BST0371412.

Connell, L. A. (2007). Sensory Impairment and Recovery After Stroke. *Univ. Nottingham*, 274. Available at: http://eprints.nottingham.ac.uk/10247/.

Crochet, S., and Petersen, C. C. H. (2009). Cortical Dynamics by Layers. *Neuron* 64, 298–300. doi:10.1016/j.neuron.2009.10.024.

De Carlos, J. A., and Borrell, J. (2007). A historical reflection of the contributions of Cajal and Golgi to the foundations of neuroscience. *Brain Res. Rev.* 55, 8–16. doi:10.1016/j.brainresrev.2007.03.010.

Donohue, D. E., and Ascoli, G. A. (2011). Automated reconstruction of neuronal morphology: An overview. *Brain Res. Rev.* 67, 94–102. doi:10.1016/j.brainresrev.2010.11.003.

Engel, O., Kolodziej, S., Dirnagl, U., and Prinz, V. (2011). Modeling Stroke in Mice - Middle Cerebral Artery Occlusion with the Filament Model. *J. Vis. Exp.* doi:10.3791/2423.

Fiedler, J., Přibáň, V., Škoda, O., Schenk, I., Schenková, V., and Poláková, S. (2011). Cognitive outcome after EC-IC bypass surgery in hemodynamic cerebral ischemia. *Acta Neurochir. (Wien).* 153, 1303–1311. doi:10.1007/s00701-011-0949-x.

Fisher, C. M. (1971). Pathological observations in hypertensive cerebral hemorrhage. *J. Neuropathol. Exp. Neurol.* 30, 536–550. doi:10.1097/00005072-197107000-00015.

Fletcher, D. A., and Mullins, R. D. (2010). Cell mechanics and the cytoskeleton. *Nature* 463, 485–492. doi:10.1038/nature08908.

Fluri, F., Schuhmann, M. K., and Kleinschnitz, C. (2015). Animal models of ischemic stroke and their application in clinical research. *Drug Des. Devel. Ther.* 9, 3445–3454. doi:10.2147/DDDT.S56071.

Franzén, L. E., Ekstedt, M., Kechagias, S., and Bodin, L. (2005). Semiquantitative evaluation overestimates the degree of steatosis in liver biopsies: A comparison to stereological point counting. *Mod. Pathol.* 18, 912–916. doi:10.1038/modpathol.3800370.

Freeman, M. R., Delrow, J., Kim, J., Johnson, E., and Doe, C. Q. (2003). Unwrapping glial biology: Gcm target genes regulating glial development, diversification, and function. *Neuron* 38, 567–580. doi:10.1016/S0896-6273(03)00289-7.

Friedman, R. M., Chen, L. M., and Roe, A. W. (2004). Modality maps within primate somatosensory cortex. *Proc. Natl. Acad. Sci.* 101, 12724–12729. doi:10.1073/pnas.0404884101.

Frotscher, M., Haas, C. A., and Förster, E. (2003). Reelin controls granule cell migration in the dentate gyrus by acting on the radial glial scaffold. *Cereb. Cortex* 13, 634–640. doi:10.1093/cercor/13.6.634.

Ghanavati, S., Lerch, J. P., and Sled, J. G. (2014). Automatic anatomical labeling of the complete cerebral vasculature in mouse models. *Neuroimage* 95, 117–128. doi:10.1016/j.neuroimage.2014.03.044.

Goldhaber, S. Z., and Bounameaux, H. (2012). Pulmonary embolism and deep vein thrombosis. in *The Lancet*, 1835–1846. doi:10.1016/S0140-6736(11)61904-1.

Gray, E. G. (1963). Electron microscopy of presynaptic organelles of the spinal cord. *J. Anat.* 97, 101–6. Available at: http://www.ncbi.nlm.nih.gov/pubmed/13949972%5Cnhttp://www.pubmedcentral.nih.gov/articlerender.fcgi?artid=PMC1244260%5Cnhttp://www.pubmedcentral.nih.gov/articlerender.fcgi?artid=1244260&tool=pmcentrez&rendertype=abstract.

Grefkes, C., and Ward, N. S. (2014). Cortical reorganization after stroke: How much and how functional? *Neuroscientist* 20, 56–70. doi:10.1177/1073858413491147.

Haley, M. J., and Lawrence, C. B. (2017). The blood–brain barrier after stroke: Structural studies and the role of transcytotic vesicles. *J. Cereb. Blood Flow Metab.* 37, 456–470. doi:10.1177/0271678X16629976.

Hama, S., Yamashita, H., Yamawaki, S., and Kurisu, K. (2011). Post-stroke depression and apathy: Interactions between functional recovery, lesion location, and emotional response. *Psychogeriatrics* 11, 68–76. doi:10.1111/j.1479-8301.2011.00358.x.

Hansson, E., and Rönnbäck, L. (2003). Glial neuronal signaling in the central nervous system. *FASEB J.* 17, 341–8. doi:10.1096/fj.02-0429rev.

Hartings, J. A., Rolli, M. L., Lu, X.-C. M., and Tortella, F. C. (2003). Delayed secondary phase of peri-infarct depolarizations after focal cerebral ischemia: relation to infarct growth and neuroprotection. *J. Neurosci.* 23, 11602–10. doi:23/37/11602 [pii].

Heni, M., Hennige, A. M., Peter, A., Siegel-Axel, D., Ordelheide, A.-M., Krebs, N., et al. (2011). Insulin Promotes Glycogen Storage and Cell Proliferation in Primary Human Astrocytes. *PLoS One* 6, e21594. doi:10.1371/journal.pone.0021594.

High, B., Cole, A. A., Chen, X., and Reese, T. S. (2015). Electron microscopic tomography reveals discrete transcleft elements at excitatory and inhibitory synapses. *Front. Synaptic Neurosci.* 7. doi:10.3389/fnsyn.2015.00009.

Hossain, M. I., Roulston, C. L., and Stapleton, D. I. (2014). Molecular basis of impaired glycogen metabolism during ischemic stroke and hypoxia. *PLoS One* 9. doi:10.1371/journal.pone.0097570.

Hossmann, K. A. (1998). Experimental models for the investigation of brain ischemia. *Cardiovasc. Res.* 39, 106–20. doi:10.1016/S0008-6363(98)00075-3.

Hultén, L. M., and Levin, M. (2009). The role of hypoxia in atherosclerosis. *Curr. Opin. Lipidol.* 20, 409–414. doi:10.1097/MOL.0b013e3283307be8.

Iadecola, C., and Alexander, M. (2001). Cerebral ischemia and inflammation. *Curr. Opin. Neurol.* 14, 89–94. doi:10.1097/00019052-200102000-00014.

Imig, C., Min, S.-W., Krinner, S., Arancillo, M., Rosenmund, C., Südhof, T. C., et al. (2014). The Morphological and Molecular Nature of Synaptic Vesicle Priming at Presynaptic Active Zones. *Neuron* 84, 416–431. doi:10.1016/j.neuron.2014.10.009.

Inoue, S., and Oldenbourg, R. (1994). Microscopes. *Handb. Opt. Vol. 2 Devices, Meas. Prop.*, 1568.

Jackson, F. R., and Haydon, P. G. (2008). Glial cell regulation of neurotransmission and behavior in Drosophila. *Neuron Glia Biol.* 4, 11–17. doi:10.1017/S1740925X09000027.

Jewett, M. C., Fritz, B. R., Timmerman, L. E., and Church, G. M. (2013). In vitro integration of ribosomal RNA synthesis, ribosome assembly, and translation. *Mol. Syst. Biol.* 9. doi:10.1038/msb.2013.31.

Johnston, S. C., Mendis, S., and Mathers, C. D. (2009). Global variation in stroke burden and mortality: estimates from monitoring, surveillance, and modelling. *Lancet Neurol.* 8, 345–354. doi:10.1016/S1474-4422(09)70023-7.

Kaas, J. H. (2004). Evolution of somatosensory and motor cortex in primates. in *Anatomical Record - Part A Discoveries in Molecular, Cellular, and Evolutionary Biology*, 1148–1156. doi:10.1002/ar.a.20120.

Kaas, J., Nelson, R., Sur, M., Lin, C., and Merzenich, M. (1979). Multiple representations of the body within the primary somatosensory cortex of primates. *Science (80-.).* 204, 521–523. doi:10.1126/science.107591.

Kajihara, H., Tsutsumi, E., Kinoshita, A., Nakano, J., Takagi, K., and Takeo, S. (2001). Activated

astrocytes with glycogen accumulation in ischemic penumbra during the early stage of brain infarction: Immunohistochemical and electron microscopic studies. *Brain Res.* 909, 92–101. doi:10.1016/S0006-8993(01)02640-3.

Kalaria, R. N., Akinyemi, R., and Ihara, M. (2016). Stroke injury, cognitive impairment and vascular dementia. *Biochim. Biophys. Acta - Mol. Basis Dis.* 1862, 915–925. doi:10.1016/j.bbadis.2016.01.015.

Kaneko, Y., Danev, R., Nitta, K., and Nagayama, K. (2005). In vivo subcellular ultrastructures recognized with Hilbert differential contrast transmission electron microscopy. *J. Electron Microsc. (Tokyo).* 54, 79–84. doi:10.1093/jmicro/dfh105.

Kerr, P. B., Caputy, A. J., and Horwitz, N. H. (2005). A history of cerebral localization. *Neurosurg. Focus* 18, e1. Available at: http://www.ncbi.nlm.nih.gov/pubmed/20183202.

Kim, M. J., Futai, K., Jo, J., Hayashi, Y., Cho, K., and Sheng, M. (2007). Synaptic Accumulation of PSD-95 and Synaptic Function Regulated by Phosphorylation of Serine-295 of PSD-95. *Neuron* 56, 488–502. doi:10.1016/j.neuron.2007.09.007.

Kim, S. Y., Hsu, J. E., Husbands, L. C., Kleim, J. A., and Jones, T. A. (2017). Coordinated plasticity of synapses and astrocytes underlies practice-driven functional vicariation in peri-infarct motor cortex. *J. Neurosci.* 38, 1295–17. doi:10.1523/JNEUROSCI.1295-17.2017.

Kim, Y. K., Yang, E. J., Cho, K., Lim, J. Y., and Paik, N. J. (2014). Functional recovery after ischemic stroke is associated with reduced gabaergic inhibition in the cerebral cortex: A GABA PET study. *Neurorehabil. Neural Repair* 28, 576–583. doi:10.1177/1545968313520411.

Koch, C., and Laurent, G. (1999). Complexity and the nervous system. *Science (80-.).* 284, 96–98. doi:10.1126/science.284.5411.96.

Labat-gest, V., and Tomasi, S. (2013). Photothrombotic Ischemia: A Minimally Invasive and Reproducible Photochemical Cortical Lesion Model for Mouse Stroke Studies. *J. Vis. Exp.*, 50370. doi:10.3791/50370.

Lai, T. W., Zhang, S., and Wang, Y. T. (2014). Excitotoxicity and stroke: Identifying novel targets for neuroprotection. *Prog. Neurobiol.* 115, 157–188. doi:10.1016/j.pneurobio.2013.11.006.

Lam, D. M. K., Wiesel, T. N., and Kaneko, A. (1974). Neurotransmitter synthesis in cephalopod retina. *Brain Res.* 82, 365–368. doi:10.1016/0006-8993(74)90621-0.

Langhorne, P., Bernhardt, J., and Kwakkel, G. (2011). Stroke rehabilitation. *Lancet* 377, 1693–1702. doi:10.1016/S0140-6736(11)60325-5.

Langhorne, P., Coupar, F., and Pollock, A. (2009). Motor recovery after stroke: a systematic review. *Lancet Neurol.* 8, 741–754. doi:10.1016/S1474-4422(09)70150-4.

Lawrence, P. F., Alves, J. C., Jicha, D., Bhirangi, K., Dobrin, P. B., and Lamparello, P. J. (1998). Incidence, timing, and causes of cerebral ischemia during carotid endarterectomy with regional anesthesia. *J. Vasc. Surg.* 27, 329–337. doi:10.1016/S0741-5214(98)70363-5.

Li, Y., Powers, C., Jiang, N., and Chopp, M. (1998). Intact, injured, necrotic and apoptotic cells after focal cerebral ischemia in the rat. *J. Neurol. Sci.* 156, 119–132. doi:10.1016/S0022-510X(98)00036-7.

Lim, S. F., Riehn, R., Ryu, W. S., Khanarian, N., Tung, C. K., Tank, D., et al. (2006). In vivo and scanning electron microscopy imaging of upconverting nanophosphors in Caenorhabditis elegans. *Nano Lett.* 6, 169–174. doi:10.1021/nl0519175.

Lusis, A. J. (2000). Atherosclerosis. *Nature* 407, 233–241. doi:10.1038/35025203.

Machado, A. G., Baker, K. B., Schuster, D., Butler, R. S., and Rezai, A. (2009). Chronic electrical stimulation of the contralesional lateral cerebellar nucleus enhances recovery of motor function after cerebral ischemia in rats. *Brain Res.* 1280, 107–116. doi:10.1016/j.brainres.2009.05.007.

Majde, J. a (2003). Animal models for hemorrhage and resuscitation research. *J. Trauma* 54, S100–S105. doi:10.1097/01.TA.0000064503.24416.F4.

Malenka, R. C., and Bear, M. F. (2004). LTP and LTD: An embarrassment of riches. *Neuron* 44, 5–21. doi:10.1016/j.neuron.2004.09.012.

Martin, L. J., Al-Abdulla, N. A., Brambrink, A. M., Kiesch, J. R., Sieber, F. E., and Portera-Cailliau, C. (1998). Neurodegeneration in excitotoxicity, global cerebral ischemia, and target deprivation: A perspective on the contributions of apoptosis and necrosis. *Brain Res. Bull.* 46, 281–309. doi:10.1016/S0361-9230(98)00024-0.

Masland, R. H. (2004). Neuronal cell types. *Curr. Biol.* 14, R497–R500. doi:10.1016/j.cub.2004.06.035.

McGeoch, P. D., Brang, D., Huang, M., and Ramachandran, V. S. (2015). Primary somatosensory cortex hand representation dynamically modulated by motor output. *Neurocase* 21, 103–105. doi:10.1080/13554794.2013.873060.

Metea, M. R. (2006). Glial Cells Dilate and Constrict Blood Vessels: A Mechanism of Neurovascular Coupling. *J. Neurosci.* 26, 2862–2870. doi:10.1523/JNEUROSCI.4048-05.2006.

Miller, D. W., Cookson, M. R., and Dickson, D. W. (2004). Glial cell inclusions and the pathogenesis of neurodegenerative diseases. *Neuron Glia Biol.* 1, 13–21. doi:10.1017/S1740925X04000043.

Morales, J., Alonso-Nanclares, L., Rodríguez, J.-R., DeFelipe, J., Rodríguez, Á., and Merchán-Pérez, Á. (2011). Espina: A Tool for the Automated Segmentation and Counting of Synapses in Large Stacks of Electron Microscopy Images. *Front. Neuroanat.* 5. doi:10.3389/fnana.2011.00018.

Mullins, C. (2005). *The Biogenesis of Cellular Organelles.* Boston, MA: Springer US doi:10.1007/b138220.

Murthy, V. N., and De Camilli, P. (2003). Cell Biology Of The Presynaptic Terminal. *Annu. Rev. Neurosci* 26, 701–728. doi:10.1146/annurev.neuro.26.041002.131445.

Nahirney, P. C., Reeson, P., and Brown, C. E. (2016). Ultrastructural analysis of blood–brain barrier breakdown in the peri-infarct zone in young adult and aged mice. *J. Cereb. Blood Flow Metab.* 36, 413–425. doi:10.1177/0271678X15608396.

Nathaniel, T. I., Williams-Hernandez, A., Hunter, L. A., Liddy, C., Peffley, D. M., Umesiri, F. E., et al. (2015). Tissue hypoxia during ischemic stroke: Adaptive clues from hypoxia-tolerant animal models. *Brain Res. Bull.* 114, 1–12. doi:10.1016/j.brainresbull.2015.02.006.

Nathanson, N. M. (2006). “Muscarinic Acetylcholine Receptors,” in *Encyclopedia of Life Sciences* (Chichester, UK: John Wiley & Sons, Ltd), 3573–3581. doi:10.1038/npg.els.0004078.

Nelson, S. B., Hempel, C., and Sugino, K. (2006). Probing the transcriptome of neuronal cell types. *Curr. Opin. Neurobiol.* 16, 571–576. doi:10.1016/j.conb.2006.08.006.

Ng, Y. S., Stein, J., Ning, M., and Black-Schaffer, R. M. (2007). Comparison of clinical characteristics and functional outcomes of ischemic stroke in different vascular territories. *Stroke.* 38, 2309–14. doi:10.1161/STROKEAHA.106.475483.

Nieto-Sampedro, M., Hoff, S. F., and Cotman, C. W. (1982). Perforated postsynaptic densities: probable intermediates in synapse turnover. *Proc. Natl. Acad. Sci. U. S. A.* 79, 5718–22. Available at: /pmc/articles/PMC346976/?report=abstract.

Nimchinsky, E. A., Sabatini, B. L., and Svoboda, K. (2002). Structure and Function of Dendritic Spines. *Annu. Rev. Physiol.* 64, 313–353. doi:10.1146/annurev.physiol.64.081501.160008.

Ogden, D., and Stanfield, P. (1981). Patch clamp techniques for single channel and whole-cell recording. *Currents* 2, 53–78. doi:10.1523/JNEUROSCI.4368-15.2016.

Olmez, I., and Ozyurt, H. (2012). Reactive oxygen species and ischemic cerebrovascular disease. *Neurochem. Int.* 60, 208–212. doi:10.1016/j.neuint.2011.11.009.

Paolicelli, R. C., Bolasco, G., Pagani, F., Maggi, L., Scianni, M., Panzanelli, P., et al. (2011). Synaptic pruning by microglia is necessary for normal brain development. *Science (80-.).* 333, 1456–1458. doi:10.1126/science.1202529.

Patel, S. A., Nagy, J. O., Bolstad, E. D., Gerdes, J. M., and Thompson, C. M. (2007). Tetrapeptide inhibitors of the glutamate vesicular transporter (VGLUT). *Bioorganic Med. Chem. Lett.* 17, 5125–5128. doi:10.1016/j.bmcl.2007.07.006.

Peljto, M., and Wichterle, H. (2011). Programming embryonic stem cells to neuronal subtypes. *Curr. Opin. Neurobiol.* 21, 43–51. doi:10.1016/j.conb.2010.09.012.

Rochefort, N. L., and Konnerth, A. (2012). Dendritic spines: From structure to in vivo function. *EMBO Rep.* 13, 699–708. doi:10.1038/embor.2012.102.

Rodan, L., McCrindle, B. W., Manlhiot, C., MacGregor, D. L., Askalan, R., Moharir, M., et al. (2012). Stroke recurrence in children with congenital heart disease. *Ann. Neurol.* 72, 103–111. doi:10.1002/ana.23574.

Rodnina, M. V., Serebryanik, A. I., Ovcharenko, G. V., and El'skaya, A. V. (1994). ATPase Strongly Bound to Higher Eukaryotic Ribosomes. *Eur. J. Biochem.* 225, 305–310. doi:10.1111/j.1432-1033.1994.00305.x.

Rosoklija, G. B., Petrushevski, V. M., Stankov, A., Dika, A., Jakovski, Z., Pavlovski, G., et al. (2014). Reliable and durable Golgi staining of brain tissue from human autopsies and experimental animals. *J. Neurosci. Methods* 230, 20–29. doi:10.1016/j.jneumeth.2014.04.006.

Sandoval, K. E., and Witt, K. A. (2008). Blood-brain barrier tight junction permeability and ischemic stroke. *Neurobiol. Dis.* 32, 200–219. doi:10.1016/j.nbd.2008.08.005.

Schaechter, J. D. (2004). Motor rehabilitation and brain plasticity after hemiparetic stroke. *Prog. Neurobiol.* 73, 61–72. doi:10.1016/j.pneurobio.2004.04.001.

Schepers, V., Post, M., Visser-Meily, A., Van De Port, I., Akhmouch, M., and Lindeman, E. (2009). Prediction of depressive symptoms up to three years post-stroke. *J. Rehabil. Med.* 41, 930–935. doi:10.2340/16501977-0446.

Schmitz, S. K., Hjorth, J. J. J., Joemai, R. M. S., Wijntjes, R., Eijgenraam, S., de Bruijn, P., et al. (2011). Automated analysis of neuronal morphology, synapse number and synaptic recruitment. *J. Neurosci. Methods* 195, 185–193. doi:10.1016/j.jneumeth.2010.12.011.

Scholtyseck, E., and Mehlhorn, H. (1970). Ultrastructural study of characteristic organelles (paired organelles, micronemes, micropores) of sporozoa and related organisms. *Z. Parasitenkd.* 34, 97–127. doi:10.1007/BF00260383.

Seitz, R. J., Hoflich, P., Binkofski, F., Tellmann, L., Herzog, H., and Freund, H. J. (1998). Role of the premotor cortex in recovery from middle cerebral artery infarction. *Arch Neurol* 55, 1081–1088. Available at: http://www.ncbi.nlm.nih.gov/pubmed/9708958%5Cnhttp://archneur.jamanetwork.com/data/Journals/NEUR/7658/noc7487.pdf.

Selnes, O. a, and Hillis, a (2000). Patient Tan revisited: a case of atypical global aphasia? *J. Hist. Neurosci.* 9, 233–7. doi:10.1076/0964-704X(200012)9:3;1-A;FT233.

Shea, S., and Di Tullio, M. (2013). Atrial fibrillation, silent cerebral ischemia, and cognitive function. *J. Am. Coll. Cardiol.* 62, 1998–1999. doi:10.1016/j.jacc.2013.06.025.

Sheng, M., and Kim, E. (2011). The postsynaptic organization of synapses. *Cold Spring Harb. Perspect. Biol.* 3. doi:10.1101/cshperspect.a005678.

Sheng, M., and Kim, M. J. (2002). Postsynaptic signaling and plasticity mechanisms. *Science (80-.).* 298, 776–780. doi:10.1126/science.1075333.

Shigeno, S., Sasaki, T., and Haszprunar, G. (2007). Central nervous system of Chaetoderma japonicum (Caudofoveata, Aplacophora): Implications for diversified ganglionic plans in early molluscan evolution. *Biol. Bull.* 213, 122–134. doi:10.2307/25066628.

Shigeno, S., Tsuchiya, K., and Segawa, S. (2001). Embryonic and paralarval development of the central nervous system of the loliginid squid Sepioteuthis lessoniana. *J. Comp. Neurol.* 437, 449–475. doi:10.1002/cne.1295.

Simpson, D. (2005). Phrenology and the neurosciences: contributions of F. J. Gall and J. G. Spurzheim. *ANZ J. Surg.* 75, 475–82. doi:10.1111/j.1445-2197.2005.03426.x.

Sims, N. R., and Yew, W. P. (2017). Reactive astrogliosis in stroke: Contributions of astrocytes to recovery of neurological function. *Neurochem. Int.* 107, 88–103. doi:10.1016/j.neuint.2016.12.016.

St. Pierre, T. G., House, M. J., Bangma, S. J., Pang, W., Bathgate, A., Gan, E. K., et al. (2016). Stereological analysis of liver biopsy histology sections as a reference standard for validating non-invasive liver fat fraction measurements by MRI. *PLoS One* 11, 1–18. doi:10.1371/journal.pone.0160789.

Strong, A. J., Anderson, P. J., Watts, H. R., Virley, D. J., Lloyd, A., Irving, E. A., et al. (2007).

Peri-infarct depolarizations lead to loss of perfusion in ischaemic gyrencephalic cerebral cortex. *Brain* 130, 995–1008. doi:10.1093/brain/awl392.

Stuart, G., Spruston, N., Sakmann, B., and Hausser, M. (1997). Action potential initiation and back propagation in neurons of the mammalian central nervous system. *Trends Neurosci.* 20, 125–131. doi:10.1016/S0166-2236(96)10075-8.

Swanson, L. W. (2013). "Basic principles of nervous system organization," in *Neuroscience in the 21st Century: From Basic to Clinical*, 1255–1288. doi:10.1007/978-1-4614-1997-6_44.

Takatsuru, Y., Fukumoto, D., Yoshitomo, M., Nemoto, T., Tsukada, H., and Nabekura, J. (2009). Neuronal Circuit Remodeling in the Contralateral Cortical Hemisphere during Functional Recovery from Cerebral Infarction. *J. Neurosci.* 29, 10081–10086. doi:10.1523/JNEUROSCI.1638-09.2009.

Tantama, M., Martínez-François, J. R., Mongeon, R., and Yellen, G. (2013). Imaging energy status in live cells with a fluorescent biosensor of the intracellular ATP-to-ADP ratio. *Nat. Commun.* 4. doi:10.1038/ncomms3550.

Tennant, K. A., Taylor, S. L., White, E. R., and Brown, C. E. (2017). Optogenetic rewiring of thalamocortical circuits to restore function in the stroke injured brain. *Nat. Commun.* 8, 1–14. doi:10.1038/ncomms15879.

Thrane, A. S., Rangroo Thrane, V., and Nedergaard, M. (2014). Drowning stars: reassessing the role of astrocytes in brain edema. *Trends Neurosci.* 37, 620–628. doi:10.1016/j.tins.2014.08.010.

Umegaki, M., Sanada, Y., Waerzeggers, Y., Rosner, G., Yoshimine, T., Heiss, W.-D., et al. (2005). Peri-infarct depolarizations reveal penumbra-like conditions in striatum. *J. Neurosci.* 25, 1387–94. doi:10.1523/JNEUROSCI.4182-04.2005.

Ünal-Çevik, I., Kilinç, M., Can, A., Gürsoy-Özdemir, Y., and Dalkara, T. (2004). Apoptotic and necrotic death mechanisms are concomitantly activated in the same cell after cerebral ischemia. *Stroke* 35, 2189–2194. doi:10.1161/01.STR.0000136149.81831.c5.

Uylings, H. B. M., and de Brabander, J. M. (2002). Neuronal Changes in Normal Human Aging and Alzheimer's Disease. *Brain Cogn.* 49, 268–276. doi:10.1006/brcg.2001.1500.

van de Pol, M., and Wright, J. (2009). A simple method for distinguishing within- versus between-subject effects using mixed models. *Anim. Behav.* 77, 753–758. doi:10.1016/j.anbehav.2008.11.006.

Von Bartheld, C. S. (2002). Counting particles in tissue sections: Choices of methods and

importance of calibration to minimize biases. *Histol. Histopathol.* 17, 639–648. doi:10.14670/HH-17.639.

Watila, M. M., and Balarabe, B. (2015). Factors predicting post-stroke aphasia recovery. *J. Neurol. Sci.* 352, 12–18. doi:10.1016/j.jns.2015.03.020.

Watson, B. D., Dietrich, W. D., Busto, R., Wachtel, M. S., and Ginsberg, M. D. (1985). Induction of reproducible brain infarction by photochemically initiated thrombosis. *Ann. Neurol.* 17, 497–504. doi:10.1002/ana.410170513.

Weisz, N., Wuhle, A., Monittola, G., Demarchi, G., Frey, J., Popov, T., et al. (2014). Prestimulus oscillatory power and connectivity patterns predispose conscious somatosensory perception. *Proc. Natl. Acad. Sci.* 111, E417–E425. doi:10.1073/pnas.1317267111.

Williams, D. B., and Carter, C. B. (2009). *Transmission electron microscopy: A textbook for materials science*. doi:10.1007/978-0-387-76501-3.

Willshaw, D. (2006). "Self-organization in the nervous system," in *Cognitive Systems - Information Processing Meets Brain Science*, 5–33. doi:10.1016/B978-012088566-4/50004-0.

Winship, I. R., and Murphy, T. H. (2009). Remapping the somatosensory cortex after stroke: Insight from imaging the synapse to network. *Neuroscientist* 15, 507–524. doi:10.1177/1073858409333076.

Wong, M., Wuethrich, P., Eggli, P., and Hunziker, E. (1996). Zone-specific cell biosynthetic activity in mature bovine articular cartilage: A new method using confocal microscopic stereology and quantitative autoradiography. *J. Orthop. Res.* 14, 424–432. doi:10.1002/jor.1100140313.

Yanagihara, T. (1974). Effect of Anoxia on Protein Metabolism in Subcellular Fractions of Rabbit Brain. *Stroke* 5, 226–229. doi:10.1161/01.STR.5.2.226.

Yonekura, I., Kawahara, N., Nakatomi, H., Furuya, K., and Kirino, T. (2004). A Model of Global Cerebral Ischemia in C57 BL/6 Mice. *J. Cereb. Blood Flow Metab.* 24, 151–158. doi:10.1097/01.WCB.0000096063.84070.C1.

Younts, T. J., Monday, H. R., Dudok, B., Klein, M. E., Jordan, B. A., Katona, I., et al. (2016). Presynaptic Protein Synthesis Is Required for Long-Term Plasticity of GABA Release. *Neuron* 92, 479–492. doi:10.1016/j.neuron.2016.09.040.

Zhang, J., Zhang, Y., Xing, S., Liang, Z., and Zeng, J. (2012). Secondary neurodegeneration in remote regions after focal cerebral infarction: A new target for stroke management? *Stroke*

43, 1700–1705. doi:10.1161/STROKEAHA.111.632448.

Zhao, Y., and Rempe, D. A. (2010). Targeting Astrocytes for Stroke Therapy. *Neurotherapeutics* 7, 439–451. doi:10.1016/j.nurt.2010.07.004.

Zhu, C., Zhao, J., Bibikova, M., Leverson, J. D., Bossy-Wetzel, E., Fan, J.-B., et al. (2005). Functional analysis of human microtubule-based motor proteins, the kinesins and dyneins, in mitosis/cytokinesis using RNA interference. *Mol. Biol. Cell* 16, 3187–99. doi:10.1091/mbc.E05-02-0167.

Appendix A: Neuronal ultrastructure and synaptic morphology

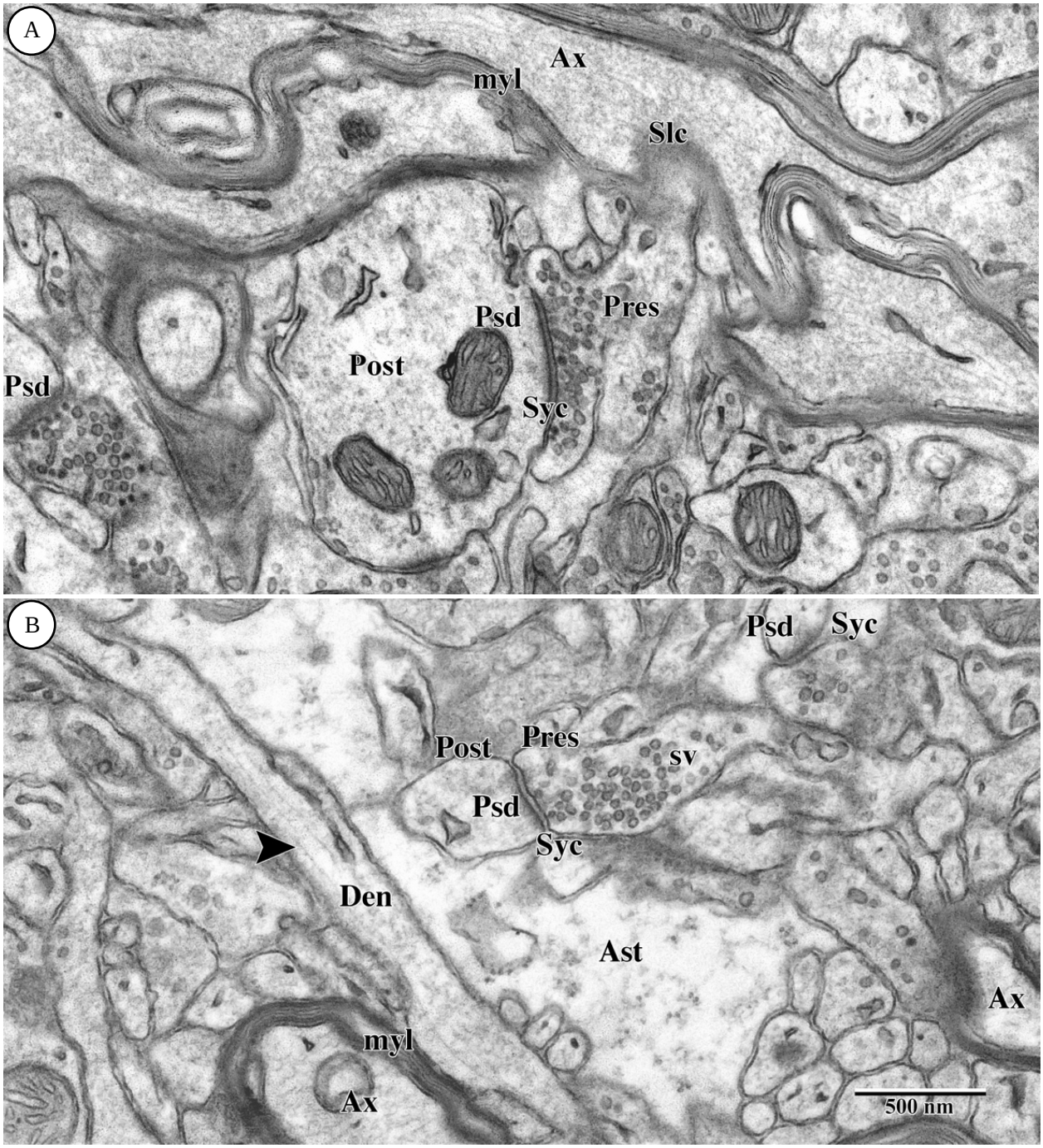

Figure 32: Synaptic structures within layer 3 of the PI in adult mouse SSC
Components of the synapse commonly encountered in EMs of neuronal tissue, which were used in constructing the criteria for identifying synapses. Pre- and postsynaptic terminals meet at the synaptic cleft, with astrocytic processes surrounding them (arrow). Ast, Astrocyte. Ax, axon. myl, myelination. Post, postsynaptic terminal. Pres, presynaptic terminal Psd, postsynaptic density. Sa, spine apparatus. sv, synaptic vesicles. Syc, synaptic cleft. Slc, Schmidt-Lanterman cleft. Microtubules (arrowhead) have also been identified. Image was taken using transmission

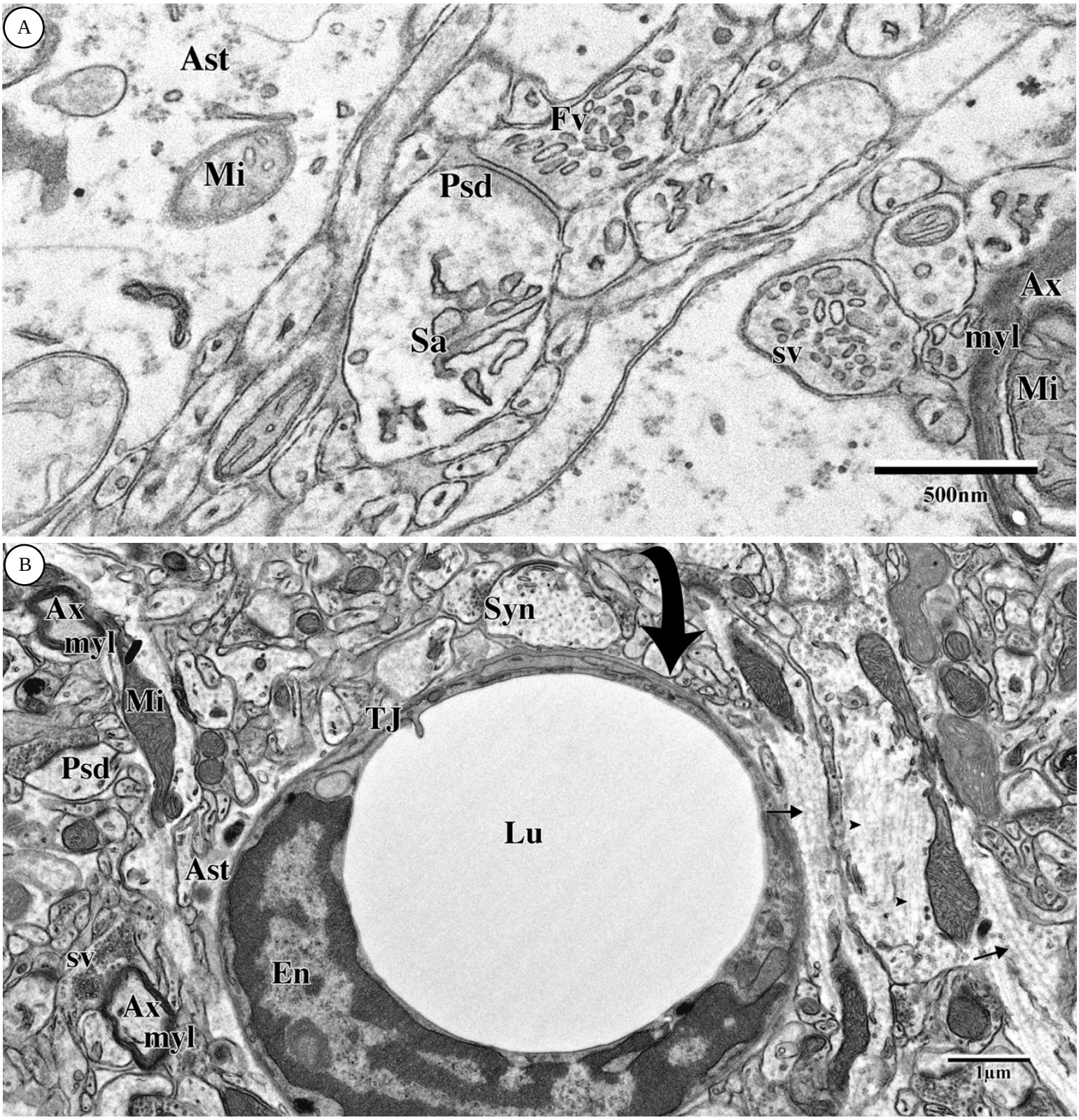

Figure 33. Neuronal and vascular structures within layer 3 of the adult mouse SSC.
(Above) proximal PI synapses 72 h post stroke, exihibiting abnormal structure and morphology. Synapses in the PI often show mixed characteristics. The synapse located in the centre of the EM shows evidence of postsynaptic density, while containing flattened vesicles in the presynaptic terminal, a trait common in inhibitory synapses. (Below) EM of the contralateral SSC captured at low magnification, displays structures typically found in proximity to cortical capillaries. Ast, Astrocyte. Ax, axon. En, Endothelial cell. Lu, lumen of capillary. Mi, Mitochondria. myl, myelination. Sa, spine apparatus. Fv, flattened vesicles. Syn, synapse. Syc, synaptic cleft. TJ, tight junction. Neurofilaments (arrowhead) and microtubules (arrow) and capillary (curved arrow) have also been indicated.

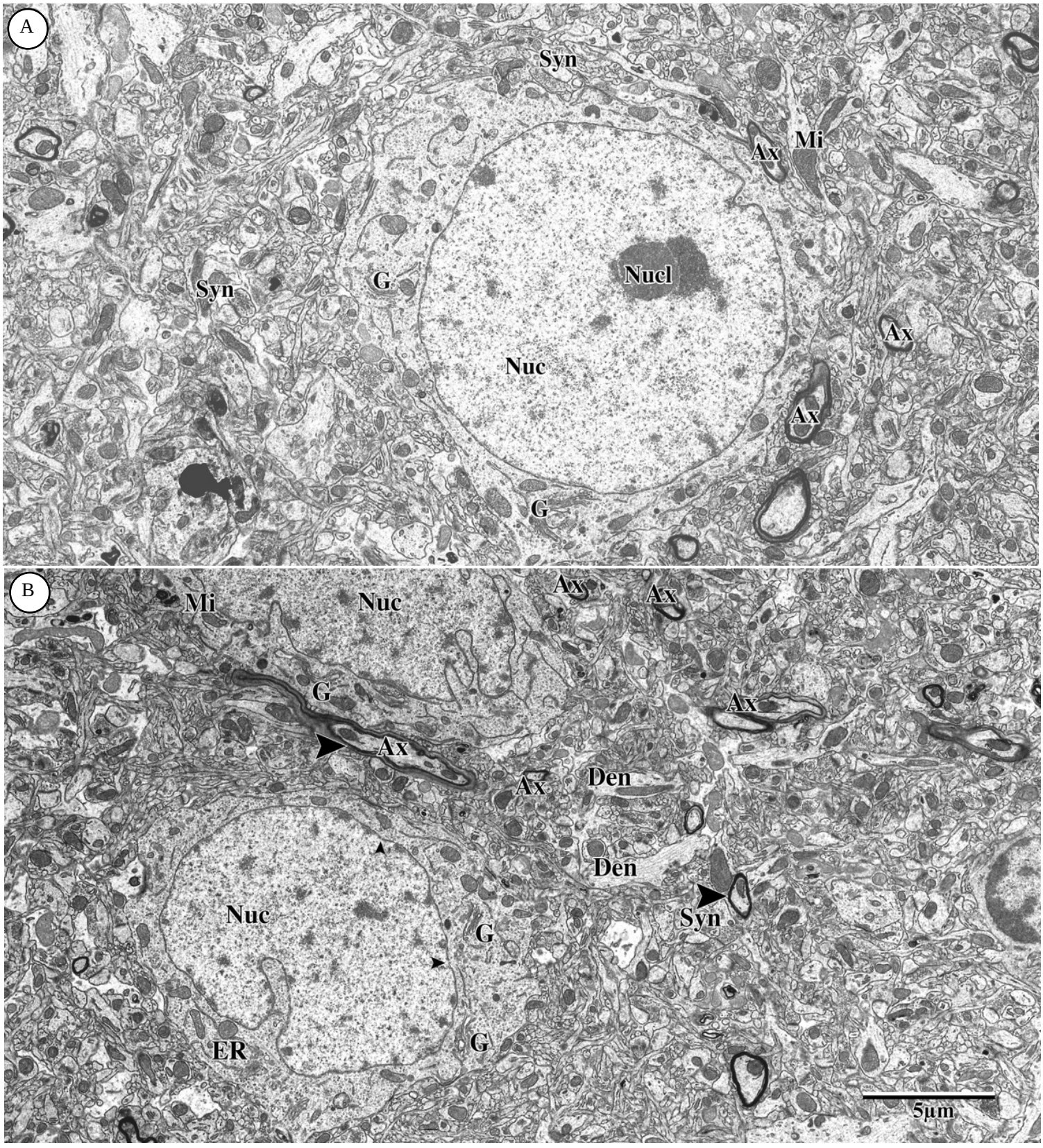

Figure 34. Low magnification EMs of pyramidal neurons within layer 5 contralateral adult mouse SSC
EMs show large pyramidal neurons of cortical layer 5 along with surrounding structures. Neurons deep within the cortex often show no dendritic offshoots, since these structures are sent to higher cortical layers. Pyramidal neurons within layer 5 are usually 15µm in size. Ax, axon. ER, endoplasmic reticulum. Den, dendrite. G, golgibody Mi, Mitochondria. Nuc, nucleus. Nucl, nucleolus. Syn, synapse. Syc, synaptic cleft. Myelination (arrowhead) surrounding axonal processes have been indicated.

Appendix B: Additional statistical data

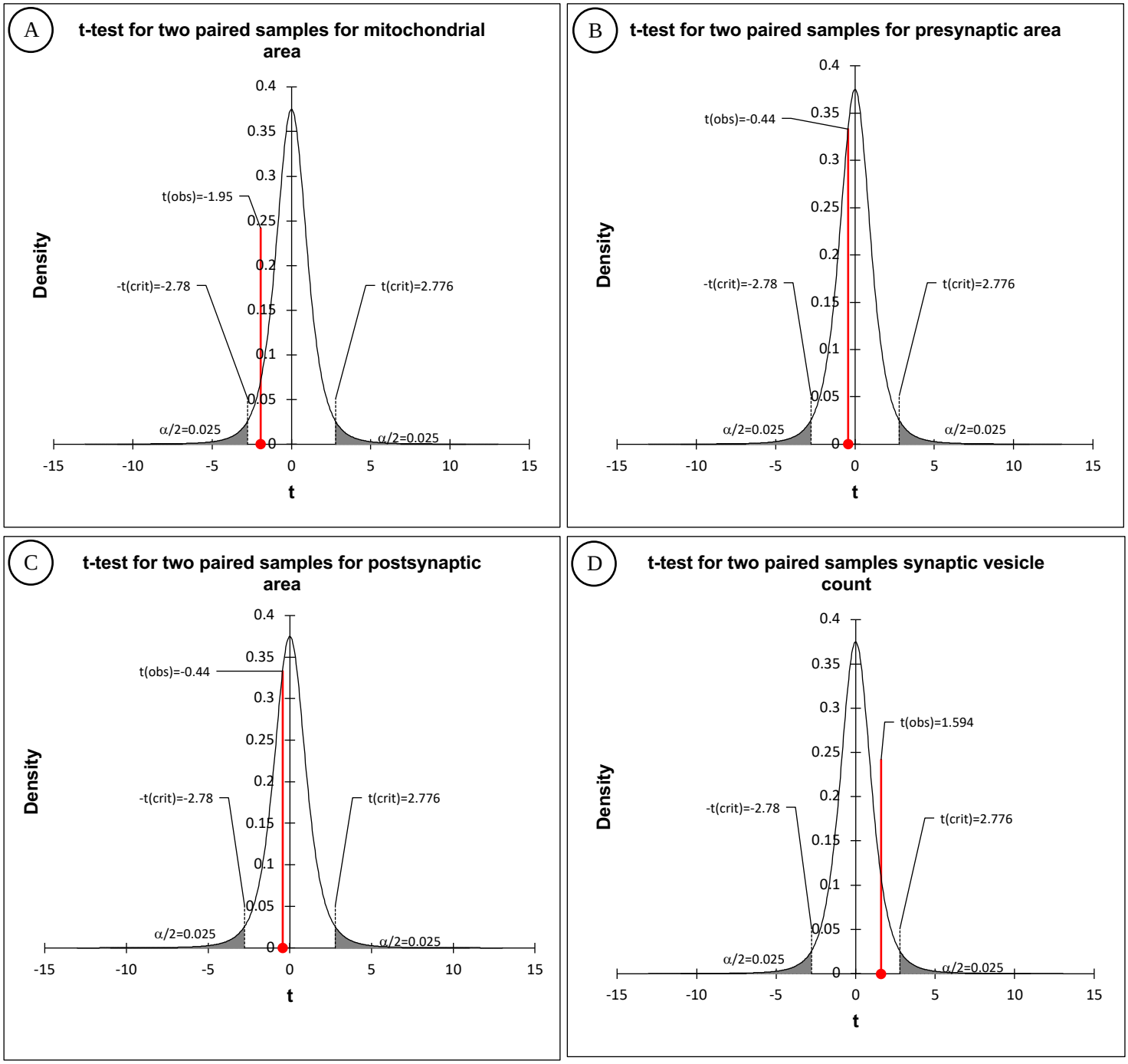

Figure 35: Sampling distribution of bidirectional hypotheses that were found to be not significant.
Bi-directional hypothesis was setup with $p<0.05$ considered to be significant. Each tail of the distribution received half of this p value. $t(obs) < t(crit)$, therefore $p>0.05$.

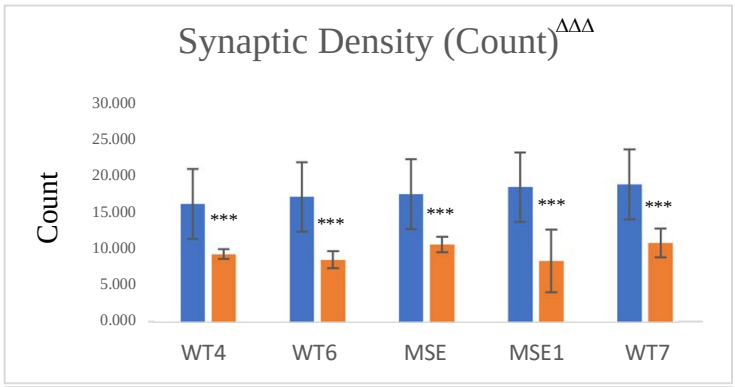
Synaptic Density (Count)ΔΔΔ
Count
30.000
25.000
20.000
15.000
10.000
5.000
0.000
***
WT4
WT6
MSE
MSE1
WT7

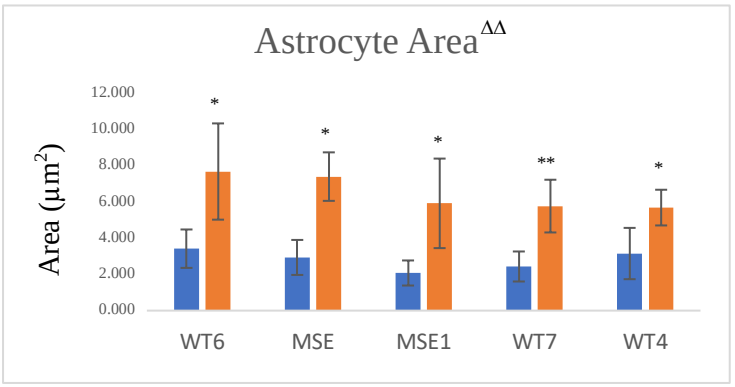
Astrocyte AreaΔΔ
Area (µm2)
12.000
10.000
8.000
6.000
4.000
2.000
0.000
*
**
WT6
MSE
MSE1
WT7
WT4

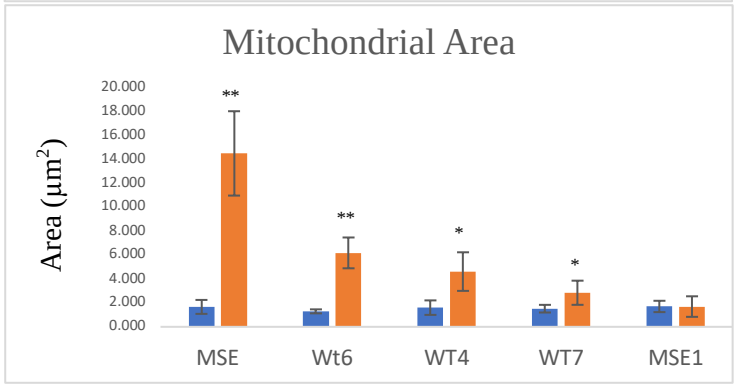
Mitochondrial Area
Area (µm2)
20.000
18.000
16.000
14.000
12.000
10.000
8.000
6.000
4.000
2.000
0.000
**
*
MSE
Wt6
WT4
WT7
MSE1

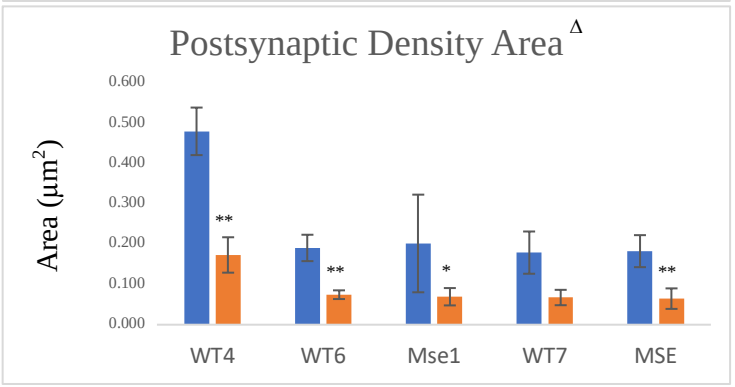
Postsynaptic Density AreaΔ
Area (µm2)
0.600
0.500
0.400
0.300
0.200
0.100
0.000
**
*
WT4
WT6
Mse1
WT7
MSE

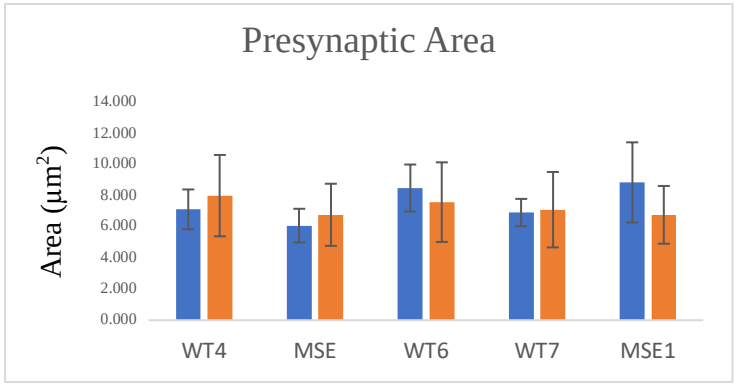
Presynaptic Area
Area (µm2)
14.000
12.000
10.000
8.000
6.000
4.000
2.000
0.000
WT4
MSE
WT6
WT7
MSE1

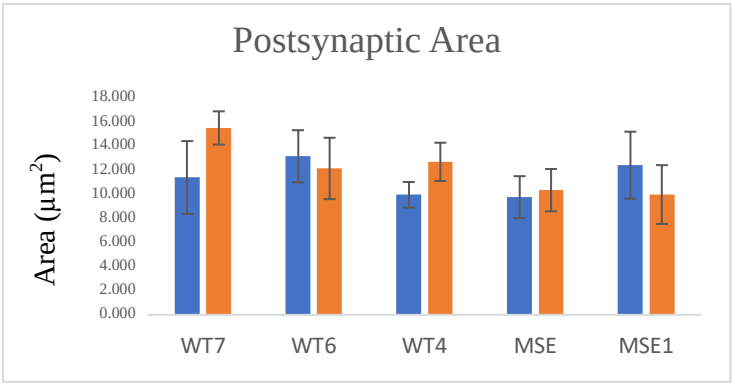
Postsynaptic Area
Area (µm2)
18.000
16.000
14.000
12.000
10.000
8.000
6.000
4.000
2.000
0.000
WT7
WT6
WT4
MSE
MSE1

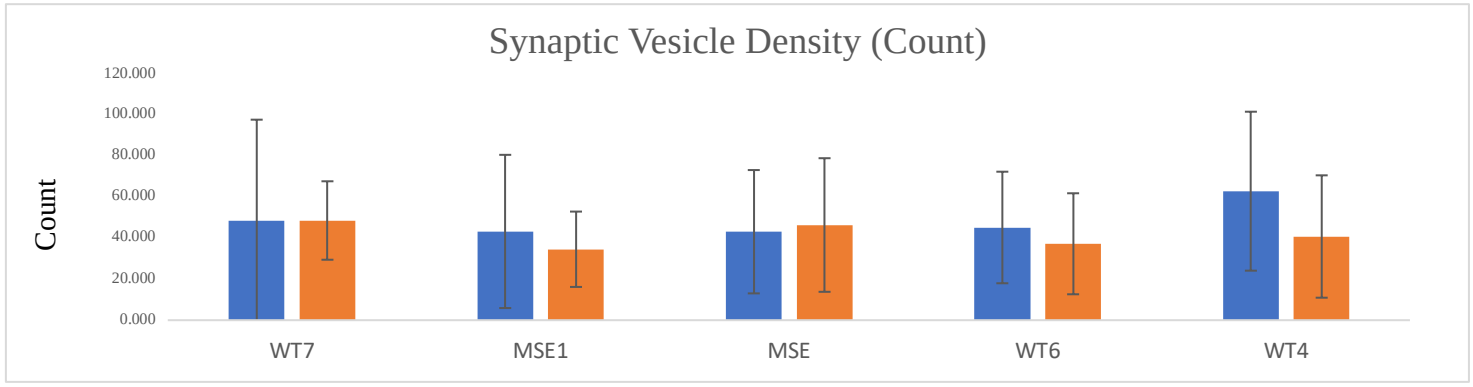
Synaptic Vesicle Density (Count)
Count
120.000
100.000
80.000
60.000
40.000
20.000
0.000
WT7
MSE1
MSE
WT6
WT4

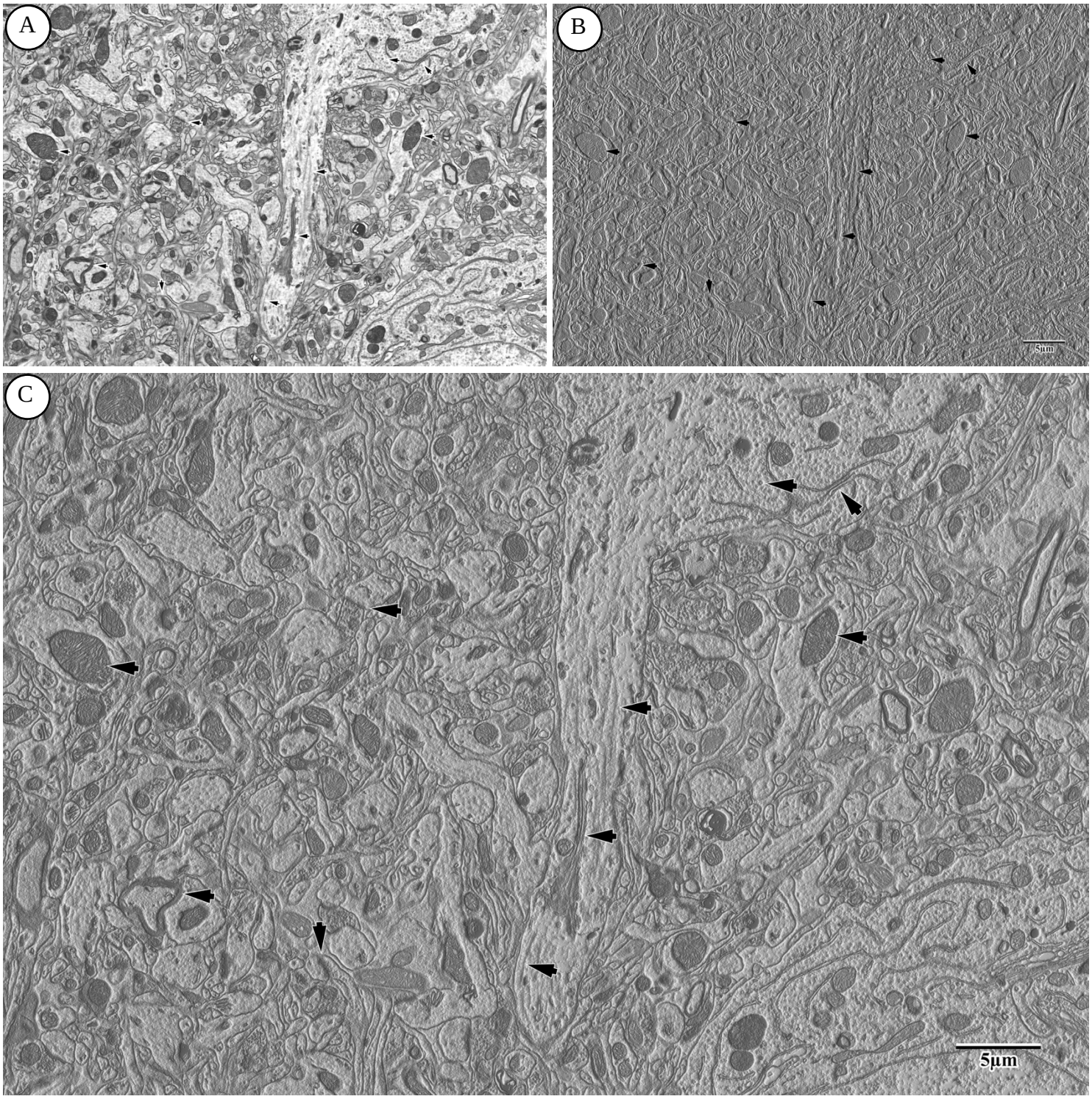

Figure 36: Low magnification embossed EMs of dendritic processes with accentuated cellular structures. Obtained EMs were processed and embossed using Photoshop and layers were embedded into a three-dimensional bump mapping. (C) was created using the original image (A), and topographic map (B) generated following embossing and three-dimensional mapping Specific structures (short arrows) are indicated across all panels in order to contrast these structures.

Appendix C: additional images of three-dimensional embossing

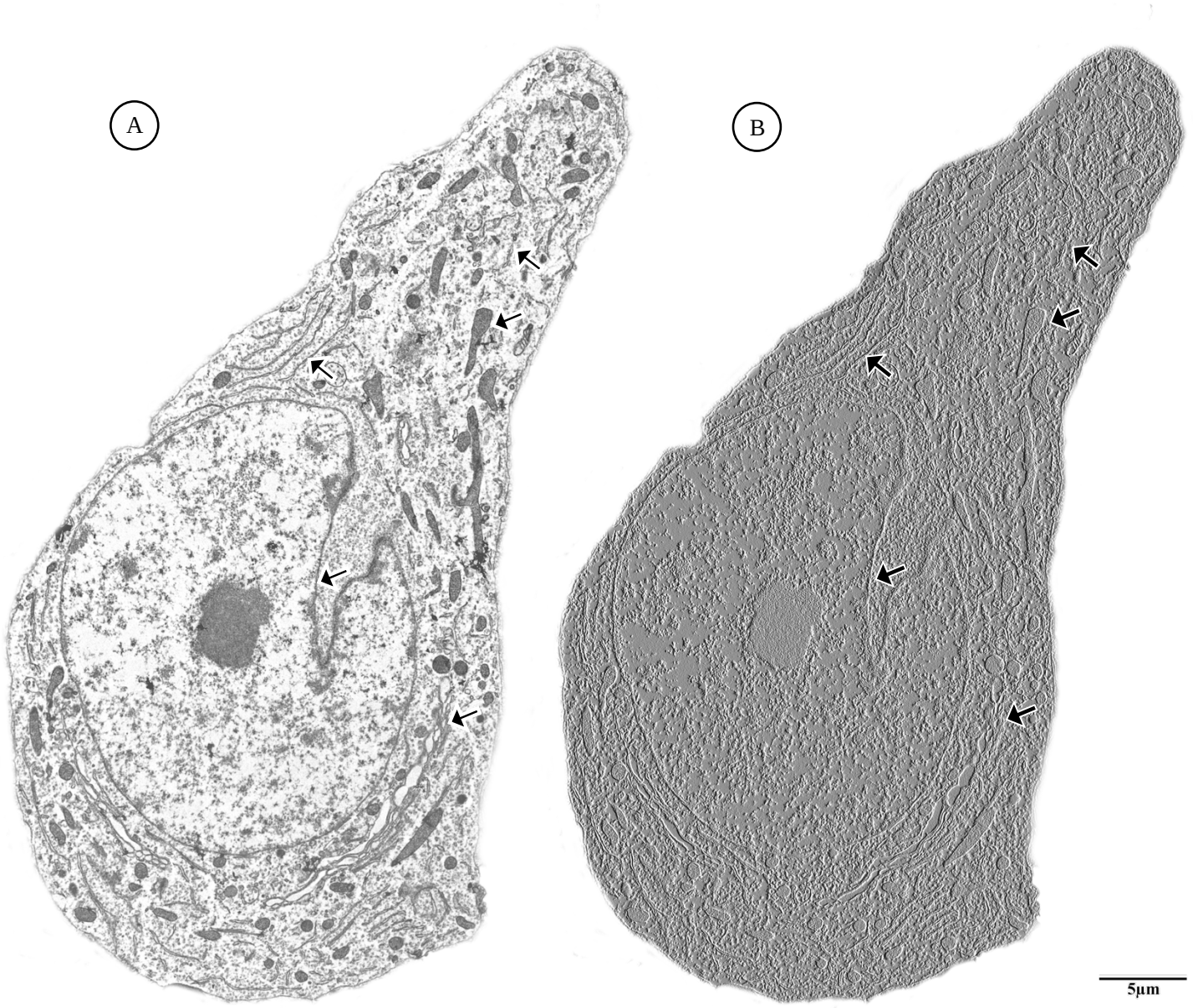

Figure 37: Embossed EMs of pyramidal neuron and internal structures in the layer 3 PI
EMs were processed and embossed using Photoshop and layers were embedded into the 3D bump mapping. The overlayed images, result in allowing both the use of electron microscopy imagery and 3D bump mapping analytics, seen in (C). (A) and (B) show the two different components that were overlayed. Cytoskeletal and subcellular structures (arrow) are indicated for comparison across the three images. Note that intracellular structures in (A) are fully visible but show a two-dimnsional morphology, while sturctures in (B) show a portruding stucture with but are harder to identify.

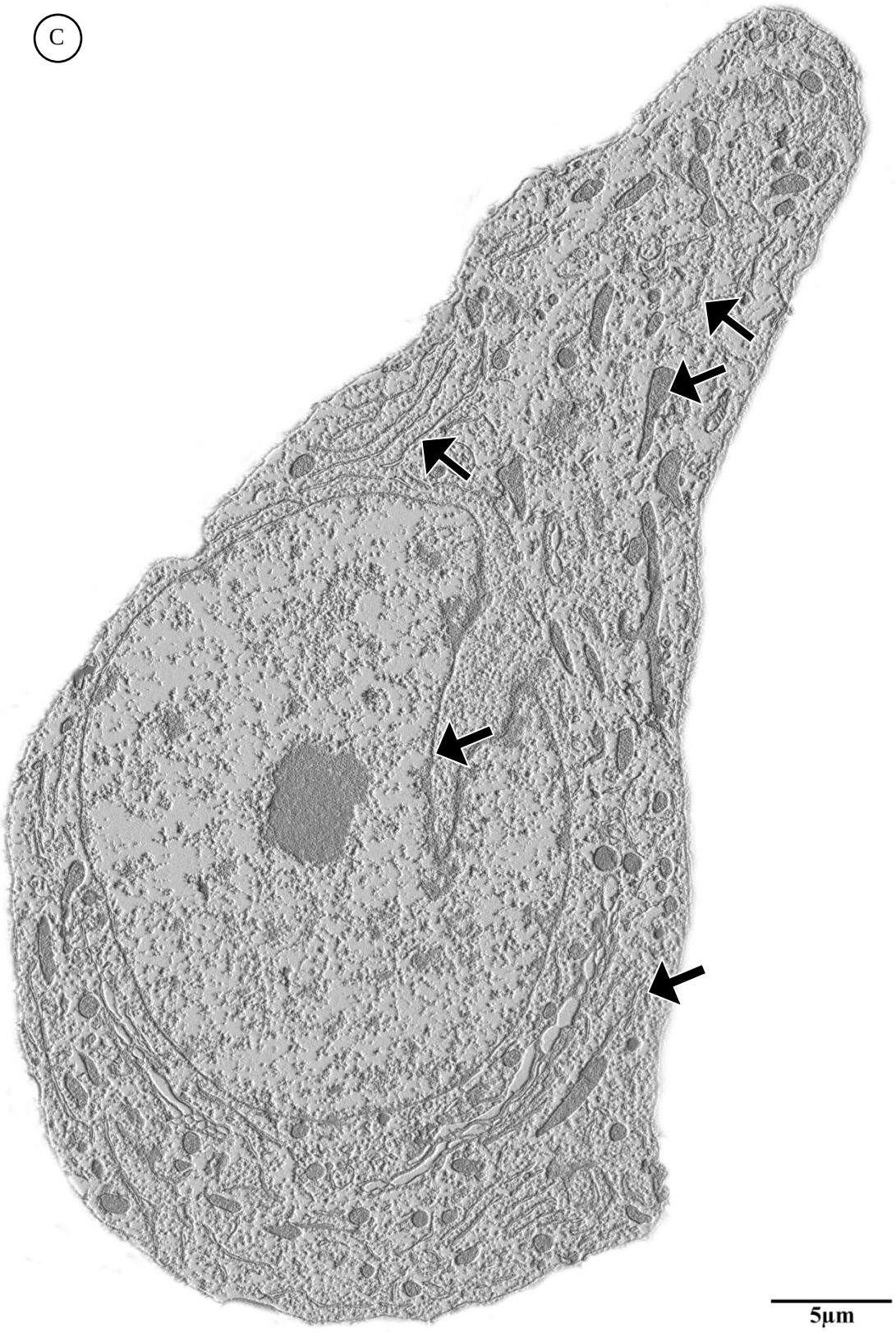
C
5µm

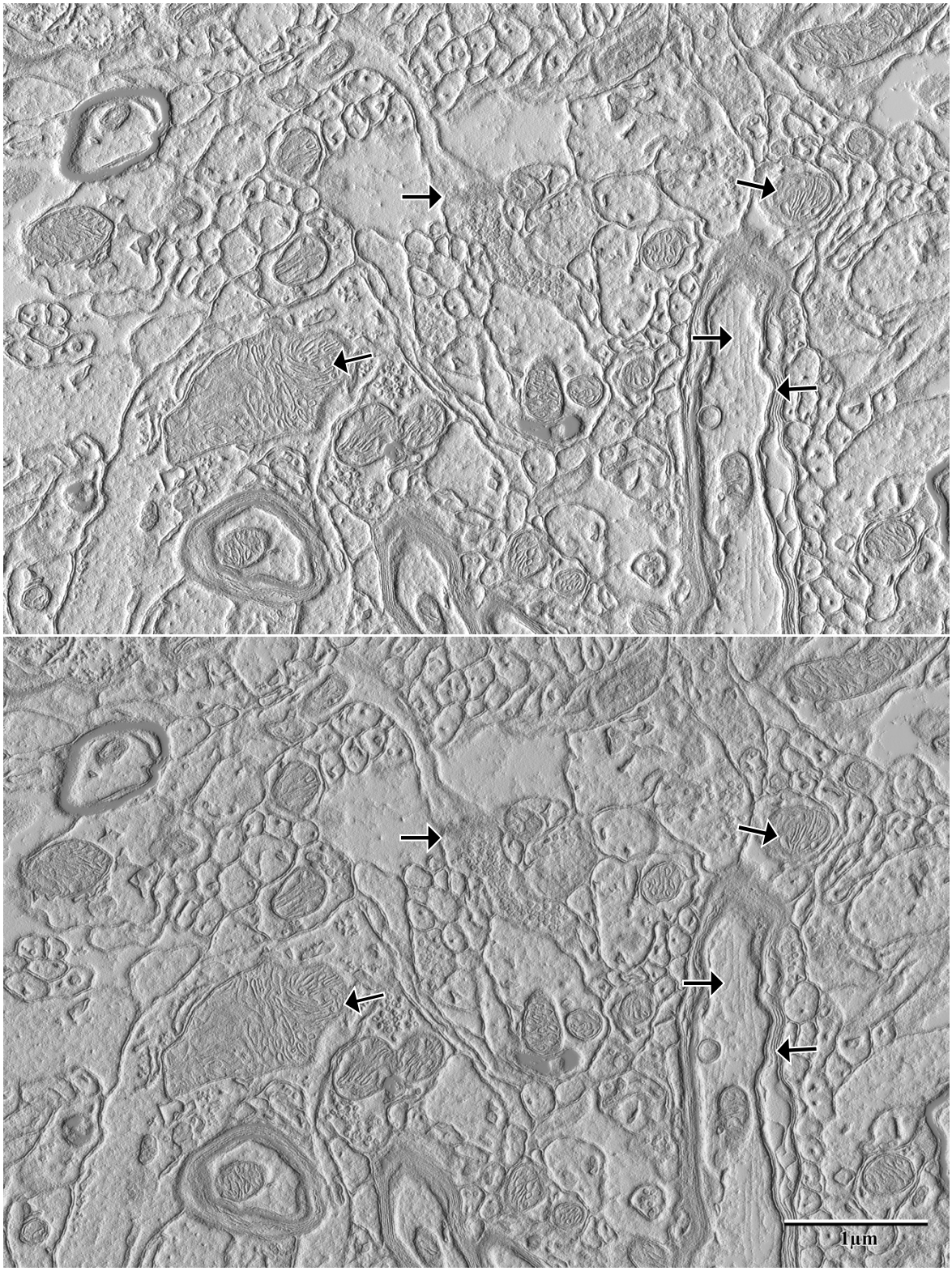

Figure 38: Embossed EMs of synaptic structures in control hemisphere
EMs were processed and embossed using Photoshop and layers were embedded into the 3D bump mappin. The overlayed images, result in allowing both the use of electron microscopy imagery and 3D bump mapping analytics. (Above) concave bump mapping while (Below) shows protruded bump maps. Cytoskeletal and subcellular structures (arrow) are pointed out for comparison across images.

Appendix D: Stereological Analysis

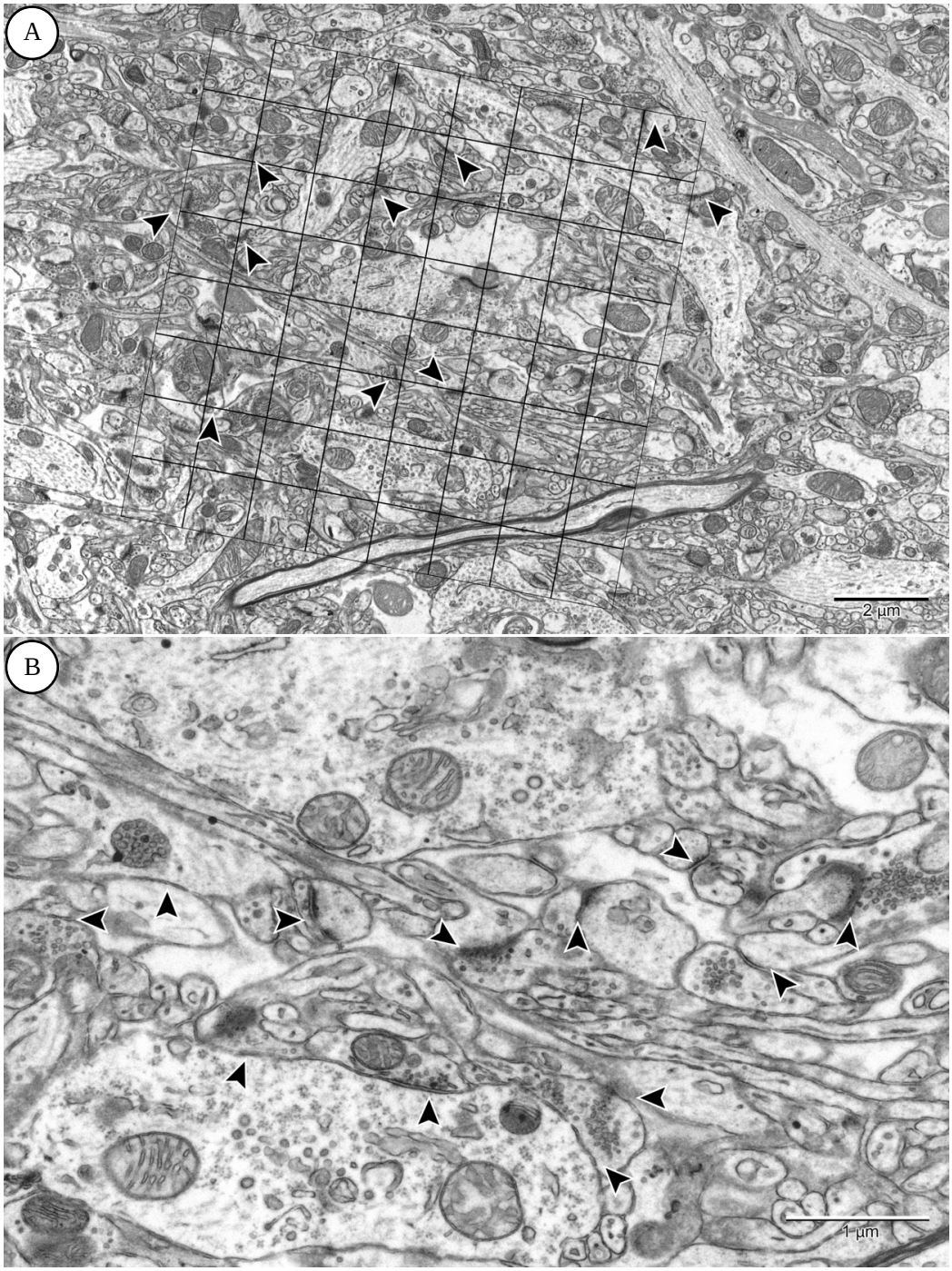

Figure 39: Stereological analysis for finding preferential magnification for data collection. A 1 μm^2 grid was placed on a 10,000x magnified image (Above), and compared to a 30,000x magnified image (Below) located within the same region. Synapses in (Above) with synaptic clefts that were intersected by 2 perpendicular lines (i.e. edge of the squares) were counted. The synapses in (Below) were also counted. Number of synapses in (Above) and (Below) were equal (found to be 9 synapses) hence 30,000x magnified images are good representation of synaptic density. This methodology was adopted due to its unbaised nature and since it allows for the implementation of random sampling via the random placement of the grid and the grid size itself.